Universidad Pública de Navarra
Nafarroako Unibertsitate Publikoa

Universidad Pública de Navarra

Departamento de Ingeniería Eléctrica, Electrónica y de Comunicación

Design and fabrication of novel optical fiber architectures for sensing applications

PhD dissertation by

José Javier Imas González

Advisors:

Dr. Carlos Ruiz Zamarreño

Prof. Ignacio Raúl Matías Maestro

Pamplona, October 2022

https://doi.org/10.48035/Tesis/2454/44230

"But he knew no other way; it was part of a short but inflexible personal code of ethics that he had carried with him all his adult life: do the job and do it well."

Robert Galbraith, The Silkworm

ACKNOWLEDGEMENTS

The development of this PhD thesis has been possible thanks to the financial support of the Spanish Ministry of Universities (FPU18/03087 grant), the Spanish Ministry of Science and Innovation (PID2019-106231RB-I00 TEC Research fund), the European Regional Development Fund (ERDF) (TEC2016-78047-R), the ATTRACT call financed by the European Union's Horizon 2020 research and innovation program (grant agreement No 777222), and the Public University of Navarra (PJUPNA26).

A special thanks to the Public University of Navarra (UPNA), where most of the work presented here was done, and the Advanced Photonic Components research group of Professor Jacques Albert at Carleton University in Ottawa, Canada, where a research stay was made.

RECONOCIMIENTOS

El desarrollo de esta tesis ha sido posible gracias al apoyo financiero del Ministerio de Universidades (beca FPU18/03087), el Ministerio de Ciencia e Innovación (PID2019-106231RB-I00 TEC), el Fondo Europeo de Desarrollo Regional (FEDER) (TEC2016-78047-R), la convocatoria ATTRACT financiada por el programa de investigación e innovación Horizon 2020 de la Unión Europea (subvención No 777222) y la Universidad Pública de Navarra (PJUPNA26).

Un agradecimiento especial a la Universidad Pública de Navarra (UPNA), donde se ha desarrollado la mayor parte del trabajo presentado en esta tesis, y al grupo de investigación de Componentes Fotónicos Avanzados del profesor Jacques Albert en la Universidad de Carleton en Ottawa, Canadá, donde se realizó una estancia de investigación.

AGRADECIMIENTOS

En primer lugar, gracias a mis padres, que a pesar de no entender nada de lo que hago y no ser grandes entusiastas de que hiciera una tesis, me han apoyado igualmente durante todo el doctorado, lo mismo que llevan haciendo desde siempre.

Gracias también a mis directores de tesis, Carlos, que lleva 3 años sin permitirme que le diga que tengo un mal día y que siempre es capaz de encontrar soluciones cuando parece que no las hay; y Natxo, que se las apaña para cargarme de trabajo cada vez que pasa por el despacho, pero consigue contagiarme también su buen humor. También quiero agradecer a Ignacio del Villar, que nunca tiene problema en sacar un hueco para ayudarme a mejorar una simulación cuando estoy estancado.

Merecen también un agradecimiento mis compañero de despacho: María Elena, Diego, Aritz, que siempre han estado dispuestos a echarme una mano o compartir su experiencia cuando lo he necesitado; y en especial, Ignacio, compañero de fatigas en el doctorado y en Pyroistech, que siempre contribuye a que vea las cosas con más optimismo. Gracia también a Pablo, que tuvo paciencia para enseñarme a trabajar con fibras a pesar de la gran cantidad que rompía al principio. No puedo olvidarme tampoco del resto de la familia de Sensores, con sus juevintxos y sus salidas al monte: Carlos, Nerea, Melanys, Omar, Ismel, Aitor, Desiree, Dina. De igual manera, también tengo que acordarme de los técnicos de laboratorio por su ayuda y sus bromas: Santi, David y Miguel.

Gracias también a mis amigos, que son pocos pero valiosos y que siempre muestran interés en que les explique qué estoy investigando y me ayudan a desconectar.

Por último, quiero agradecer a Jacques Albert y a los miembros de su grupo de investigación en la Universidad de Carleton, por haberme acogido con los brazos abiertos y haberme hecho sentir uno más.

ABSTRACT

Optical fiber sensors have experienced an important progress in recent years with the employment of structures based on gratings, interferometers or electromagnetic resonances, among others; and the development of nanotechnology, that has enabled the deposition of coatings at the micro- and nanometric level on the fiber. These advances have allowed the manufacture of optical fiber sensors for measuring physical variables, chemical parameters or biosensing applications.

This thesis contributes to the analysis and optimization, both theoretical and experimental, of different configurations and structures in optical fiber, applied to the development of sensors. Several structures are studied in this thesis, including Lossy Mode Resonances (LMRs) and optical fiber gratings: FBGs (fiber Bragg gratings), LPGs (long period fiber gratings) and TFBGs (tilted fiber Bragg gratings). The main research lines that are presented in this thesis are the fabrication of multisensing devices based on LMRs and the enhancement of the mode transition in optical fiber gratings: LPGs in double clad fibers and TFBGs. The common element between both research lines is the employment of thin films of high refractive index materials: tin oxide (SnO_2), indium tin oxide (ITO) and titanium dioxide (TiO_2). The results shown in this thesis reveal the potential of combining several structures and/or phenomena in optical fibers to improve the performance of optical fiber sensors.

RESUMEN

Los sensores de fibra óptica han experimentado un importante progreso en los últimos años con el empleo de estructuras basadas en redes de Bragg, interferómetros o resonancias electromagnéticas, entre otras; y el desarrollo de la nanotecnología, que ha permitido la deposición de recubrimientos a nivel micro y nanométrico sobre la fibra. Estos avances han posibilitado la fabricación de sensores de fibra óptica para medir variables físicas, parámetros químicos o aplicaciones de biosensado.

Esta tesis contribuye al análisis y optimización, tanto teórica como experimental, de diferentes configuraciones y estructuras en fibra óptica, aplicadas al desarrollo de sensores. En esta tesis se estudian varias estructuras, incluidas las *Lossy Mode Resonances* (LMRs) y redes en fibra óptica: FBGs (redes de Bragg en fibra), LPGs (redes de período largo en fibra) y TFBGs (redes de Bragg inclinadas en fibra). Las principales líneas de investigación que se presentan en esta tesis son la fabricación de dispositivos multisensores basados en LMRs y la mejora del fenómeno de la *mode transition* en redes de fibra óptica: LPGs en fibras con doble cladding y TFBGs. El elemento común entre ambas líneas de investigación es el empleo de películas delgadas de materiales de alto índice de refracción: óxido de estaño (SnO_2), óxido de indio y estaño (ITO) y dióxido de titanio (TiO_2). Los resultados mostrados en esta tesis revelan el potencial de combinar varias estructuras y/o fenómenos en fibras ópticas para mejorar el desempeño de los sensores de fibra óptica.

TABLE OF CONTENTS

Chapter 1
Introduction

1.1. Motivation and objectives

Optical fiber sensors have gained relevance in recent years due to the inherent advantages of optical fiber, including its light weight, electromagnetic immunity, low transmission losses, large bandwidth, multiplexing capability and resistance to harsh environments [1–3]. However, there are also important concerns, which are being progressively solved as the technology matures, like cost, complexity in interrogation systems and unfamiliarity of the end user with the technology. Different structures have been developed in optical fibers for sensing purposes, such as interferometers [4], gratings [5], electromagnetic resonances [6] or photonic crystal fibers [7], among many others.

The development of nanotechnology has widened the range of applications of optical fiber sensors, as it has enabled the deposition of coatings at the micro- and nanometric level on the fiber [8]. These coatings are made of materials sensitive to the parameters to be measured and modify the properties of the light traveling through the fiber, leading to the manufacture of sensors for applications such pH sensing [9], gas detection [10], or biosensing [11–13], among others. Some of the employed deposition techniques are dip coating [14], layer by layer nanoassembly (LbL) [15], sputtering [16], and electrospinning [17].

Metal oxides can be found among the materials deposited on optical fibers for the development of sensors. Metal oxides are characterized by their thermal and mechanical robustness, good resistance to chemical degradation and the fact that their properties are not affected by aging. Examples of this type of materials include tin oxide (SnO_2), indium tin oxide (ITO), zinc oxide (ZnO) or titanium dioxide (TiO_2). The first sensors that exploited metal oxides were based on resistance measurement [8]. In the case of optical fiber, one of the techniques that can be employed for manufacturing sensors with metallic oxides is the deposition of a thin film on cladding removed multimode fibers (CRMF) [18,19], cladding etched single mode fibers [20] or D-shaped fibers [21,22]; generating resonances known as Lossy Mode Resonances (LMRs) [23].

LMRs are obtained when the real part of the permittivity of the thin film material is positive and higher in magnitude than both its imaginary part and the real part of the permittivity of the material surrounding the thin film. Metal oxides as well as polymers fulfill previous conditions [23]. Under these conditions, one or several resonances will appear in the transmission spectrum at certain wavelengths. The wavelength at maximum attenuation at which an LMR is observed, known as resonance wavelength, depends on the optical properties on the thin film, its thickness and the refractive index of the surrounding medium [24]. For instance, if the first two parameters are fixed, a relationship can be established between the wavelength of the resonance and the surrounding medium refractive index (SRI), enabling the

development of refractometers [25]. LMRs possess some advantages over the well known Surface Plasmon Resonances (SPRs), such as the possibility of being generated with both transverse electric (TE) and transverse magnetic (TM) polarized light or obtaining several resonances in the same spectrum [23].

On the other hand, one of the main concerns in the field of optical sensors in the last years is the development of platforms that allow the simultaneous measurement of several magnitudes [26–28], such as temperature, relative humidity, pressure, refractive index, etc. This matter also extents to the biosensing field [29–31], where the detection of multiple biomarkers can improve considerably the accuracy in the diagnosis or monitoring of a disease [32–34]. Nevertheless, regarding LMRs, the manufacture of multisensing devices is still in its infancy and very few sensors, mostly based on planar waveguides, have been recently developed with this purpose, such as a multichannel refractometer [35] or a sensor for measuring simultaneously the relative humidity and the temperature based on a dually nanocoated waveguide [36].

Following such considerations, the aim of this thesis is to develop sensors for measuring several parameters based on LMRs, combining them or not with other technologies; as well as continue exploring the possibilities offered by metal oxide nanocoatings, responsible for the generation of LMRs, in other optical structures. For that purpose, the main objectives of this thesis are:

- Developing multisensing devices through the combination of LMRs with other optical structures such as gratings.
- Obtaining several independent LMRs on a single optical fiber for multisensing purposes.
- Studying the enhancement of the sensitivity in optical fiber gratings through the deposition of metal oxide thin films, which is strongly linked to the LMR effect.
- Acquiring the knowledge to simulate all the proposed structures in order to perform numerical analysis, be able to optimize the studied devices and predict their response.

1.2. Organization

This thesis has been organized in chapters as follows. First of all, Chapter 2 presents a review of wavelength based optical sensing structures that have been employed, individually or combined, during the development of this thesis, such as LMRs and optical fiber gratings. The latter include fiber Bragg gratings (FBGs), long period fiber gratings (LPFGs or LPGs) and tilted fiber Bragg gratings (TFBGs). For each structure the main characteristics, operation, types, fabrication techniques and typical applications are discussed.

The next chapter (Chapter 3) is focused on the study and development of different structures and configurations based on LMRs that enable measuring more than one variable or parameter simultaneously, with the purpose of obtaining multisensing platforms. In the first place, the employment of different grating patterns on thin films

deposited on two distinct substrates, coverslips and D-shaped optical fibers, is theoretically analyzed. The idea behind these structures is to generate an LMR with the thin film while producing bands in the reflection spectrum due to the grating pattern. Two different thin film patterns are studied: a pure grating pattern and the combination of a section of constant thickness and a grating section. The parameters of the different structures are assessed in order to find their optimum values for their implementation, focusing on the case of a pure grating pattern on a D-shaped optical fiber.

Then, the combination of an LMR and an FBG is implemented on a D-shaped optical fiber for measuring the surrounding medium refractive index (SRI) and the temperature at the same time with a single device. The LMR is obtained through the deposition of a TiO_2 thin film while the FBG is inscribed on the core of the optical fiber. The device response to changes in the SRI and temperature is characterized and its performance is compared with other sensors with similar characteristics.

The last device that is studied in this chapter, both theoretically and experimentally, is a D-shaped optical fiber where two independent LMRs are obtained through the deposition of a nanocoating with two sections of different thickness. The possibility of obtaining several independent LMRs in a single device has been previously demonstrated in the case of planar waveguides [37], but not in the case of optical fibers. The fabrication process is explained in detail and it is studied how to optimize the length of the sections of the nanocoating so both resonances have a similar depth. Finally, the performance of the device as a refractometer is assessed.

Chapter 4 is focused on the study of the mode transition in different types of optical fiber gratings. First, this phenomenon is analyzed in LPGs inscribed on double clad fibers where the refractive index of the second cladding is lower than that of the first cladding. It was numerically shown that a second cladding can enhance the mode transition in LPGs in [38] but this analysis lacked an experimental demonstration until now. Initially, the etching process to obtain LPGs with a second cladding with different thicknesses is described. Then, the mode transition is experimentally studied in these fibers through the deposition of a TiO_2 thin film, assessing the impact of the second cladding thickness on the sensitivity to the thin film thickness. These results are supported with simulations of the wavelength shift of the resonances and the evolution of the effective indices of the cladding modes as a function of the thin film thickness, as well as simulations of the optical field intensity distribution. Finally, the sensitivity to the SRI in liquids (1.33 - 1.47 range) is evaluated for LPGs with different values of the second cladding thickness.

In the second part of the chapter, the mode transition is theoretically studied and experimentally demonstrated in TFBGs through the deposition of high refractive index thin films (ITO, TiO_2). The mode transition is first shown in an ITO deposition employing a sputtering deposition system. Then, two TiO_2 depositions are carried out with an atomic layer deposition (ALD) system, each one with a separate TFBG and a different polarization state (P-polarization, corresponding to EH modes; and S-polarization, corresponding to HE modes; respectively). The evolution of the effective indices of the cladding modes and the power distribution of the mode fields

during the mode transition are simulated to support the previous results and understand the differences between both polarizations. The mode transition is also tested as a method to recover the thickness of the deposited thin films by comparing the experimental results with the simulated mode transitions using for the thin film the refractive index value given by the ellipsometer. The results are compared with the ones obtained by the ellipsometer and the scanning electron microscope (SEM).

Finally, Chapter 5 summarizes the principal results obtained in this thesis, presenting the main conclusions that can be extracted from this work and the lines that have been opened and can be continued in the near future.

Bibliography

1. Optical Fiber Sensors: Advanced Techniques and Applications ; Rajan, G., Ed.; CRC Pres, 2015; ISBN 9781482228250.
2. Lee, B. Review of the Present Status of Optical Fiber Sensors. Optical Fiber Technology 2003, 9, 57–79, doi:10.1016/S1068-5200(02)00527-8.
3. Villar, I. del; Matias, I.R. Optical Fiber Sensors : Fundamentals for Development of Optimized Devices; Wiley-IEEE Press; ISBN 978-1-119-53476-1.
4. Lee, B.H.; Kim, Y.H.; Park, K.S.; Eom, J.B.; Kim, M.J.; Rho, B.S.; Choi, H.Y. Interferometric Fiber Optic Sensors. Sensors 2012, Vol. 12, Pages 2467-2486 2012, 12, 2467–2486, doi:10.3390/S120302467.
5. Othonos, Andreas.; Kalli, Kyriacos. Fiber Bragg Gratings : Fundamentals and Applications in Telecommunications and Sensing. 1999, 422.
6. Sharma, A.K.; Jha, R.; Gupta, B.D. Fiber-Optic Sensors Based on Surface Plasmon Resonance: A Comprehensive Review. IEEE Sensors Journal 2007, 7, 1118–1129, doi:10.1109/JSEN.2007.897946.
7. Russel, P. Photonic Crystal Fibers. Science 2003, 299, 57–61, doi:10.1126/SCIENCE.1079280.
8. Elosua, C.; Arregui, F.J.; Del Villar, I.; Ruiz-Zamarreño, C.; Corres, J.M.; Bariain, C.; Goicoechea, J.; Hernaez, M.; Rivero, P.J.; Socorro, A.B.; et al. Micro and Nanostructured Materials for the Development of Optical Fibre Sensors. Sensors (Switzerland) 2017, 17, 2312.
9. Lin, J. Recent Development and Applications of Optical and Fiber-Optic PH Sensors. TrAC Trends in Analytical Chemistry 2000, 19, 541–552, doi:10.1016/S0165-9936(00)00034-0.
10. Elosua, C.; Matias, I.R.; Bariain, C.; Arregui, F.J. Volatile Organic Compound Optical Fiber Sensors: A Review. Sensors 2006, Vol. 6, Pages 1440-1465 2006, 6, 1440–1465, doi:10.3390/S6111440.
11. Brogan, K.L.; Walt, D.R. Optical Fiber-Based Sensors: Application to Chemical Biology. Current Opinion in Chemical Biology 2005, 9, 494–500, doi:10.1016/J.CBPA.2005.08.009.
12. Leung, A.; Shankar, P.M.; Mutharasan, R. A Review of Fiber-Optic Biosensors. Sensors and Actuators B: Chemical 2007, 125, 688–703, doi:10.1016/J.SNB.2007.03.010.
13. Bosch, M.E.; Sánchez, A.J.R.; Rojas, F.S.; Ojeda, C.B. Recent Development in Optical Fiber Biosensors. Sensors 2007, Vol. 7, Pages 797-859 2007, 7, 797–859, doi:10.3390/S7060797.
14. Scriven, L.E. Physics and Applications of DIP Coating and Spin Coating. MRS Online Proceedings Library (OPL) 1988, 121, doi:10.1557/PROC-121-717.
15. Decher, G. Fuzzy Nanoassemblies: Toward Layered Polymeric Multicomposites. Science (1979) 1997, 277, 1232–1237, doi:10.1126/SCIENCE.277.5330.1232/ASSET/CAD200AF-11BC-422A-A1F2-02C346F12F0A/ASSETS/GRAPHIC/SE3675666003.JPEG.

16. Kelly, P.J.; Arnell, R.D. Magnetron Sputtering: A Review of Recent Developments and Applications. Vacuum 2000, 56, 159–172, doi:10.1016/S0042-207X(99)00189-X.

17. Teo, W.E.; Ramakrishna, S. A Review on Electrospinning Design and Nanofibre Assemblies. Nanotechnology 2006, 17, R89, doi:10.1088/0957-4484/17/14/R01.

18. Sanchez, P.; Zamarreño, C.R.; Hernaez, M.; Del Villar, I.; Fernández-Valdivieso, C.; Matias, I.R.; Arregui, F.J. Lossy Mode Resonances toward the Fabrication of Optical Fiber Humidity Sensors. Measurement Science and Technology 2011, 23, 014002, doi:10.1088/0957-0233/23/1/014002.

19. Hernaez, M.; Mayes, A.G.; Melendi-Espina, S. Graphene Oxide in Lossy Mode Resonance-Based Optical Fiber Sensors for Ethanol Detection. Sensors 2018, Vol. 18, Page 58 2017, 18, 58, doi:10.3390/S18010058.

20. Ascorbe, J.; Corres, J.M.; Matias, I.R.; Arregui, F.J. High Sensitivity Humidity Sensor Based on Cladding-Etched Optical Fiber and Lossy Mode Resonances. Sensors and Actuators B: Chemical 2016, 233, 7–16, doi:10.1016/J.SNB.2016.04.045.

21. Chiavaioli, F.; Zubiate, P.; Del Villar, I.; Zamarreño, C.R.; Giannetti, A.; Tombelli, S.; Trono, C.; Arregui, F.J.; Matias, I.R.; Baldini, F. Femtomolar Detection by Nanocoated Fiber Label-Free Biosensors. ACS Sensors 2018, 3, 936–943, doi:10.1021/acssensors.7b00918.

22. Zubiate, P.; Zamarreño, C.R.; Sánchez, P.; Matias, I.R.; Arregui, F.J. High Sensitive and Selective C-Reactive Protein Detection by Means of Lossy Mode Resonance Based Optical Fiber Devices. Biosensors and Bioelectronics 2017, 93, 176–181, doi:10.1016/j.bios.2016.09.020.

23. Del Villar, I.; Arregui, F.J.; Zamarreño, C.R.; Corres, J.M.; Bariain, C.; Goicoechea, J.; Elosua, C.; Hernaez, M.; Rivero, P.J.; Socorro, A.B.; et al. Optical Sensors Based on Lossy-Mode Resonances. Sensors and Actuators B: Chemical 2017, 240, 174–185, doi:10.1016/J.SNB.2016.08.126.

24. Del Villar, I.; Hernaez, M.; Zamarreño, C.R.; Sánchez, P.; Fernández-Valdivielso, C.; Arregui, F.J.; Matias, I.R. Design Rules for Lossy Mode Resonance Based Sensors. Applied Optics 2012, 51, 4298–4307, doi:10.1364/AO.51.004298.

25. Zubiate, P.; Zamarreño, C.R.; Del Villar, I.; Matias, I.R.; Arregui, F.J. High Sensitive Refractometers Based on Lossy Mode Resonances (LMRs) Supported by ITO Coated D-Shaped Optical Fibers. Optics Express 2015, 23, 8045, doi:10.1364/oe.23.008045.

26. Hromadka, J.; Korposh, S.; Partridge, M.C.; James, S.W.; Davis, F.; Crump, D.; Tatam, R.P. Multi-Parameter Measurements Using Optical Fibre Long Period Gratings for Indoor Air Quality Monitoring. Sensors and Actuators, B: Chemical 2017, 244, 217–225, doi:10.1016/j.snb.2016.12.050.

27. Pevec, S.; Donlagic, D. MultiParameter Fiber-Optic Sensor for Simultaneous Measurement of Thermal Conductivity, Pressure, Refractive Index, and Temperature. IEEE Photonics Journal 2017, 9, doi:10.1109/JPHOT.2017.2651978.

28. Kim, H.T.; Yu, M. Lab-on-Fiber Nanoprobe with Dual High-Q Rayleigh Anomaly-Surface Plasmon Polariton Resonances for Multiparameter Sensing. Scientific Reports 2019, 9, 1–9, doi:10.1038/s41598-018-38113-1.

29. Washburn, A.L.; Luchansky, M.S.; Bowman, A.L.; Bailey, R.C. Quantitative, Label-Free Detection of Five Protein Biomarkers Using Multiplexed Arrays of Silicon Photonic Microring Resonators. Analytical Chemistry 2010, 82, 69–72, doi:10.1021/ac902451b.

30. Huang, R.; Liao, Y.; Zhou, X.; Fu, Y.; Xing, D. Multiplexed Detection of MicroRNA Biomarkers from Tumor Cells and Tissues with a Homogeneous Nano-Photon Switch. Sensors and Actuators, B: Chemical 2017, 247, 505–513, doi:10.1016/j.snb.2017.03.055.

31. Liao, Z.; Zhang, Y.; Li, Y.; Miao, Y.; Gao, S.; Lin, F.; Deng, Y.; Geng, L. Microfluidic Chip Coupled with Optical Biosensors for Simultaneous Detection of Multiple Analytes: A Review. Biosensors and Bioelectronics 2019, 126, 697–706.

32. Muinao, T.; Deka Boruah, H.P.; Pal, M. Multi-Biomarker Panel Signature as the Key to Diagnosis of Ovarian Cancer. Heliyon 2019, 5, e02826.

33. Nozaki, T.; Sugiyama, S.; Koga, H.; Sugamura, K.; Ohba, K.; Matsuzawa, Y.; Sumida, H.; Matsui, K.; Jinnouchi, H.; Ogawa, H. Significance of a Multiple Biomarkers Strategy Including Endothelial Dysfunction to Improve Risk Stratification for Cardiovascular Events in Patients at High Risk for Coronary Heart Disease. J Am Coll Cardiol 2009, 54, 601–608, doi:10.1016/j.jacc.2009.05.022.

34. Shariat, S.F.; Karakiewicz, P.I.; Ashfaq, R.; Lerner, S.P.; Palapattu, G.S.; Cote, R.J.; Sagalowsky, A.I.; Lotan, Y. Multiple Biomarkers Improve Prediction of Bladder Cancer Recurrence and Mortality in Patients Undergoing Cystectomy. Cancer 2008, 112, 315–325, doi:10.1002/cncr.23162.

35. Dominguez, I.; Corres, J.M.; Fuentes, O.; Del Villar, I.; Matias, I.R. Multichannel Refractometer Based on Lossy Mode Resonances. IEEE Sensors Journal 2022, 22, 3181–3187, doi:10.1109/JSEN.2022.3142050.

36. Dominguez, I.; Del Villar, I.; Fuentes, O.; Corres, J.M.; Matias, I.R. Dually Nanocoated Planar Waveguides towards Multi-Parameter Sensing. Scientific Reports 2021 11:1 2021, 11, 1–8, doi:10.1038/s41598-021-83324-8.

37. Dominguez, I.; Del Villar, I.; Fuentes, O.; Corres, J.M.; Matias, I.R. Interdigital Concept in Photonic Sensors Based on an Array of Lossy Mode Resonances. Scientific Reports 2021 11:1 2021, 11, 1–11, doi:10.1038/s41598-021-92765-0.

38. Del Villar, I.; Matias, I.R.; Arregui, F.J. Deposition of Coatings on Long-Period Fiber Gratings: Tunnel Effect Analogy. Optical and Quantum Electronics 2006 38:8 2006, 38, 655–665, doi:10.1007/S11082-006-9002-3.

Chapter 2

Lossy Mode Resonances and Optical Fiber Gratings: State of the Art

2.1. Introduction

Optical fiber sensors are devices in which a physical, chemical or biological variable affects light propagation through an optical fiber, producing a modulation of the optical signal that is related to the variable to be measured [1]. The interest of these sensors is based on the outstanding advantages of optical fiber including electromagnetic immunity, small size, lightweight, low transmission losses, high sensitivity, large bandwidth, multiplexing capability or resistance to harsh environments [1–3]. These properties have enabled the development of optical fiber sensors for measuring physical variables (temperature, strain, pressure), chemical parameters (pH, gas detection) or biosensing (proteins, viruses, DNA sequences) [4–8].

Regarding the light property in which the sensor operation is based, four main categories of optical fiber sensors can be distinguished: intensity modulated sensors, phase modulated (interferometric) sensors, polarization modulated (polarimetric) sensors and wavelength modulated (spectrometric) sensors [1]. Intensity modulated sensors are based on monitoring the intensity changes at a certain wavelength and they are cheap and simple, but they require a stable reference signal [1]. With respect to interferometric sensors, they employ the interference between two beams that have propagated though different optical paths, within the same or in two different optical fibers [9]. Interferometry is traditionally based on measuring the phase difference between these two beams [1], although interferometers can also make use of changes in wavelength, intensity or frequency in the interferometric signal for sensing purposes [9]. In the case of polarimetric sensors, they measure how the state of polarization of light is affected by the variable of interest [10]. Finally, wavelength modulated sensors track the shift of the transmission or attenuation bands in the optical spectrum. They are expensive, as they need a spectrometer or an interrogator to monitor the wavelength shift, but they are robust, reliable in terms of noise and they offer a high versatility [11]. The current thesis is focused on the development of wavelength modulated sensing structures

Concerning wavelength based optical fiber sensors, there are three main types [12]: sensors based on gratings (fiber Bragg gratings, long period gratings, tilted fiber Bragg gratings), interferometers (Fabry Pérot, Mach-Zehnder, Michelson, Sagnac) and resonance-based sensors (surface plasmon resonances and lossy mode resonances). Gratings consist of a periodic modulation of the refractive index along the core of an optical fiber [13–15]. Regarding interferometers, in this case only the spectral response is considered. Resonance based sensors rely on the utilization of a thin film that affects the propagation of the light through the fiber thus generating a resonance [16,17].

This chapter presents a review of wavelength based optical fiber sensing structures that have been used, individually or combined, during the development of this thesis, such as lossy mode resonances (LMRs) and optical fiber gratings. The latter case comprises fiber Bragg gratings (FBGs), long period fiber gratings (LPFGs or LPGs) and tilted fiber Bragg gratings (TFBGs). For each structure the main characteristics, operation, types, fabrication techniques and typical applications are discussed.

2.2. Lossy Mode Resonances (LMRs)

When an optical fiber in which the cladding has been totally or partially removed is covered with a thin film, light propagation is affected due to the interaction of the evanescent field of the fiber with the thin film, which can lead to the generation of different types of resonances depending on the relationships between the refractive indices of the optical fiber and the thin film material.

Before establishing the conditions for the generation of the different types of resonances, the employed notation must be introduced. For a certain material, the refractive index *N*, the permittivity ε and the relationship between both are given by:

$$N = n + k \cdot i \tag{2.1}$$

$$\varepsilon = \varepsilon' + \varepsilon'' \cdot i \tag{2.2}$$

$$\varepsilon = N^2 = (n + k \cdot i)^2 = (n^2 - k^2) + (2nk) \cdot i \tag{2.3}$$

where *n* and *k* are the real and imaginary parts of the refractive index respectively and ε' are ε'' are the real and imaginary parts of the permittivity. From the previous equations it can be deduced that $\varepsilon' = n^2 - k^2$ and $\varepsilon'' = 2nk$ respectively.

A surface plasmon resonance (SPR) is generated when the real part of the permittivity of the thin film material is negative and higher in magnitude than both its imaginary part and the real part of the permittivity of the material surrounding the thin film. In case the second condition if fulfilled but the real part of the permittivity of the thin film material is positive, a second type of resonance, called lossy mode resonance (LMR), is generated [17,18]. These conditions are summarized in the table in **Fig. 2.1**, where the subindex *'TF'* refers to the thin film material and the subindex *'SM'* to the surrounding material. The map k_{TF} vs n_{TF} is plotted assuming a silica substrate with a refractive index of 1.45 [19] and that air is the surrounding medium (refractive index of 1 [20]).

This section will be mainly focused on LMRs since several sensors based on them have been developed in this thesis. However, the differences between LMRs and SPRs will be briefly introduced in the next subsection. The following subsections will describe the main characteristics of LMRs, the different techniques to generate them and their applications.

Type of Resonance	$\varepsilon', \varepsilon''$ conditions	n_{TF}, k_{TF} conditions $\forall\ n > 0, k > 0$
SPR Surface Plasmon Resonance	$\varepsilon'_{TF} < 0$ $\lvert\varepsilon'_{TF}\rvert > \lvert\varepsilon''_{TF}\rvert$ $\lvert\varepsilon'_{TF}\rvert > \lvert\varepsilon''_{SM}\rvert$	$k_{TF} > (\sqrt{2}+1)\cdot n_{TF}$ $k_{TF}^2 - n_{TF}^2 > 1.45^2$
LMR Lossy Mode Resonance	$\varepsilon'_{TF} > 0$ $\lvert\varepsilon'_{TF}\rvert > \lvert\varepsilon''_{TF}\rvert$ $\lvert\varepsilon'_{TF}\rvert > \lvert\varepsilon''_{SM}\rvert$	$k_{TF} < (\sqrt{2}-1)\cdot n_{TF}$ $n_{TF}^2 - k_{TF}^2 > 1.45^2$

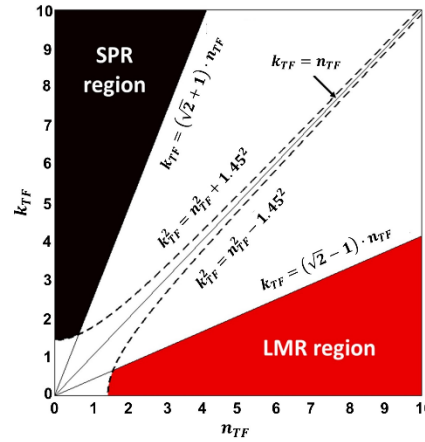

Fig. 2.1 Conditions for the generation of SPR and LMR. Adapted from [17]. Copyright 2017, with permission from Elsevier.

2.2.1. Main characteristics of LMRs and differences with SPRs

LMRs are generated because a mode that is guided in the optical fiber starts to be guided in the thin film with losses. This phenomenon occurs when this lossy mode is near the cutoff condition. The described transition is recognizable because the effective index of this mode begins to increase for wavelengths below that of the maximum LMR depth in the transmission spectrum, until surpassing the refractive index of the optical fiber. This implies that the mode is guided by the thin film, whose refractive index is higher than that of silica (material of the optical fiber), for shorter wavelengths while it is guided by the core for longer wavelengths [17,18,21].

The wavelength where the cutoff condition takes place, thus the position of the resonance or resonance wavelength, depends on the real part of the refractive index of the material of the thin film, its thickness and the surrounding medium refractive index (SRI). In general, these parameters have to be increased to achieve a higher sensitivity [22]. In practice, the SRI value is usually fixed by the application and the real part of the refractive index of the coating is the parameter that tends to be increased to improve the sensitivity [17].

Regarding SPRs, they are obtained when the evanescent field couples to a surface plasmon polariton. However, although LMRs and SPRs are generated by different physical phenomena, their operation and applications are similar. In both cases, a resonance is obtained in the optical spectrum (reflection or transmission, depending on the configuration) and its position depends on the properties of the thin film and those of the surrounding medium, therefore both types of resonances are utilized for the development of highly sensitive refractometric devices [17]. Nevertheless, there are important differences between LMRs and SPRs that will be explained in the following paragraphs.

In the first place, LMRs and SPRs appear with different materials due to the conditions they have to fulfil. In general, LMRs are generated with metal oxides (tin oxide, SnO_2; titanium dioxide, TiO_2) and polymers [23] while SPRs are obtained with pure metals, such as gold or silver [24]. However, there are hybrid materials, for instance indium tin oxide (ITO) [25], that are able to generate both type of resonances at different wavelengths.

The second difference between LMRs and SPRs is the optimum incidence angle. In the case of LMRs, the best incidence angle approaches 90º [26] making the optical fiber the most adequate structure for LMR generation. On the other hand, SPR excitation is favored by angles in the 40 - 75º range [24], which leads to the employment of the Kretschmann configuration [27] as well as optical fibers for the generation of SPRs. Both configurations are shown in **Fig. 2.2**. The Kretschmann configuration consists of an optical prism where a thin film is deposited and in which light is coupled and reflected with a variable incidence angle. Kretschmann configuration can also be employed to generate LMRs [28].

In an optical fiber configuration, the resonance will be monitored as a dip in the transmitted power as a function of the wavelength, while in the Kretschmann configuration the resonance will be monitored as a dip in the reflected power as a function of the incident angle or as a function of the wavelength. It is also worth mentioning that both type of resonances can be obtained in a planar waveguide consisting of a coverslip, as it has been recently demonstrated [29].

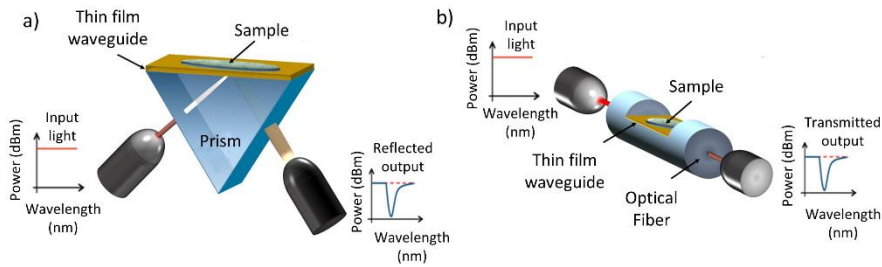

Fig. 2.2 Configurations for the generation of SPRs and LMRs: a) Kretschmann configuration, b) Optical fiber. Adapted from [17]. Copyright 2017, with permission from Elsevier.

Another important difference is that LMRs can be generated with both TE (transverse electric) and TM (transverse magnetic) polarized light, while SPRs can only be generated with TM polarized light [30,31]. Finally, several resonances can be obtained with LMRs when the thin film thickness is progressively increased and a higher number of modes are near the cutoff condition, whereas in the case of the SPR the resonance shifts to higher wavelengths and no additional resonances appear [30].

2.2.2. Thin film deposition techniques

In order to generate a LMR, it is necessary to fabricate a thin film on the corresponding substrate (usually an optical fiber). Different techniques are used for this purpose [32]:

- **Dip coating**: this technique consists in immersing a substrate in one or more liquids to produce a thin film and it does not usually require very complex instruments. The most common dip coating methods employed in the case of LMR based sensors are Sol-gel and Layer-by-Layer nano assembly (LbL). In the first case the substrate is dipped in the sol (dispersion of colloidal particles) and then extracted to produce a gel, which will solidify after drying, thus producing a thin film. Regarding LbL, the process consists in immersing the substrate alternatively in cationic and anionic solutions with an intermediate washing step for eliminating the excess of material [32].

- **Physical vapor deposition (PVD)**: this process involves vaporizing atoms or molecules from a solid or liquid source, transporting them as vapor through a vacuum or low pressure gas environment and condensing them on a substrate. It is a line-of-sight-process, which means that complex pieces have to be rotated in order to obtain a uniform coating [33]. There are different techniques including sputtering, electron beam deposition, ion beam deposition, cathodic arc deposition and thermal evaporative deposition [32]. Only the first two methods are described in detail as they are the ones that have been used in this thesis:

  – *Sputtering*: in this process a gas (typically argon or xenon) is ionized in a vacuum chamber, generating plasma, by applying a high voltage between the cathode (located behind the target) and the anode (connected to the chamber). The ions impact on the target, causing the detachment of atoms of the material from it, which are then deposited onto the substrate to produce a thin film, see **Fig. 2.3a**. Nowadays, it is common the use of a magnetron (magnetron sputtering) to confine the electrons near the surface of the target, leading to higher deposition rates. Different types of sources can be used to generate the voltage difference, including DC, pulsed or radio frequency (RF), depending on the material to be deposited. It is also worth mentioning reactive sputtering, where a reactive gas such as oxygen is employed so that it chemically reacts with the sputtered material [34].

  – *Electron beam deposition*: in this process an electron beam is focused on a target, thus vaporizing atoms which then condense on the substrate generating the thin film. The process takes place in a vacuum chamber that is usually heated for improving the bonding between the coating and the substrate. Before the deposition, an ionized beam (ion beam etching) can be directed towards the substrate to remove contamination [33].

- **Chemical vapor deposition (CVD)**: this process is based on the chemical reaction of gaseous precursors on or in close proximity to a heated substrate [32]. There are several methods based on CVD, such as atomic layer deposition (ALD), plasma enhanced CVD (PECVD), photo-assisted CVD, electrochemical vapor deposition

(EVD), metal-organic CVD, flame assisted CVD, aerosol assisted CVD or electrochemical vapor deposition [32,35]. Only ALD is explained as it is the only CVD technique that has been utilized in this thesis.

– *Atomic layer deposition (ALD)*: most ALD processes are based on surface binary reaction sequences using two gaseous precursors, to which the substrate is exposed alternately, see **Fig. 2.3b**. These reactions are self-limiting, meaning that they stop once all available surface area has been covered. As a result, a binary compound film with a very controlled thickness is obtained, at the Ångstrom (10^{-10} m) or monoatomic level [36]. Its main drawback is its slow deposition rate.

  It can be distinguished between thermal ALD and plasma or radical-enhanced ALD. The first type is the most basic one. In this case, the substrate is successively and individually exposed to two reactants. It is mainly used for metal oxides, such as Al_2O_3, TiO_2 or ZnO. On the other hand, plasma ALD is used for single element materials that can be deposited in a binary sequence, such as metals and semiconductors (Si, Ge) [36].

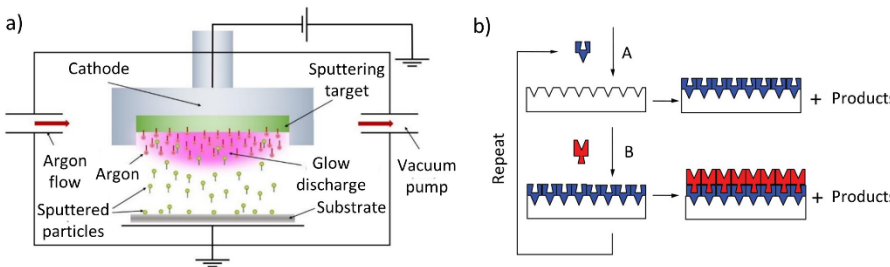

Fig. 2.3 a) Diagram of the key elements in a sputtering deposition process. Reprinted from [37]. Copyright 2010, The Authors. Published in open access b) Schematic diagram of the ALD technique. Reprinted from [36] (copyright 2010, American Chemical Society) and adapted from [38] (copyright 1996, American Chemical Society).

2.2.3. Applications

One of the most common applications in the case of LMR-based sensors has been the development of refractometers [17,18,39,40]. Nevertheless, there are also other applications including gas detection [41–45], humidity sensors [46–49], pH sensors [50–52], or biosensors [53–58].

- **Refractive index sensing**: although LMRs can be generated with both polymers and metallic oxides, most LMR based refractometers employ metallic oxides because its refractive index is higher (which increases the sensitivity [22]) and because refractometers are usually characterized with oil or glycerol solutions, which adhere to the surface of the polymer and prevent a proper testing [17].

  The best sensitivities have been achieved with the employment of a D-shaped fiber configuration, as it is the case of the following works. Regarding the water region (refractive index around 1.321), the best reported result corresponds to [39], where a sensitivity of 14.501 nm/RIU is obtained in the 1.321 - 1.326 with SnO_2. In the

same work a sensitivity of 136.276 nm/RIU is reached in the 1.4474 - 1.449 range by employing ITO, see **Fig. 2.4a**. SnO_2 is also utilized in [40], where a sensitivity of 95.012 nm/RIU is achieved with a LMR with TE polarization in the 1.4415 - 1.4447 range and a value of 829.636 nm/RIU is obtained with a LMR with TM polarization in the 1..4481 - 1.4487.

- **Gas detection**: gas monitoring has gained importance in recent years for controlling industrial processes, detecting dangerous compounds or assessing the health of patients through biomarkers present in human breath. LMR-based sensors have been developed for detecting several gases, including ammonia [41], volatile compounds (VCs) [42], hydrogen sulfide (H_2S) [43] or nitrogen oxides (NO_x) [44] among others. It is common the use of plastic multimode optical fibers, mainly PMMA (polymethyl methacrylate); and the employment of metal oxides for generating the LMR, such as ZnO [45].

- **Humidity sensing**: it could be considered a subcategory within gas detection as measuring humidity is equivalent to measuring water vapor gas concentration. The first humidity sensor based on LMR was developed in [46], employing an ITO thin film and a poly(allylamine hydrochloride) (PAH) and poly(acrylic acid) (PAA) multilayer overlay fabricated using LbL technique. Changes in the relative humidity (RH) induce thickness changes in the structure, therefore producing a wavelength shift. A sensitivity of 1.5 nm/%RH was obtained in the humidity range from 40% to 80%.

  Recent advances include the utilization of materials such as graphene oxide (GO) [47] or the employment of planar waveguides instead of optical fibers as sensing structure [48]. It is also worth mentioning the LMR-based sensor developed in [49] where gold nanoparticles (Au NPs) embedded in polymeric thin films were deposited on a cladding removed optical fiber, generating two Localized Surface Plasmon Resonances (LSPRs), associated to the Au NPs; and a LMR, whose sensitivity to the relative humidity is 11.2 nm/%RH in the 45% - 90 % range.

- **pH sensing**: pH sensors based on LMRs generally employ PAH/PAA thin films as those are weak polyelectrolytes whose degree of ionization is modified with the pH value. The thickness of the polymeric structure increases if the degree of ionization of one of the polymers is reduced and achieves its minimum if both polymers are fully ionized, thus affecting the resonance wavelength [17]. The first sensor of this type was developed in [50] by using a cladding removed multimode fiber and was studied in the 3 - 6 pH range. Subsequent sensors of this type were developed on a tapered single mode fiber [51] (studied in the 4 - 6 pH range) and a D-shaped optical fiber [52] (maximum sensitivity of 69 nm/pH unit in the 4 - 5 pH range).

- **Biosensing**: the high sensitivities achieved with LMR-based refractometers have motivated the development of biosensors based on this technology. In [53] a sensor based on a D-shaped fiber coated with SnO_2 for the detection of immunoglobulin G (IgG) achieved a limit of detection (LOD) of 0.15 ng/L (1 fM), see **Fig. 2.4b**; whereas in [54] the same structure was employed for detecting the D-dimer, a biomarker for venous thromboembolism (VTE), obtaining a LOD of 100 ng/mL, five times below the clinical cutoff value. Other biomolecules that have been

detected by means of LMRs include the Tau Protein (an Alzherimer's biomarker) [55] and perfluorooctanoic acid [56].

LMR based biosensors have also been utilized for detecting miRNAs, which are small and non-coding RNAs (ribonucleic acids) involved in the regulation of gene expression. It is the case of [57], where a miRNA associated with Huntington disease is detected or in [58], in which the same study is carried out with a miRNA linked with rheumatoid arthritis.

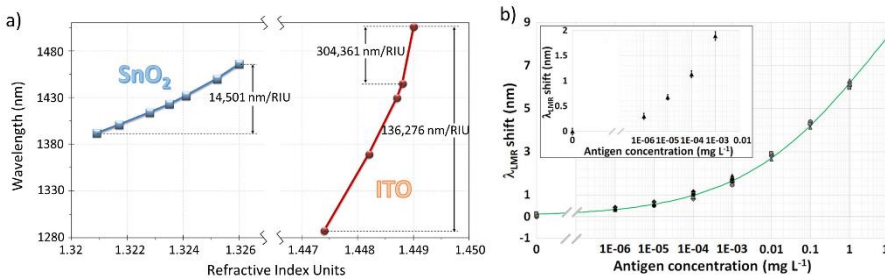

Fig. 2.4 a) Calibration curve of LMR-based refractometers using SnO_2 (water region) and ITO (1.4474 - 1.449 range) as coating materials. Reprinted from [39]. Copyright 2016, with permission from Elsevier. b) Calibration curve of an LMR-based biosensor for detecting IgG. The inset shows the enlargement of the calibration curve for the lower concentration range. Reprinted from [53]. Copyright 2018, American Chemical Society.

- **Multiparameter sensing**: multiple resonances can be obtained in the same spectrum by increasing the thickness of the thin film [30] but these resonances cannot be employed to sense different parameters as they are all associated with the same thin film. This problem has been recently overcome by the development of sensors based on planar waveguides in which several independent thin films are deposited and each one can be used for sensing a different parameter [59]. The thicknesses of the different thin films have to be controlled in order to avoid the overlap of the corresponding resonances in the spectrum.

  For instance, in [60] a LMR sensor for measuring simultaneously refractive index and temperature based on a coverslip is presented. The coverslip is coated with a CuO thin film and then partially coated with PDMS, generating two resonances in the spectrum, each of them sensitive to one of the parameters of interest. A similar approach is employed in [61] where two independent thin films are deposited on the same coverslip to develop a multirefractometer. A variant of this configuration is introduced in [62] where the thin films are deposited on both sides of the coverslip, obtaining a sensor for measuring simultaneously temperature and humidity.

  In chapter 3, it is addressed the development of LMR-based sensors for multiparameter sensing applying the same approach that is utilized in the previous works, but employing an optical fiber instead of a planar waveguide as the sensing structure.

2.3. Optical fiber gratings

Optical fiber gratings consist of a periodic modulation of the refractive index along the core of an optical fiber [13–15], typically a single mode optical fiber with a 8 µm thick core and a 125 µm thick cladding [63]. There are two main types of optical fiber gratings according to the grating period length: short period fiber grating, usually called fiber Bragg gratings (FBG) and with a period in the order of 500 nm; and long period fiber gratings (LPFG or LPG), with periods in the order of the hundreds of µm [64]. In FBGs, there is a coupling between the core mode propagating in the forward direction and counter-propagating modes; while in LPGs there is a coupling between the core mode and the co-propagating cladding modes [3]. Among FBGs, it can be distinguished between the devices where the coupling takes place between the core mode and the counter-propagating core mode (the term FBG is usually employed to refer to these devices although it is actually broader) and those where the coupling occurs between the core mode and the counter-propagating cladding modes. The latter receive the name of tilted fiber Bragg gratings (TFBG) [65,66] as the gratings are angled with respect to the perpendicular to the optical fiber axis in order to achieve this coupling. Due to their importance, TFBGs are considered most of the time a category on their own instead of a subtype of FBGs.

2.3.1. FBGs

FBGs are characterized for presenting a narrow band in the reflection spectrum (seen as a dip in the transmission spectrum), known as the Bragg resonance, which is centered on the Bragg wavelength (λ_B), given by the phase matching condition:

$$\lambda_B = 2 \cdot n_{core}(\lambda_B) \cdot \Lambda \tag{2.4}$$

where n_{core} (λ_B) is the effective refractive index of the core mode at the Bragg wavelength (close to the refractive index of silica, 1.44 at 1550 nm [19]) and Λ is the grating period or grating pitch. The schematic representation of an FBG as well as the transmission and reflection spectra of an FBG approximately centered at 1560 nm can be observed in **Fig. 2.5**. The Bragg resonance is visible in both the transmission and the reflection spectra.

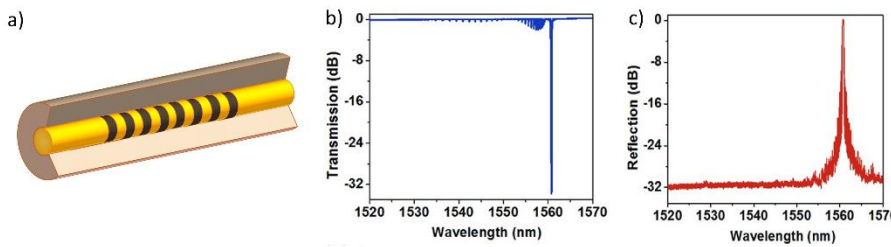

Fig. 2.5. a) Schematic representation of a fiber Bragg grating (FBG). b) Transmission spectrum of an FBG. c) Reflection spectrum of an FBG. b), c) reproduced from [65]. Copyright 2012, WILEY-VCH Verlag GmbH & Co. KGaA, Weinheim.

Both the effective refractive index of the core and the grating period are affected by changes in strain and temperature, therefore causing a shift of the Bragg wavelength.

The sensitivities for a Bragg resonance located at approximately 1550 nm to the strain and the temperature are 1.2 pm per 1 με (1 με = 1 μm/m) and 13.7 pm/ºC respectively [15]. On the other hand, FBGs are not sensitive to SRI variation, since light coupling occurs between core modes and the core is separated from the external medium by the fiber cladding [3].

2.3.1.1. Fabrication techniques

The externally written fabrication techniques for inscribing Bragg gratings in photosensitive optical fibers include the interferometric technique [67], the phase-mask technique [68,69] and the point-by-point technique [70,71].

- **Interferometric technique**: it employs an interferometer that splits the incident ultraviolet (UV) into two beams and them recombines them to create an interference pattern. The optical fiber is exposed to this pattern, therefore producing a refractive index modulation of the core [15]. Two types of interferometers have been used: the amplitude splitting interferometer and the wave-front splitting interferometer. In the first case, the UV incident light is divided into two equal intensity beams and then they are recombined after travelling through two different optical paths. The main advantage of this technique is that the Bragg wavelength can be easily tuned by varying the intersecting angle between the two beams, while the most important drawback is that the setup is highly affected by mechanical vibrations. With respect to wave-front splitting interferometers, they include the prism interferometer [72] and Lloyd's interferometer [73], see **Fig. 2.6a**. They are less sensitive to vibrations than amplitude splitting interferometers as they only utilize one optical component, but both the grating length and the wavelength tunability are limited in these setups. Finally, one disadvantage that is common to all interferometric methods is that the laser sources must have good temporal and spatial coherence [15].

- **Phase mask technique**: the mask consists of a flat slab of silica glass in which one of the flat surfaces has been etched by means of photolithographic techniques in order to create a one dimensional periodic surface relief structure [68,69]. The optical fiber in which the grating is going to be inscribed is placed close to the surface of the slab where the relief structure has been etched. The manufacturing process consists in illuminating the phase mask with UV light (KrF excimer lasers are the most common sources [15]), which propagates through the mask (transparent to UV light) and is diffracted by its periodic corrugations. The depth of the corrugations is chosen so the diffraction into the zero-order is almost suppressed and the ± 1 diffracted order beams produce a periodic pattern that is photoimprinted in the optical fiber, creating the gratings, as it can be observed in **Fig. 2.6b**. The period of the fiber gratings is half the period of the mask gratings [68]. The advantages of the phase mask technique include easy alignment of the fiber, no critical dependence on the stability of the setup or the coherence of the UV laser beam (as it happened in the interferometric methods), and the possibility of manufacturing the gratings on several fibers at the same time by placing them in parallel under the phase mask [68].

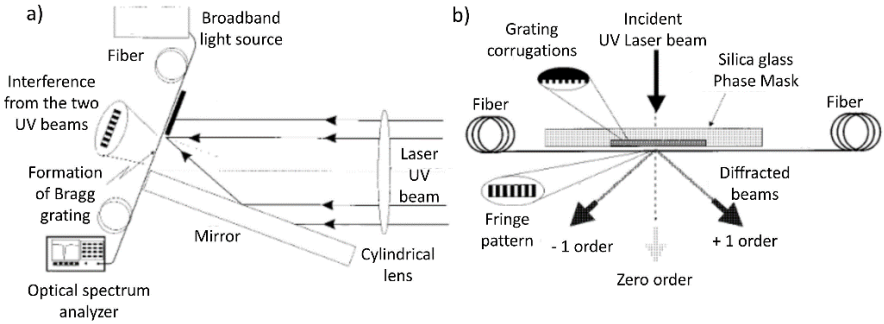

Fig. 2.6. a) Schematic of Lloyd interferometer for fabricating fiber Bragg gratings. b) Schematic of the phase mask technique for photoimprinting an FBG. a), b) reproduced from [15]. Copyright 1997, AIP Publishing.

- **Point-by-point technique**: one grating period is fabricated at a time, as opposed to the phase mask technique. A small section of the optical fiber is exposed from the side to a collimated beam of UV light passing through a mask containing a slit whose width is typically equal to half the grating period Λ. The incident light slightly increases the refractive index of the core in the exposed fiber section. This way, one grating period is manufactured. The fiber is then displaced along its axis a distance equal to Λ and the exposure step is repeated [71]. This process continues until the required number of gratings has been manufactured. The main advantage of the point-by-point technique is the flexibility, making easy to introduce variations in grating length, grating period, and spectral response; while the most important drawback is that it is not a practical method to manufacture grating with an important number of periods [15,68,71].

The previously described techniques can also be employed with a femtosecond laser source (a laser that emits pulses with a duration in the order of the femtoseconds, with 1 fs = 10^{-15}s) instead of an UV laser [74]. The advantages of femtosecond lasers include their flexibility in producing different FBG configurations, the fact that they do not require the fibers to be photosensitive for inducing a refractive index modulation and the stability of the manufactured FBGs at high temperatures, which makes them ideal for sensing applications in harsh environments [75].

2.3.1.2. Classification of FBGs

In order to do a first classification of the FBGs, it is necessary to introduce the concept of photosensitivity. Photosensitivity can be understood as the change in the refractive index of the core produced after the exposure of UV light, with a higher photosensitivity causing a larger change [15]. The interest in increasing this change is due to the fact that it leads to a higher reflectivity of the Bragg resonance, although it also broadens the peak. The methods for increasing the photosensitivity include hydrogen loading or hydrogenation (diffusing hydrogen molecules into fiber cores at high pressures and temperatures), flame brushing (diffusing hydrogen into the core by means of a hydrogen-rich flame that is brushed over the fiber), boron codoping (addition of boron to the core of the fibers) or employing ArF excimer lasers [15].

Depending on the photosensitivity of the fiber and the writing conditions of the gratings, FBGs can be classified into [74,76–78]:

- **Type I**: standard gratings with a low refractive index modulation (in the order of 10^{-5}), generated when the pulse energy of the writing UV beam is below approximately 30 mJ, which is the threshold that enables to distinguish between type I and type II gratings [15]. They are fabricated in most types of germanosilicate fibers. The refractive index change associated with this process is usually positive.
  - *Type IH*: similar to type I, these gratings are manufactured in hydrogenated fibers to enhance the photosensitivity thus the strength of the grating [74].
  - *Type IHp* (formerly Type IA): gratings written after the generation and erasure of a Type I grating in a hydrogenated fiber [19]. Initially, a Type I grating is generated and the Bragg resonance increases in strength and shifts towards the red. Then, if the UV exposure continues, the index variation saturates and the grating decreases in strength. After a while, a Type IHp grating is formed, with the Bragg resonance regaining in strength and shifting towards the red. The refractive index change is in the order of 10^{-2} higher than that of the initial type I grating [79]. These gratings stand out for having a lower temperature sensitivity than the other types (7 pm/ºC) [19].
  - *Type In* (formerly Type IIA): gratings written after the generation and erasure of a Type I grating (like type IHp gratings) in a hydrogen-free germanosilicate fiber [19]. The generation process is the same that has been described for Type IHp gratings, but after the saturation the Bragg wavelength increases in strength but shifts towards the blue [80].
  - *Type IHs* (hypersensitized): grating made in a fiber that has been pretreated to maintain the photosensitivity increase gained with hydrogenation [74] (in normal cases this is not a permanent effect, as the hydrogen diffuses out [15]).
  - *Type Id*: gratings written with a 193 nm ArF laser operating just below the damage threshold of the glass. They do not require the use of a doped fiber. They usually have higher scattering losses than other Type I gratings but lower than the Type II gratings [74].
- **Type II**: gratings with a high refractive index modulation (in the order of 10^{-3}, achieving values up to 0.006) created with a pulse energy of the writing beam above 30 mJ. In these type of gratings, it is characteristic the presence of damage in the core-cladding interface. Type II gratings produce resonances with high reflectivity and large bandwidth, as expected for a high modulation [15]. Other important feature is that they are stable up to 1000ºC, much higher than Type I gratings.
- **Regenerated gratings**: gratings produced after subjecting a Type I grating to an annealing process at temperatures of 1000ºC. The original grating is erased and a new grating generates at a longer wavelength, gaining in strength and shifting towards the red during the rest of the process [81]. Their reflection peak is weak but they are stable at temperatures up to 1000ºC, so they are gaining importance in extreme sensing applications [74].

A second classification of FBGs can be done based on the refractive index modulation done in the core of the fiber [13,76,82]:

- **Uniform FBG**: the core refractive index modulation and the grating period are constant, see **Fig. 2.7a**. It is the basic case that has been analyzed until this point, producing a narrow band in the reflection spectrum.

- **Apodised FBG**: the core refractive index is modulated with a certain function, such as a Gaussian-apodised grating (see **Fig. 2.7b**) or raise-cosine apodised gratings. This way, the side lobes surrounding the Bragg resonance in an uniform grating can be suppressed or greatly attenuated, as in the zero DC case in **Fig. 2.7b**. Nevertheless, if the apodisation implies a change in the mean value of the effective refractive index of the core in the grating region, sides lobes appear again. A positive index change causes a side lobe on the short wavelength end while a negative index change produces a side lobe on the long wavelength one [82] and the latter can be observed for the non-zero DC case in **Fig. 2.7b**.

- **Chirped FBG**: the grating period varies along the grating length, typically in a linear trend, see **Fig. 2.7c**. As a result, the Bragg wavelength changes along the grating, since each part of the grating reflects a different spectrum. Therefore, the reflected spectrum is broader than in uniform FBGs, with a full width half maximum (FWHM) that ranges between a few and tens of nanometers [83]. The most important feature of chirped FBGs compared with uniform FBGs is that the spectrum depends on the temperature/strain distribution along the grating, so they do not only measure these variables, but they also detect the point where they change [84].

- **Phase-shifted FBG**: a phase shift is introduced in the core refractive index modulation, producing a spectral notch in the reflected spectrum or, what is the same, a narrow band transmission filter, as it can be observed in **Fig. 2.7d**. The position of the resonance wavelength depends on the value of the phase change [85].

- **Sampled or superstructured grating**: the effective refractive index or the grating pitch are varied at intervals with a period much larger than the nominal grating period, conforming a periodic "superstructure" [82], see **Fig. 2.7e**. As a result, these gratings possess side-band resonances that are equally spaced in frequency around the fundamental resonance [13]. If the period of the superstructure is Λ_S, the wavelength spacing of the side-band resonances $\Delta\lambda_S$ is calculated as [86]:

$$\Delta\lambda_S \approx \frac{\lambda_B^2}{2 \cdot n_{core}(\lambda_B) \cdot \Lambda_S} \tag{2.5}$$

- **Eccentric FBG**: they have been included in this classification in absence of a better place, although they are not typically considered part of it. In eccentric FBGs, also called highly localized FBGs, the refractive index modulation is shifted from the fiber core center and is only done in part of the core section. As a result, there is a coupling between the core mode and the counter-propagating cladding modes, as in TFBGs. Therefore, its spectrum consists of hundreds of cladding mode

resonances spreading over several hundred nanometers, from the Bragg wavelength to the cut-off wavelength, that corresponds to the resonance whose effective refractive index matches that of the surrounding medium [63,87].

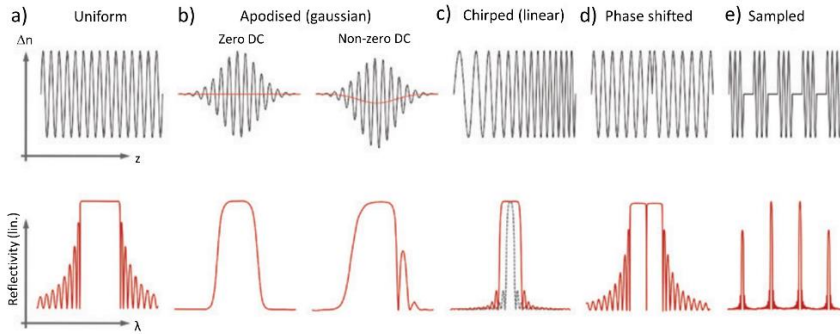

Fig. 2.7 Types of gratings according to the refractive index modulation (top) and the corresponding reflection spectra (bottom): a) uniform, b) Gaussian-apodised (red lines in the refractive index profile indicate the average change), c) chirped (linear), d) phase shifted, e) sampled or superstructured. Reproduced under the terms of the Creative Commons Attribution-Non Commercial 3.0 Unported License [82]. Copyright 2017, the Authors.

2.3.1.3. Applications

The main variables measured with FBGs are temperature [88,89] and strain [90–92]. However, other variables such as pressure [93–96], liquid level [97–99], or displacement [100] can also be measured by the translation of these parameters into an axial strain applied to the fiber. Finally, although it is necessary to reduce or remove the fiber cladding, sensors based on FBGs for measuring the SRI [101–103], or biosensing applications [104–108] have also been developed.

- **Temperature sensing**: the development of temperature sensors is one of the most basic applications of FBGs [88,89]. Nowadays, efforts regarding temperature sensing with FBGs are focused in developing sensors for extreme temperatures (higher than 1000ºC or cryogenic) for applications such as power plants, turbines, combustion or aeronautics [76,109].

  Techniques to develop high temperature resistant FBGs include modifying the glass composition, thermal annealing or cycling processes or inscribing grating by means of femtosecond infrared lasers (the previously explained inscription techniques are based on UV photosensitivity) [110,111]. Silica fiber can be used in applications for measuring up to 1000ºC, whereas sapphire fibers are employed for higher temperatures [109]. In [112], FBGs written in sapphire fibers are employed to measure temperatures up to 1745ºC with repeatability better than 1ºC, while in [113] the same type of fibers are used to measure temperatures up to 1900ºC and temperature distribution is studied in an inductive furnace at 1500ºC.

  Regarding cryogenic temperatures, the thermal coefficient of silica tends to 0 at 4 K, so metal coatings are employed for enabling measurements at these temperatures [114,115]. In [114], the best results are obtained with a Pb electrocoated FBG, with

a sensitivity of 8.7 pm/K in the 4.2 - 35 K range. Additional cryogenic sensors have been developed in recent years. Although the latter do not achieve temperatures as low as 5 K, they cover a wide range (up to ambient temperature) with a good sensitivity. In [116], a TiN coated FBG is able to measure temperatures in the -195 ºC (78 K) - 25ºC range with 10.7 pm/ºC sensitivity, while in [117] a sensitivity of 48 pm/ºC is achieved in the -180ºC (93 K) - 25ºC range with a polymer-coated FBG that measures strain simultaneously.

- **Strain sensing**: as in the case of temperature, measuring strain is a common use of FBGs, as it is demonstrated by the existence of several reviews about this topic [90–92]. Nowadays, strain sensors based on FBGs have acquired importance thanks to their utilization in structural health monitoring (SHM) applications, that is, a set techniques implemented for damage detection in aerospace, civil and mechanical engineering infrastructures [118]. FBGs are embedded in reinforced concrete beams, composite materials or piles or in structures such as bridges for monitoring strain. They are encapsulated to ensure their durability. It is common the use of different methods, such as a second FBG, to compensate the effect of the temperature change on the Bragg wavelength [90].

- **Pressure sensing**: when a fiber is compressed, it suffers an axial strain, therefore pressure can be measured with an FBG. One of the first sensors of this type was developed in [93], with a linear sensitivity of -3 pm/MPa in the 0 - 70 MPa range. The sensitivity can be increased by using coatings, such as a carbon fiber laminated composite in [94] (sensitivity of 100 pm/MPa in the 0 - 70 MPa). Sensitivity has been further increased by employing differential FBG sensors, as in [95] (340 pm/MPa in the 0 - 10 MPa range, including temperature compensation and based on a diaphragm-cantilever structure, see **Fig. 2.8**) and [96] (821.87 pm/MPa in the -11.6 – 11.6 MPa range, also measuring temperature), although the dynamic range is reduced compared with previous sensors.

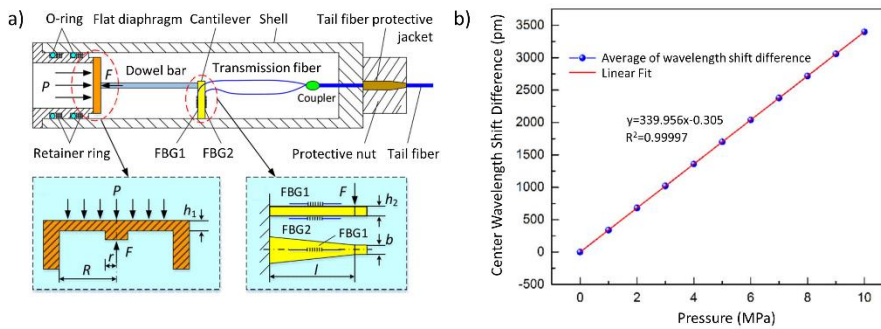

Fig. 2.8 a) Schematic diagram of the FBG pressure sensor including detailed diagrams of the flat diaphragm and the cantilever. b) Average difference values for several essays in the wavelength shifts between the two FBGs under pressure values ranging from 0 to 10 MPa. Reproduced from [95]. Copyright 2017, with permission from Elsevier.

It is also worth mentioning the employment of FBGs inscribed in air-hole fibers for measuring high temperatures and pressures simultaneously [109]. When applying

an external pressure to the fiber, the air holes suffer a deformation, producing internal stress inside the fiber and inducing birefringence, which separates the FBG peaks for both polarization states. These two peaks are used for sensing both the temperature and the pressure. This structure has been employed both with Type II [119] (0.1 - 13.8 MPa range for temperatures above 800 ºC) and regenerated gratings [120] (0.1 - 16.5 MPa range for temperatures in the 24 - 800 ºC range), that correspond to the FBG types that support high temperatures.

- **Liquid level sensing**: there are two basic options when measuring the liquid level with FBGs [121]. The first one is to measure the wavelength shift produced by the SRI change that takes place when the FBG is progressively submerged in the liquid, although the measurement level range is limited to the grating physical length. An example is found in [97], where a chirped FBG is employed, achieving a high sensitivity of 1214 pm/nm but only having a level range of 5.6 mm. The second option are the pressure based sensors, where the liquid level is measured through the subsequent change in pressure, that causes a strain in the fiber, affecting the Bragg wavelength. The sensors are encapsulated in different kinds of structures, including diaphragms, as in [98,99], with sensitivities lower than 3 pm/mm but level ranges between 0.5 and 1 m.
- **Displacement sensing**: measuring displacement is important in the field of structural health monitoring, in structures, such as buildings, dams or bridges [76]. In this case, sensors are designed so the displacement causes a deformation of a certain element and this produces a strain on the FBG, generating a shift of the Bragg wavelength. It is common the use of cantilever structures or springs in this type of sensors [122]. For example, in [100] an FBG is employed combined with a wedge-shaped sliding block a T-shaped cantilever beam to measure displacements up to 2 mm with a sensitivity of 2086.27 pm/mm in the 1 mm - 2 mm range and a resolution of 0.48 µm, see **Fig. 2.9**.

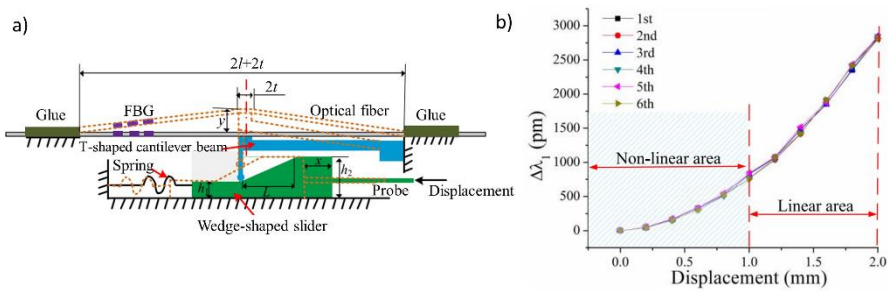

Fig. 2.9 a) Schematic diagram of the FBG displacement sensor. b) Wavelength shift of the FBG for several essays for displacements in the range 0 - 2 mm. The sensitivity in the linear range is 2086.27 pm/mm. Reproduced from [100]. Copyright 2017, IEEE.

- **Refractive index (RI) sensing**: FBGs are insensitive to the surrounding medium refractive index (SRI), as previously mentioned. Nevertheless, by reducing the cladding thickness by means of etching methods, the evanescent field of the core mode begins to penetrate the surrounding medium, therefore inducing a sensitivity to the SRI [3]. The first sensor of this type was developed in [101], etching the fiber

diameter down to 11 µm and achieving a poor sensitivity of 0.087 nm/RIU. The sensitivity is improved by further reducing the fiber diameter, as in [102] (sensitivity of 16 nm/RIU for a diameter of 8.5 µm) and [103] (sensitivity of 237.5 nm/RIU for a diameter of 3 µm, etching both the cladding and an important part of the core) but the obtained values are still far from the results achieved with other technologies. It must also be considered that the fiber becomes more fragile when further etching the fiber.

- **Biosensing**: the limitations of FBGs regarding RI sensing condition the development of biosensors, based on measuring a surface RI change. Therefore it is necessary to reduce or remove the fiber cladding through etching or polishing, or directly write FBGs in microfibers (fibers with a diameter of a few µm) in order to manufacture biosensors based on FBGs [123].

  Sridevi *et al*. have developed several biosensors based on etched FBGs and functionalized with graphene oxide or reduced graphene oxide for the detection of different biomarkers, such as C-reactive protein [104], protein concanavalin A [105], glucose and glycated hemoglobin [106]. C-reactive protein is also detected in [107] by means of a femtosecond-pulsed laser written and etched FBG, but improving the detection limit in [104] by more than 6 orders of magnitude (0.82 pg/L in [107] vs 10 µg/L in [104]). Another biosensor based on an etched FBG is reported in [108], where thrombin is detected after applying a silanization process to the fiber. On the other hand, Bertucci *et al*. have manufactured several sensors for detecting DNA sequences by using FBGs inscribed on microstructured optical fibers and functionalized with peptide nucleic acids [124,125].

- **Multiparameter sensing**: common FBG multiparameter sensors are designed to measure temperature and a second magnitude that is usually strain or a variable that is connected with strain such as pressure, bending or displacement. The sensor design is usually based on a configuration with two FBGs whose sensitivities to the variables of interest are different [126]. The purpose of measuring the temperature can be the temperature on itself or compensating the temperature drift when measuring the other variable. Another possibility of multiparameter FBG sensing is measuring simultaneously the SRI and the temperature [127,128]. In this case, an FBG is made sensitive to the SRI by polishing or etching the fiber while a second FBG is inscribed in a standard SMF section and only measures the temperature. This possibility, but employing an LMR for measuring the SRI instead of an FBG, is explored in chapter 3.

2.3.2. LPGs

In LPGs, there is a coupling between the core mode and the co-propagating cladding modes. The high attenuation of the cladding modes leads to the appearance of attenuation bands in the transmission spectrum, each one corresponding to the coupling to a different cladding mode [129], see **Fig. 2.10b**. The position of each attenuation band is given by the phase matching condition:

$$\lambda = \left(n_{core}(\lambda) - n^{i}_{cladding}(\lambda)\right) \cdot \Lambda \tag{2.6}$$

where $n_{core}\ (\lambda)$ is the effective refractive index of the core mode at λ, $n^{i}_{cladding}\ (\lambda)$ is the effective refractive index of the ith cladding mode at λ, and Λ is the grating period. The grating period has typically a value between 100 μm and 1 mm.

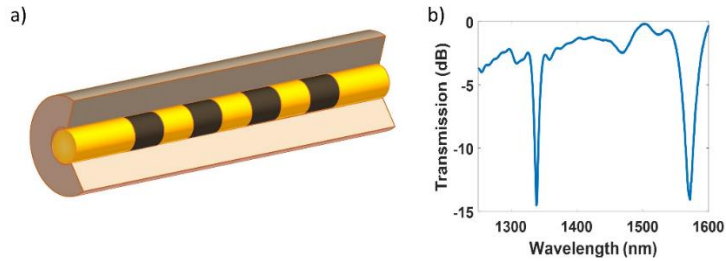

Fig. 2.10 a) Schematic representation of a long period grating (LPG). b) Transmission spectrum of an LPG.

In this case of LPGs, it is important the description of two phenomena that enable an increase in sensitivity: the dispersion turning point (DTP) (also known as turn-around point (TAP) or phase matching turning point (PMTP)) and the mode transition.

The dispersion turning point was proposed for the first time in [130] and is connected with the appearance of two resonances in the transmission spectrum linked with a single cladding mode. This phenomenon can be better understood if equation (2.6) is graphically represented. By using equation (2.6), it can be calculated the theoretical grating period that produces a resonance at a certain wavelength for a certain cladding mode i by simply simulating $n_{core}\ (\lambda)$ and $n^{i}_{cladding}\ (\lambda)$ and solving Λ. Then, the resonance wavelength can be plotted as a function of the grating period for each cladding mode, as it has been done in **Fig. 2.11a** for a standard single-mode fiber.

In general, it can be observed that for a grating period value (graphically a vertical line) and each cladding mode curve, there is only one wavelength that verifies the equation (one intersection point). However, for high order cladding modes, there are grating period values that produce two intersection points, therefore two resonances, that is, the dispersion turning point. For instance, this happens in **Fig. 2.11a** for the 11^{th} cladding mode and a period of approximately 190 μm. Each of these resonances possesses a very high sensitivity and shifts in a different direction as a function of the refractive index, as it can be observed in **Fig. 2.11b**. Therefore, sometimes their separation is employed as a parameter for sensitivity instead of the shift of a single resonance, leading to sensitivities that are approximately the double [3]. More information will be given in the applications subsection.

Regarding the mode transition, the term was introduced in [131], although this phenomenon was first observed in [132]. In this work, a thin film with a higher refractive index than that of the cladding was deposited on an optical fiber with an LPG written on its core, producing a wavelength shift and an amplitude change of the attenuation bands as a function of its thickness.

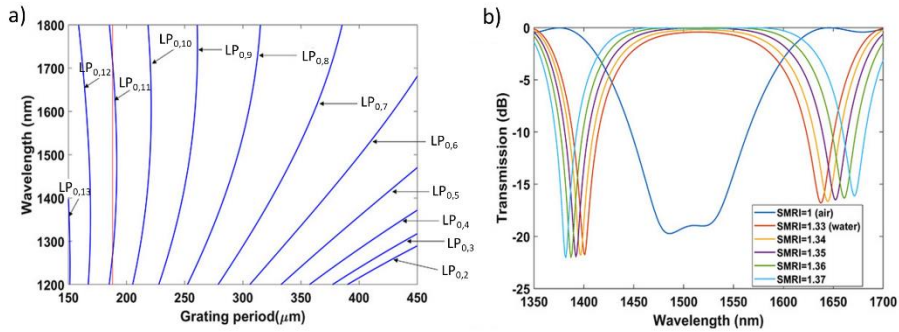

Fig. 2.11 Simulation with FIMMWAVE software of an LPG written on a standard single-mode fiber. a) Calculated variation of resonance wavelength with grating period. b) Transmission for LPG working at DTP immersed in different SRIs. Reproduced from [3]. Copyright 2019, WILEY-VCH Verlag GmbH & Co. KGaA, Weinheim.

It was later demonstrated that the wavelength shift is caused by the gradual transfer of energy from a cladding mode to a leaky mode of the thin film as it becomes thick enough to support one, causing a reorganization of the cladding modes. Each cladding mode *i* shifts its effective refractive index value towards the effective index of the immediate lower order cladding mode *i-1* [133,134]. Both effects can be observed in **Fig. 2.12a** where mode transitions take place at thicknesses of 300, 1200, 2100 and 3000 nm and modes $LP_{0,2}$, $LP_{0,3}$, $LP_{0,4}$, $LP_{0,5}$ become guided respectively, causing at each transition a reorganization of the remaining modes. The range of thicknesses where this effect takes place is also connected with an apparent fiber mode loss (a decrease of the amplitude of the grating resonance) since the power transfer from the fiber core to the coating reduces the power density in the fiber core and consequently the coupling coefficient of the grating. The term "Lossy Mode Resonance" (LMR) can be used to describe such effects [17].

Furthermore, the fast shift of the cladding modes effective index in this region leads to an increase in the sensitivity of the attenuation bands (both are linked through the phase matching equation (2.6)), which was demonstrated in [134]. This can be observed in **Fig. 2.12b**, in which the fastest wavelength shift of the resonances occurs for a thin film thickness of around 300 nm, which corresponds to the mode transition in this work [133]. It can also be noted that each resonance shifts until reaching the original position of the resonance corresponding to the immediately lower cladding mode.

Nevertheless, the first works on this phenomenon had to face the problem that the resonances faded during the transition because the deposition techniques employed (Langmuir Blodgett and Layer by Layer self-assembly) produced coatings with strong losses [132,133]. This problem can also be appreciated in **Fig. 2.12b**, where there are almost no experimental points in the mode transition region. This obstacle was solved by using the dip coating technique, which provided higher quality films, demonstrating the applicability for sensing [135].

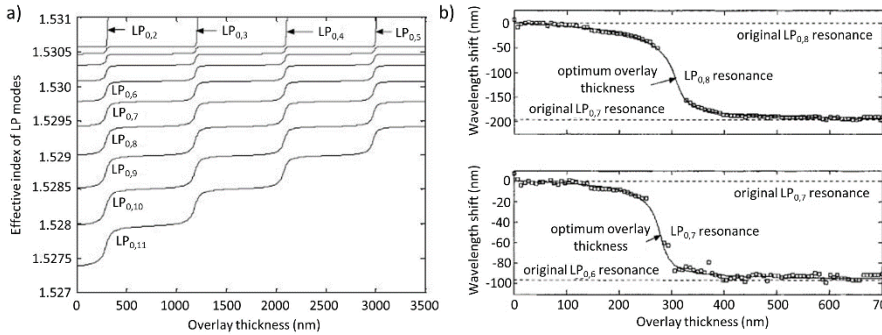

Fig. 2.12 a) Effective index evolution as a function of the thin film thickness (refractive index value 1.67) for the first ten cladding modes in a standard single-mode fiber at 1200 nm. Reproduced under an Open Access License [134]. Copyright 2005, Optica Publishing Group. b) Shift in the wavelength of the resonances associated to the 8th (top) and the 7th (bottom) cladding modes as a function of the thin film thickness (refractive index value 1.62) in a standard single-mode fiber. Open squares, experimental values; solid curves, theoretical values. Reproduced from [133]. Copyright 2005, Optica Publishing Group.

Before finishing this section, it is worth mentioning the existence of helical long period gratings (HLPGs), which have a periodic spiral refractive index modulation along the axis direction, as opposed to conventional LPGs [136]. Helical structures are generally manufactured by twisting and/or heating the optical fiber. Their main difference with standard LPGs is that they are more sensitive to torsion [137], being torsion sensors one of their main applications [136].

2.3.2.1. Fabrication techniques

The most common method for manufacturing LPGs is UV irradiation (using for instance KrF excimer lasers), being the main techniques the phase mask technique, the point-by-point technique, and interferometry; which have already been described in the case of FBGs [129]. However, there are other methods including: ion implantation [138], irradiation by femtosecond laser pulses (already explained for FBGs) [139], irradiation by CO_2 lasers [140,141], electrical arc discharge [142], etching [143] and mechanically induced gratings [144]. The methods that have not been aforementioned will be described below these lines.

- **Ion implantation**: the method consists in implanting protons (H^+) or He^{2+} ions in the core of the optical fiber, producing a refractive index modulation due to the densification of the silica glass. This densification is induced by the atomic collisions through which the implanted ions lose their energy. The refractive index increase achieved by ion implantation is in the order of 10^{-2} [138].
- **Irradiation by CO_2 lasers**: in the case of conventional glass fibers, the method consists in periodically irradiating with a CO_2 laser sections of the fiber, which is progressively moved along its axis direction, that is, a point-by-point technique. The main mechanisms behind the refractive index modulation in LPGs inscribed with a CO_2 laser are residual stress relaxation, glass densification and physical deformation [140,141]. A schematic diagram of a setup for inscribing LPGs by irradiation with a CO_2 laser can be observed in **Fig. 2.13a**.

- **Electrical arc discharge**: an uncoated fiber is placed between the electrodes of a splicing machine, being subjected to an electric current between 7 and 15 mA during a time interval of 200 ms - 2s. This way one grating period is manufactured. Then the fiber is displaced a distance equal to the grating period and the process is repeated, continuing until the required number of periods has been fabricated. The mechanisms that play a role in the refractive index modulation produced during the arc discharge are residual stress relaxation, glass densification and microdeformations [142]. An example of setup to manufacture arc-induced LPGs is shown in **Fig. 2.13b**.

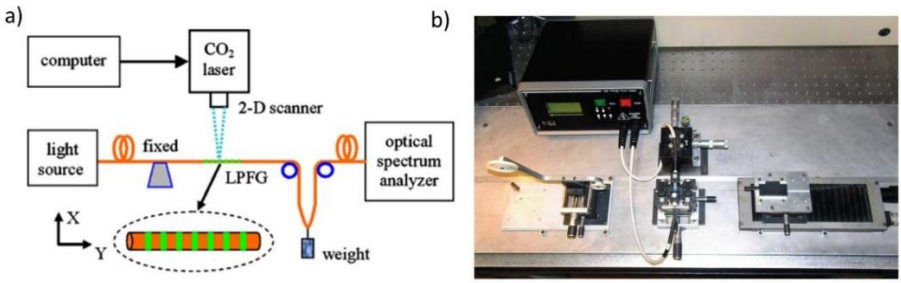

Fig. 2.13 a) Schematic diagram of an LPG fabrication system based on two-dimensional scanning of focused high-frequency CO_2 laser pulses. Reproduced from [141] (copyright 2010, AIP Publishing), adapted from [145] (copyright 2003, IEEE). b) Experimental set-up used to fabricate arc-induced LPGs. Reproduced under the terms of the Creative Commons Attribution 4.0 International License [142]. Copyright 2016, the Authors.

- **Etching**: a corrugated structure is obtained by chemically etching sections of the cladding that are periodically spaced. This is achieved by protecting some sections of the cladding with a metallic thin layer while leaving others uncoated, which will be the ones that will be etched when immersing the fiber in a hydrofluoric acid solution. The refractive index modulation is low unless the etching removes almost all the cladding. Nevertheless, the index modulation can be increased by applying stress [143].
- **Mechanically induced gratings**: the refractive index modulation can be mechanically induced by, for instance, pressing the fiber between a periodically grooved plate and a flat plate. The pressure points produce a periodic index modulation due to the photoelastic effect [144].

2.3.2.2. Applications

Sensors with similar applications as the ones described for FBGs can be developed with LPGs. Attention will be focused on temperature [146–148] and strain sensing [149–151] (basic variables to which LPGs are also sensitive) as well as on SRI sensing [152–155] and biosensing [123,156–159], applications that lately attract much attention. However, there are also sensors based on LPGs for measuring pressure [160], liquid level [161] or displacement [162], among others.

- **Temperature sensing**: the magnitude and sign of the temperature sensitivity of an LPG depend on the material of the fiber, the grating period and the order of the cladding mode that is associated to the resonance, being possible to produce attenuations band that are not sensitive to temperature [129]. Typical values in a single mode fiber range from 30 pm/ºC to 90 pm/ºC [163], higher than in FBGs (13.7 pm/ºC [15]). Methods to increase the temperature sensitivity include the use of different fiber compositions, geometries or the employment of polymer coatings [129].

  For example, in [146] the temperature sensitivity of LPGs in boron germanium fibers codoped fibers is studied in the 0 - 60ºC range for different grating periods (from 34 to 550 μm) and cladding modes (from 5th to 30th), obtaining sensitivities with different sign ranging in absolute value from 75 pm/ºC to 1750 pm/ºC. The employment of a polymer coating to enhance the temperature sensitivity is shown in [147], where a PDMS coated LPG achieves a sensitivity of 255.4 pm/ºC in the 20 - 80 ºC range. Finally, in [148] it is proposed a temperature sensor based on an isopropanol filled photonic crystal fiber (PCF) LPG, where a sensitivity of -1356 pm/ºC is achieved in the 20 - 50 ºC range. The air holes of the PCF are filled with isopropanol in order to improve the sensitivity (around 150 times compared with the air filled PCF-LPG), as this liquid possesses a high thermo-optic coefficient.

- **Strain sensing**: as in the case of the temperature, the strain sensitivity of an LPG depends on the material of the fiber, the grating period and the order of the cladding mode, being possible to generate attenuation bands with positive, negative or zero sensitivity to strain [129].

  In recent years, high strain sensitivities are achieved by using different fiber geometries and particular methods for inscribing the gratings. For instance, in [149] a sensitivity of -5.62 pm/με is achieved with an inflated LPG, obtained by inflating periodically air holes along the axis of a solid core PCF with a CO_2 laser. In [150] periodic grooves are carved on the surface of a large-mode-area PCF, producing an LPG with a strain sensitivity of -7.6 pm/με. A similar strategy to generate the LPG is followed in [151] but in this case there is an angle rotation (6º/mm) between consecutive grooves, reaching a linear sensitivity of 106.7 pm/με in the range 0 - 600 με.

  It is also worth mentioning that the sensitivity of LPGs to transverse strains and torsion has also been studied [129]. When a transverse load is applied to an LPG, birefringence is induced in the fiber. The separation between the resonances corresponding to each polarization depends on the transverse load, thus it can be used to develop a sensor [164]. Torsion has been analyzed in corrugated LPGs, where axial strain produces a change only in the resonance loss while torsion affects both the wavelength and the amplitude of the attenuation band [165]; and in LPGs written with CO_2 lasers, where both the twist rate and the twist direction can be determined [166], see **Fig. 2.14**.

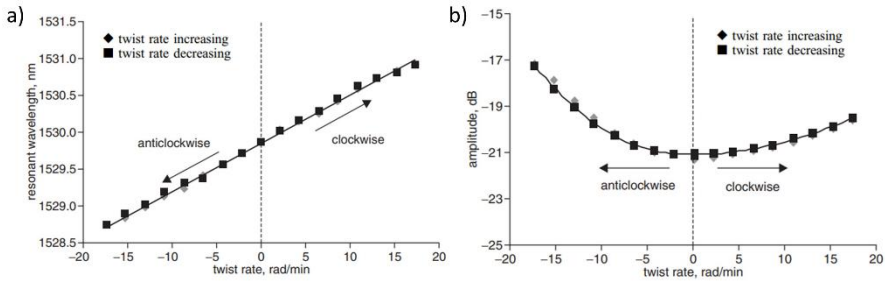

Fig. 2.14 a) Resonance wavelength shift vs twist rate applied. b) Amplitude of the attenuation band vs twist rate applied. Reproduced from [166]. Copyright 2004, The Institution of Engineering and Technology.

- **Refractive index sensing**: three phenomena (individually or combined) are generally employed to enhance the SRI sensitivity in the case of LPGs: the dispersion turning point, (DTP) the mode transition (both have been previously explained in the introduction about LPGs) and etching, which was already a method for enhancing the SRI sensitivity in the case of FBGs. In the case of the DTP, sensitivity is usually calculated considering the separation between the two peaks as a function of the SRI.

  An example of the combination of these phenomena is found in [153], in which the DTP and etching are employed together to obtain a 16.044 nm/RIU sensitivity in the 1.333 - 1.3335 range (see **Fig. 2.15a**). Also, in [154], the DTP and the mode transition (obtained through the deposition of TiO_2 thin films) are combined to optimize the sensitivity in specific SRI ranges, achieving for example a sensitivity of 10.000 nm/RIU in the 1.336 - 1.3397 range and a sensitivity of 42.000 nm/RIU in the 1.4526 - 1.4561 with different grating periods and thin film thicknesses. In [155], the combination of all three phenomena (DTP, mode transition and etching) in a single LPG is studied, and a sensitivity of 40.000 nm/RIU for SRI = 1.41 is reached considering only a single band.

- **Biosensing**: the techniques that are employed to enhance the performance of the biosensors are the mode transition and the DTP, being the latter the most utilized one [123,156]. For instance, in [157] a biosensor is developed based on an LPG operating at the mode transition (thanks to a thin film of atactic polystyrene with a suitable thickness) for the detection of anti-human IgG. In [158], goat anti-mouse IgG is detected employing an LPG working at the DTP, achieving a limit of detection of 70 µg/L in human serum (see **Fig. 2.15b**). Regarding LPG-based biosensors for detecting anti-IgG, it is also worth mentioning the work described in [159], where another strategy is used, that is, inscribing the LPG in a photonic crystal fiber (PCF) for detecting anti-mouse IgG. Biosensors based on LPGs have been developed for the detection of different targets, including the previously mentioned anti-IgG, BSA (bovine serum albumin), glucose, *Escherichia coli* or DNA sequences [156].

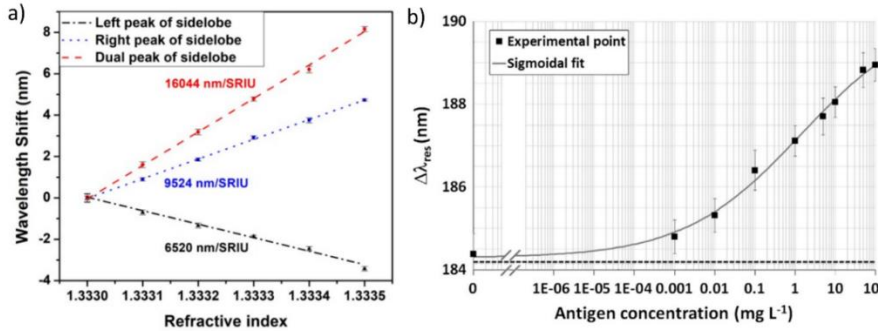

Fig. 2.15 a) Sensitivity analysis of the sidelobes of cladding mode $LP_{0,2}$ at the dispersion turning point (DTP). The greatest sensitivity (16.044 nm/RIU) is achieved if the separation between the two sidelobes is considered. Reproduced under the terms of the Creative Commons Attribution 4.0 International License [153]. Copyright 2022, the Authors. b) Calibration curve of the bioassay performed with an LPG working at the DTP for detecting anti-mouse IgG in human serum in concentrations ranging from 1 μg/L to 100 mg/L. Reproduced from [158]. Copyright 2014 Elsevier.

- **Multiparameter sensing**: the differential shift in two or more attenuation bands in an LPG can be used for multiparameter sensing, assuming that the sensitivities to the parameters under study are different for each of the bands. One of the first sensors of this type measured simultaneously strain and temperature [167]. More recent examples of multiparameter sensing with LPGs include [168], where an LPG is inscribed in a Panda fiber (fiber with high refringence due to the stress rods of boron doped glass on opposite sides of the core) and three attenuation bands are utilized for measuring simultaneously the SRI, the temperature and the strain; or [169], where three different LPGs are manufactured in series in a single mode fiber for measuring temperature, relative humidity and volatile organic compounds (VOCs), parameters linked with air quality monitoring. Each LPG is optimized for measuring the corresponding parameter and operating next to the DTP.

  LPGs have also been combined with FBGs for multiparameter sensing. A configuration that was initially used consisted in employing one LPG and two FBGs measured in reflection (the LPG spectrum is not seen in reflection). One of the monitored parameters was the wavelength shift of one of the FBGs while the other was defined by the relationship between the reflectivities of both FBGs, which were affected by the LPG shift with the variables of interest, as in [170] (strain and temperature are measured) or [171] (SRI and temperature are monitored). More recent sensors include other configurations, as in [172], where an LPG and an FBG are superimposed to measure simultaneously SRI and temperature. The sensor works in the mode transition region of the LPG and both wavelength shifts are measured in transmission.

2.3.3. TFBGs

In TFBGs the gratings are angled with respect to the perpendicular to the optical fiber axis, as opposed to FBGs, where the gratings are perpendicular to the optical fiber axis. As a result, in each grating plane part of the light is reflected towards the cladding, contributing to the enhancement of the counter-propagating cladding modes and the corresponding resonances in the transmission spectrum [65].

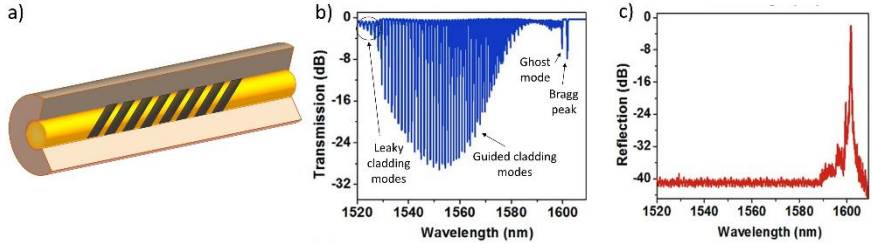

Fig. 2.16 a) Schematic representation of a tilted fiber Bragg grating (TFBG). b) Transmission spectrum of a TFBG. c) Reflection spectrum of a TFBG. b), c) reproduced from [65]. Copyright 2012 by WILEY-VCH Verlag GmbH & Co. KGaA, Weinheim.

In the TFBG transmission spectrum, several resonances can be observed, see **Fig. 2.16b**. In the first place, the Bragg resonance, which is located at the highest wavelength and corresponds, as in the case of the FBG, to the coupling of the core mode to the counter-propagating core mode (therefore its wavelength continues to be calculated with equation (2.4)). The closest resonance to the Bragg wavelength, which is usually deeper than the neighboring resonances, is named "ghost" mode resonance [173], because it has many properties in common with the Bragg resonance but it consists of the superposition of several low order cladding mode resonances. Then, to the left of the ghost mode, there is a spectral comb where each resonance is the result of the coupling between the core mode and a group of counter-propagating cladding modes. There is a discontinuity in the comb that establishes the frontier between the guided cladding modes (effective refractive index higher than the SRI) and the leaky cladding modes (effective refractive index lower than the SRI) [65]. The wavelength at which the coupling occurs for each cladding mode is given by the following equation:

$$\lambda = \left(n_{core}(\lambda) + n^{i}_{cladding}(\lambda)\right) \cdot \frac{\Lambda}{cos\theta} \qquad (2.7)$$

where $n_{core}\ (\lambda)$ is the effective refractive index of the core mode at λ, $n^{i}_{cladding}\ (\lambda)$ is the effective refractive index of the ith cladding mode at λ, Λ is the grating period and θ is the tilt angle. Regarding the reflection spectrum (see **Fig. 2.16c**), only the Bragg resonance is clearly visible. Cladding modes do not usually appear in the reflection spectra because they are highly attenuated by scattering and absorption at the cladding boundary [65].

When $\theta < 45^{o}$, the term weakly tilted FBG (or simply TFBG) is used. When $\theta > 45^{o}$, the term excessively tilted FBGs is employed [63,174]. In the latter case, due to the high tilt angle, there is coupling between the core mode and the co-propagating

cladding modes, so excessively tilted FBGs present a mixed behavior between TFBGs and LPGs. Their spectrum in transmission consists of several cladding mode resonances with a FWHM of a few nanometers spread over a wavelength range of several hundred nanometers.

Returning to the standard TFBG, the Bragg resonance possesses the same temperature and strain sensitivities as the ones mentioned for standard FBGs, while being insensitive to changes outside the cladding. Considering that the cladding mode resonances possess a very similar temperature sensitivity to that of the Bragg resonance [175], the Bragg resonance can be employed to remove the temperature cross sensitivity in most sensing applications by simply subtracting the wavelength shift of the Bragg resonance from the shift of the cladding resonances. Regarding the strain sensitivity, it is not the same for all the cladding resonances, being higher as they are close to the Bragg wavelength [175].

It must be mentioned that although the spectral sensitivity of TFBGs is low in comparison with other technologies such as LPGs, this fact is compensated by the spectral width of the resonances (two orders of magnitude lower than LPGs). As a result, the figure of merit (FOM) of TFBGs, which is the spectral sensitivity divided by the FWHM and is a measure of the resolution of the sensor, is the same as for LPGs [65].

2.3.3.1. Fabrication techniques

Regarding the fabrication techniques, they are the same as the ones previously described in the case of fiber Bragg gratings, although some modifications are required in order to "introduce" the tilt angle [65]. In the case of the interferometric techniques, the change consists in simply tilting the fiber with respect to the fringe pattern, as it can be observed in **Fig. 2. 17a**. Concerning the phase mask technique, there are two options: tilting both the phase mask and the fiber with respect to an axis perpendicular to the writing beam (see **Fig. 2. 17b**) or keeping them perpendicular to the beam and rotating the phase mask around the axis of the incident beam (see **Fig. 2. 17c**). Between these two options, the first one is preferred as it provides very strong and narrow cladding mode resonances.

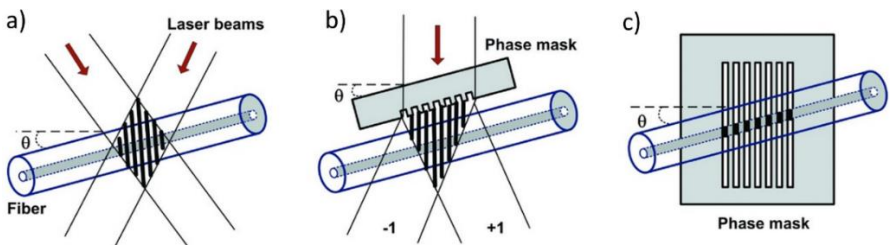

Fig. 2. 17 TFBG fabrication techniques a) Interferometric technique, b) Phase mask technique tilting both the phase mask and the fiber with respect to an axis perpendicular to the writing beam, c) Phase mask technique keeping the phase mask and the fiber perpendicular to the beam and rotating the phase mask around the axis of the incident beam (in this case the incident light is perpendicular to the plane of the page). Reproduced from [65]. Copyright 2012 by WILEY-VCH Verlag GmbH & Co. KGaA, Weinheim.

2.3.3.2. Applications

Apart from the basic magnitudes to which all the fiber gratings are sensitive (temperature and strain [175,176]), TFBGs are very sensitive to bending [177,178], leading to the development of sensors for bending measurement [179], or bending-based, such as an accelerometer [180], or a vector inclinometer [181]. Sensors for measuring the SRI [182–187], as well as biosensors [188–191] (mostly based on the combination of TFBGs with SPRs) have also been manufactured employing TFBGs. Finally, TFBG-based sensors have recently acquired great relevance for monitoring the electrochemical and thermal activity in batteries [192,193].

- **Temperature and strain**: in most cases temperature is not measured as an end in itself, but to eliminate the effect of the temperature drift on the measurement of another parameter. This is usually done by taking into account that the temperature sensitivity of all the resonances is very similar and that temperature only produces a wavelength shift, but not a change in intensity. This way temperature independent sensors for different purposes are manufactured, such as refractive index sensing [194], vibration monitoring [195] or twist detection [196].

  Considering that the wavelength shift associated with strain is different for each resonance and the approximately constant shift with temperature, TFBG based sensors for both strain and temperature can also be developed [175,176]. An example of how to measure the strain is shown in **Fig. 2.18a** [175]. The same approach, but characterizing in detail the temperature and strain sensitivities of the core mode and a cladding mode is applied in [197].

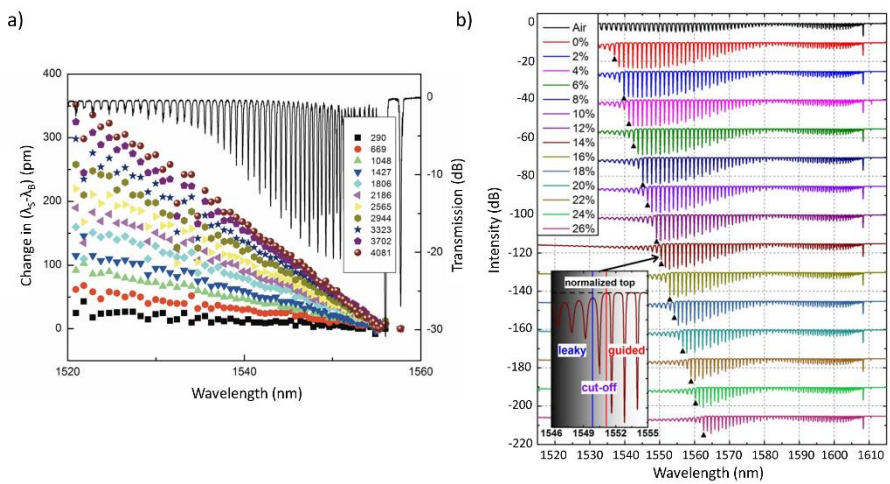

Fig. 2.18 a) Strain dependence of the relative wavelength shifts between the cladding mode resonances and the Bragg peak. Reproduced from [65] (copyright 2012 by WILEY-VCH), adapted from [175] (copyright 2006 The Institution of Engineering and Technology). b) Nonpolarized TFBG spectra in saline solutions with concentration ranging from 0% to 26%. The position of the cutoff mode is marked with a black triangle. Inset: detailed spectrum of the cutoff mode resonance for the concentration of 14%. Reproduced from [185]. Copyright 2015, Optica Publishing Group.

- **Bending**: the Bragg peak is insensitive to bending, while the ghost mode and low order cladding modes are very sensitive to bending [177,178]. The ghost mode is more useful for measuring small curvatures, while higher order modes are more suitable for stronger bends [65]. An example of a sensor of this type is presented in [179], where a directional bend sensor is developed based on a regrown TFBG written in a small core single mode fiber with UV overexposure.

  The bending sensing capability of the TFBGs can be employed to manufacture more complex sensors, such as an accelerometer [180], or a vector inclinometer [181]. In [180], a TFBG is combined with an abrupt biconical taper in an optical fiber, creating a structure that is very sensitive to microbending, see **Fig. 2.19a**. The acceleration can be determined by monitoring the reflected power level, obtaining a sensor with a linear response in the range from 0.5 to 12.5 G, see **Fig. 2.19b**. A similar configuration is employed in [181], where a vector inclinometer is introduced, being capable of measuring both the amplitude and tilt direction of bends on a 2-mm-long flexure joint in an optical fiber.

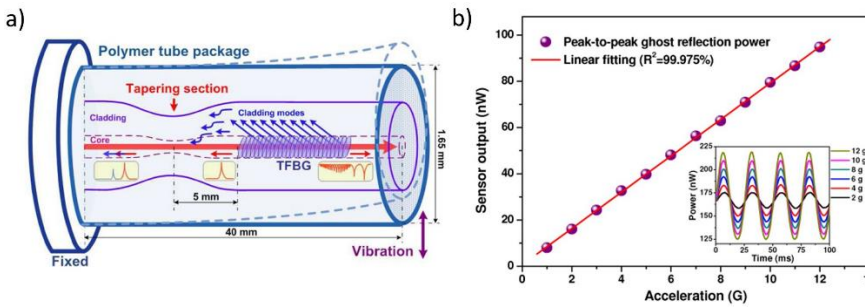

Fig. 2.19 a) Schematic diagram of the abrupt-tapered TFBG accelerometer. b) Linear power response of the sensor vs applied acceleration. Reproduced under an Open Access License [180]. Copyright 2009, Optica Publishing Group.

- **Refractive index**: when the SRI increases, the cladding mode resonances progressively disappear as the modes reach the cut-off point and they become lossy (their effective refractive index is lower than the SRI) [182]. The first methods for measuring the refractive index with TFBGs were based on the area of the envelope of the cladding mode spectrum [182]. Another proposed method was based on measuring the shift of cladding mode resonances as they approached cut-off, where the sensitivity is the highest, achieving values of around 100 nm/RIU [183]. The combination of TFBGs with SPRs by means of metallic coatings can be employed to enhance the sensitivity, as in the case of [184], where a value of 571.5 nm/RIU is achieved in the 1.332 - 1.338 RI range with a gold coating.

  It is also worth mentioning the development of refractometers based on TFBGs that detect absolute values of refractive index, as opposed to standard refractometers that detect variations of the refractive index. In [185], a method based on monitoring the cutoff wavelength (see **Fig. 2.18b**) and contrasting it with theoretical simulations is employed to calculate the refractive index of the solution a device is immersed in, achieving an accuracy of $\pm 10^{-3}$ for the SRI value. This

method is improved in [186] by employing all the resonances of the spectral comb, reaching an accuracy of ± $5 \cdot 10^{-5}$. An even lower limit of detection ($2 \cdot 10^{-5}$) is obtained in [187] by tracking the shift of 27 cladding mode resonances, although in this case the refractometer does not measure absolute values.

- **Biosensing**: most biosensors are based on the combination of TFBGs with SPRs for improving the sensitivity. For instance, in [188] a TFBG is coated with gold to generate a SPR and then additional layers of graphene oxide and staphylococcal protein A (SPA) are added to increase the sensitivity, achieving a LOD of 0.5 µg/mL for human IgG. A gold layer is also employed for generating the SPR in [189], where polydopamine (PDA)-immobilized concanavalin A (Con A) is utilized in the biofunctionalization of the sensor for detecting D-glucose. A limit of detection close to 10^{-7} M was obtained. In [190], a gold coated TFBG is employed to detect HER2 (Human Epidermal Growth Factor Receptor-2) proteins. The main features of this sensor are the employment of an FBG superimposed on the TFBG spectra and a demodulation technique based on the intersection of the upper and lower envelopes of the TFBG spectra.

  The utilization of nanoparticles, as in [191], also provides the possibility of generating a Localized Surface Plasmon Resonance (LSPR) instead of a SPR. In this case, gold nanospheres and gold nanocages enable to reduce the LOD for detecting biotin from 90 nM (without gold nanoparticles) to 11 pM and 8 pM respectively, that is, an improvement of more than three orders of magnitude.

- **Battery monitoring**: in recent years, battery monitoring has experienced important advances thanks to the use of fiber gratings. For instance, in [198] FBGs are employed to measure with high accuracy both the temperature and the pressure, as well as several thermodynamic parameters (enthalpy potential, entropy), in commercial sodium-ion and lithium-ion cells.

  The utilization of TFBGs has increased the number of variables that can be measured in real time. In [192] TFBGs are used to simultaneously monitor the temperature and refractive index inside the batteries, parameters that are linked to the chemical evolution of the electrolyte, and to measure the turbidity of the electrodes. On the other hand, a gold-coated TFBG is employed in [193] to monitor the electrochemical kinetics of aqueous zinc-ion batteries.

2.4. Conclusions

In this chapter, the optical fiber structures employed along the development of this thesis have been analyzed and described in detail, considering their main characteristics, operation, existing types, fabrication techniques and principal applications.

Regarding lossy mode resonances, they stand out because of their sensitivity, which has led to the development of several biosensors. However, several biomarkers have to be simultaneously detected for precisely diagnosing diseases. In this sense, multiparameter sensors based on LMRs on planar waveguides have already been

developed but prior to the development of this thesis, there was no similar structure based on LMRs on an optical fiber. This configuration will be covered in chapter 3.

In the case of optical gratings, different considerations have to be made for FBGs, LPGs and TFBGs. Concerning FBGs, and taking into account their characteristics, it is difficult to develop sensors with a high sensitivity. However, FBGs show a great potential to be combined with other structures for temperature compensation and improvement of their operation. The possibilities of combining FBGs with LMRs to enhance their performance will also be treated in chapter 3.

LPGs seem to have achieved their full potential thanks to the dispersion turning point (DPT) and the mode transition phenomena, which have played a key role in the development of refractometers and biosensors with high sensitivity based on LPGs. Nevertheless, there is still room for improvement, as it will be demonstrated in chapter 4 by studying the mode transition in double clad LPGs and showing that sensitivity can still be increased by employing these type of fibers.

Finally, TFBGs present an enormous potential due to their temperature compensating capability (thanks to the Bragg resonance), narrow linewidth and high figure of merit. The numerous cladding resonances in their transmission spectra also make them attractive for multiparameter sensing. TFBGs have also been combined with SPRs for enhancing their properties, so it was decided to study the deposition of a metallic oxide (material that generates LMRs) on an optical fiber with a TFBG inscribed on it. As a result, the mode transition phenomena has been studied on TFBGs and will be described in chapter 4.

Bibliography

1. *Optical Fiber Sensors: Advanced Techniques and Applications* ; Rajan, G., Ed.; CRC Pres, 2015; ISBN 9781482228250.
2. Lee, B. Review of the Present Status of Optical Fiber Sensors. *Optical Fiber Technology* **2003**, *9*, 57–79, doi:10.1016/S1068-5200(02)00527-8.
3. Urrutia, A.; Del Villar, I.; Zubiate, P.; Zamarreño, C.R. A Comprehensive Review of Optical Fiber Refractometers: Toward a Standard Comparative Criterion. *Laser & Photonics Reviews* **2019**, *13*, 1900094, doi:10.1002/lpor.201900094.
4. Bosch, M.E.; Sánchez, A.J.R.; Rojas, F.S.; Ojeda, C.B. Recent Development in Optical Fiber Biosensors. *Sensors 2007, Vol. 7, Pages 797-859* **2007**, *7*, 797–859, doi:10.3390/S7060797.
5. Leung, A.; Shankar, P.M.; Mutharasan, R. A Review of Fiber-Optic Biosensors. *Sensors and Actuators B: Chemical* **2007**, *125*, 688–703, doi:10.1016/J.SNB.2007.03.010.
6. Joe, H.E.; Yun, H.; Jo, S.H.; Jun, M.B.G.; Min, B.K. A Review on Optical Fiber Sensors for Environmental Monitoring. *International Journal of Precision Engineering and Manufacturing-Green Technology 2018 5:1* **2018**, *5*, 173–191, doi:10.1007/S40684-018-0017-6.
7. Brogan, K.L.; Walt, D.R. Optical Fiber-Based Sensors: Application to Chemical Biology. *Current Opinion in Chemical Biology* **2005**, *9*, 494–500, doi:10.1016/J.CBPA.2005.08.009.
8. Ye, X.W.; Su, Y.H.; Han, J.P. Structural Health Monitoring of Civil Infrastructure Using Optical Fiber Sensing Technology: A Comprehensive Review. *Scientific World Journal* **2014**, *2014*, doi:10.1155/2014/652329.

9. Lee, B.H.; Kim, Y.H.; Park, K.S.; Eom, J.B.; Kim, M.J.; Rho, B.S.; Choi, H.Y. Interferometric Fiber Optic Sensors. *Sensors* 2012, *12*, 2467–2486.

10. Woliński, T.R. Polarimetric Optical Fibers and Sensors. *Progress in Optics* **2000**, *40*, 1–75, doi:10.1016/S0079-6638(00)80029-3.

11. Socorro-Leránoz, A.B.; Santano, D.; Del Villar, I.; Matias, I.R. Trends in the Design of Wavelength-Based Optical Fibre Biosensors (2008–2018). *Biosensors and Bioelectronics: X* 2019, *1*, 100015.

12. Udd, E.; Spillman, W.B. *Fiber Optic Sensors: An Introduction for Engineers and Scientists*; Wiley, 2011; ISBN 9781118014103.

13. Erdogan, T. Fiber Grating Spectra. *Journal of Lightwave Technology* **1997**, *15*, 1277–1294, doi:10.1109/50.618322.

14. Othonos, A.; Kalli, K. *Fiber Bragg Gratings : Fundamentals and Applications in Telecommunications and Sensing*; Artech House: London, UK, 1999; ISBN 9780890063446.

15. Othonos, A. Fiber Bragg Gratings. *Review of Scientific Instruments* **1998**, *68*, 4309, doi:10.1063/1.1148392.

16. Gupta, B.D.; Verma, R.K. Surface Plasmon Resonance-Based Fiber Optic Sensors: Principle, Probe Designs, and Some Applications. *Journal of Sensors* **2009**, *2009*, doi:10.1155/2009/979761.

17. Del Villar, I.; Arregui, F.J.; Zamarreño, C.R.; Corres, J.M.; Bariain, C.; Goicoechea, J.; Elosua, C.; Hernaez, M.; Rivero, P.J.; Socorro, A.B.; et al. Optical Sensors Based on Lossy-Mode Resonances. *Sensors and Actuators B: Chemical* **2017**, *240*, 174–185, doi:10.1016/J.SNB.2016.08.126.

18. Chiavaioli, F.; Janner, D. Fiber Optic Sensing with Lossy Mode Resonances: Applications and Perspectives. *Journal of Lightwave Technology* **2021**, *39*, 3855–3870, doi:10.1109/JLT.2021.3052137.

19. Malitson, I.H. Interspecimen Comparison of the Refractive Index of Fused Silica. *J Opt Soc Am* **1965**, *55*, 1205, doi:10.1364/josa.55.001205.

20. Ciddor, P.E. Refractive Index of Air: New Equations for the Visible and near Infrared. *Applied Optics* **1996**, *35*, 1566, doi:10.1364/AO.35.001566.

21. Corres, J.M.; Del Villar, I.; Arregui, F.J.; Matias, I.R. Analysis of Lossy Mode Resonances on Thin-Film Coated Cladding Removed Plastic Fiber. *Optics Letters* **2015**, *40*, 4867, doi:10.1364/OL.40.004867.

22. Del Villar, I.; Hernaez, M.; Zamarreño, C.R.; Sánchez, P.; Fernández-Valdivielso, C.; Arregui, F.J.; Matias, I.R. Design Rules for Lossy Mode Resonance Based Sensors. *Applied Optics* **2012**, *51*, 4298–4307, doi:10.1364/AO.51.004298.

23. Ozcáriz, A.; Zamarreño, C.R.; Arregui, F.J. A Comprehensive Review: Materials for the Fabrication of Optical Fiber Refractometers Based on Lossy Mode Resonance. *Sensors* **2020**, *20*, 1972, doi:10.3390/s20071972.

24. Homola, J.; Piliarik, M. *Surface Plasmon Resonance (SPR) Sensors*; Springer, 2006;

25. Zamarreño, C.R.; Arregui, F.J.; Del Villar, I.; Matias, I.R.; Hernaez, M. Lossy Mode Resonance Generation With Indium-Tin-Oxide-Coated Optical Fibers for Sensing Applications. *Journal of Lightwave Technology, Vol. 28, Issue 1, pp. 111-117* **2010**, *28*, 111–117.

26. Del Villar, I.; Zamarreño, C.R.; Hernaez, M.; Arregui, F.J.; Matias, I.R. Generation of Lossy Mode Resonances with Absorbing Thin-Films. *Journal of Lightwave Technology* **2010**, *28*, 3351–3357, doi:10.1109/JLT.2010.2082492.

27. Kretschmann, E.; Raether, H. *Radiative Decay of Non Radiative Surface Plasmons Excited by Light*; 1968; Vol. 19;.

28. Del Villar, I.; Beruete, M.; Torres, V. Experimental Demonstration of Lossy Mode and Surface Plasmon Resonance Generation with Kretschmann Configuration. *Optics Letters, Vol. 40, Issue 20, pp. 4739-4742* **2015**, *40*, 4739–4742, doi:10.1364/OL.40.004739.

29. Fuentes, O.; Del Villar, I.; Dominguez, I.; Corres, J.M.; Matías, I.R. Simultaneous Generation of Surface Plasmon and Lossy Mode Resonances in the Same Planar Platform. *Sensors 2022, Vol. 22, Page 1505* **2022**, *22*, 1505, doi:10.3390/S22041505.

30. Del Villar, I.; Zamarreño, C.R.; Hernaez, M.; Arregui, F.J.; Matias, I.R. Lossy Mode Resonance Generation with Indium-Tin-Oxide-Coated Optical Fibers for Sensing Applications. *Journal of Lightwave Technology* **2010**, *28*, 111–117, doi:10.1109/JLT.2009.2036580.

31. Zamarreño, C.R.; Zubiate, P.; Sagües, M.; Matias, I.R.; Arregui, F.J. Experimental Demonstration of Lossy Mode Resonance Generation for Transverse-Magnetic and Transverse-Electric Polarizations. *Optics Letters* **2013**, *38*, 2481, doi:10.1364/ol.38.002481.

32. Zamarreño, C.R.; Matias, I.R.; Arregui, F.J. Nanofabrication Techniques Applied to the Development of Novel Optical Fiber Sensors Based on Nanostructured Coatings. *IEEE Sensors Journal* **2012**, *12*, 2699–2710, doi:10.1109/JSEN.2012.2199750.

33. Singh, J.; Wolfe, D.E. Review Nano and Macro-Structured Component Fabrication by Electron Beam-Physical Vapor Deposition (EB-PVD).

34. Kelly, P.J.; Arnell, R.D. Magnetron Sputtering: A Review of Recent Developments and Applications. *Vacuum* **2000**, *56*, 159–172, doi:10.1016/S0042-207X(99)00189-X.

35. Choy, K.L. Chemical Vapour Deposition of Coatings. *Progress in Materials Science* **2003**, *48*, 57–170, doi:10.1016/S0079-6425(01)00009-3.

36. George, S.M. Atomic Layer Deposition: An Overview. *Chemical Reviews* **2010**, *110*, 111–131, doi:10.1021/cr900056b.

37. Ozcáriz Celaya, A. Materials for the Fabrication of Optical Fiber Refractometers Based on Lossy Mode Resonance, Public University of Navarra, 2020.

38. George, S.M.; Ott, A.W.; Klaus, J.W. Surface Chemistry for Atomic Layer Growth. *Journal of Physical Chemistry* **1996**, *100*, 13121–13131, doi:10.1021/jp9536763.

39. Arregui, F.J.; Del Villar, I.; Zamarreño, C.R.; Zubiate, P.; Matias, I.R. Giant Sensitivity of Optical Fiber Sensors by Means of Lossy Mode Resonance. *Sensors and Actuators, B: Chemical* **2016**, *232*, 660–665, doi:10.1016/j.snb.2016.04.015.

40. Ozcáriz, A.; Zamarreño, C.R.; Zubiate, P.; Arregui, F.J. Is There a Frontier in Sensitivity with Lossy Mode Resonance (LMR) Based Refractometers? *Scientific Reports* **2017**, *7*, 1–7, doi:10.1038/s41598-017-11145-9.

41. Tiwari, D.; Mullaney, K.; Korposh, S.; James, S.W.; Lee, S.W.; Tatam, R.P. An Ammonia Sensor Based on Lossy Mode Resonances on a Tapered Optical Fibre Coated with Porphyrin-Incorporated Titanium Dioxide. *Sensors and Actuators B: Chemical* **2017**, *242*, 645–652, doi:10.1016/J.SNB.2016.11.092.

42. Shanavas, S.; Ahamad, T.; Alshehri, S.M.; Sultan, A.; Acevedo, R.; Anbarasan, P.M. Development of High-Performance Fiber Optic Gas Sensor Based Rice-like CeO2/MWCNT Nanocomposite Synthesized by Facile Hydrothermal Route. *Optics & Laser Technology* **2020**, *123*, 105902, doi:10.1016/J.OPTLASTEC.2019.105902.

43. Usha, S.P.; Mishra, S.K.; Gupta, B.D. Fiber Optic Hydrogen Sulfide Gas Sensors Utilizing ZnO Thin Film/ZnO Nanoparticles: A Comparison of Surface Plasmon Resonance and Lossy Mode Resonance. *Sensors and Actuators B: Chemical* **2015**, *218*, 196–204, doi:10.1016/J.SNB.2015.04.108.

44. Theoderaj, A.K.C.; Inbaraj, D.J.; Mangalaraj, C. CdS Coated Clad-Modified Fiber Optic Sensor for Detection of NO2 Gas. *Materials Research Express* **2019**, *6*, 1050c8, doi:10.1088/2053-1591/AB4236.

45. Vitoria, I.; Zamarreño, C.R.; Ozcáriz, A.; Matias, I.R. Fiber Optic Gas Sensors Based on Lossy Mode Resonances and Sensing Materials Used Therefor: A Comprehensive Review. *Sensors 2021, Vol. 21, Page 731* **2021**, *21*, 731, doi:10.3390/S21030731.

46. Hernaez, M.; Zamarreño, C.R.; Del Villar, I.; Arregui, F.J.; Matias, I.R. Optical Fiber Humidity Sensor Based on Lossy Mode Resonances. *International Journal on Smart Sensing and Intelligent Systems* **2009**, *2*, 653–660, doi:10.21307/IJSSIS-2017-373.

47. Huang, Y.; Zhu, W.; Li, Z.; Chen, G.; Chen, L.; Zhou, J.; Lin, H.; Guan, J.; Fang, W.; Liu, X.; et al. High-Performance Fibre-Optic Humidity Sensor Based on a Side-Polished Fibre Wavelength Selectively Coupled with Graphene Oxide Film. *Sensors and Actuators B: Chemical* **2018**, *255*, 57–69, doi:10.1016/J.SNB.2017.08.042.

48. Bohorquez, D.L.; Del Villar, I.; Corres, J.M.; Matias, I.R. Generation of Lossy Mode Resonances in a Broadband Range with Multilayer Coated Coverslips Optimized for Humidity Sensing. *Sensors and Actuators B: Chemical* **2020**, *325*, 128795, doi:10.1016/J.SNB.2020.128795.

49. Urrutia, A.; Goicoechea, J.; Rivero, P.J.; Pildain, A.; Arregui, F.J. Optical Fiber Sensors Based on Gold Nanorods Embedded in Polymeric Thin Films. *Sensors and Actuators, B: Chemical* **2018**, *255*, 2105–2112, doi:10.1016/J.SNB.2017.09.006.

50. Zamarreño, C.R.; Hernáez, M.; Del Villar, I.; Matías, I.R.; Arregui, F.J. Optical Fiber PH Sensor Based on Lossy-Mode Resonances by Means of Thin Polymeric Coatings. *Sensors and Actuators B: Chemical* **2011**, *155*, 290–297, doi:10.1016/J.SNB.2010.12.037.

51. Socorro, A.B.; Del Villar, I.; Corres, J.M.; Arregui, F.J.; Matias, I.R. Tapered Single-Mode Optical Fiber PH Sensor Based on Lossy Mode Resonances Generated by a Polymeric Thin-Film. *IEEE Sensors Journal* **2012**, *12*, 2598–2603, doi:10.1109/JSEN.2012.2198464.

52. Zubiate, P.; Zamarreño, C.R.; Del Villar, I.; Matias, I.R.; Arregui, F.J. Tunable Optical Fiber PH Sensors Based on TE and TM Lossy Mode Resonances (LMRs). *Sensors and Actuators, B: Chemical* **2016**, *231*, 484–490, doi:10.1016/J.SNB.2016.03.024.

53. Chiavaioli, F.; Zubiate, P.; Del Villar, I.; Zamarreño, C.R.; Giannetti, A.; Tombelli, S.; Trono, C.; Arregui, F.J.; Matias, I.R.; Baldini, F. Femtomolar Detection by Nanocoated Fiber Label-Free Biosensors. *ACS Sensors* **2018**, *3*, 936–943, doi:10.1021/acssensors.7b00918.

54. Zubiate, P.; Urrutia, A.; Zamarreño, C.R.; Egea-Urra, J.; Fernández-Irigoyen, J.; Giannetti, A.; Baldini, F.; Díaz, S.; Matias, I.R.; Arregui, F.J.; et al. Fiber-Based Early Diagnosis of Venous Thromboembolic Disease by Label-Free D-Dimer Detection. **2019**, doi:10.1016/j.biosx.2019.100026.

55. Chiavaioli, F.; Rivero, D.S.; Del Villar, I.; Socorro-Leránoz, A.B.; Zhang, X.; Li, K.; Santamaría, E.; Fernández-Irigoyen, J.; Baldini, F.; Hove, D.L.A. van den; et al. Ultrahigh Sensitive Detection of Tau Protein as Alzheimer's Biomarker via Microfluidics and Nanofunctionalized Optical Fiber Sensors. *Advanced Photonics Research* **2022**, 2200044, doi:10.1002/ADPR.202200044.

56. Moro, G.; Chiavaioli, F.; Liberi, S.; Zubiate, P.; Del Villar, I.; Angelini, A.; de Wael, K.; Baldini, F.; Moretto, L.M.; Giannetti, A. Nanocoated Fiber Label-Free Biosensing for Perfluorooctanoic Acid Detection by Lossy Mode Resonance. *Results in Optics* **2021**, *5*, 100123, doi:10.1016/J.RIO.2021.100123.

57. Zubiate, P.; Ciaurriz, P.; Tellechea, E.; Santano, D.; Del Villar, I.; Urrutia, A.; Arregui, F.J.; Matias, I.R.; Zamarreño, C.R. Short Single Strand DNA Detection by Means of Lossy Mode Resonance Based Fiber-Optic Sensor. In Proceedings of the Proceedings of IEEE Sensors; Institute of Electrical and Electronics Engineers Inc., October 1 2019; Vol. 2019-October.

58. Imas, J.J.; Zamarreño, C.R.; Zubiate, P.; Campión, J.; Sánchez-Martín, L.; Matías, I.R. Rheumatoid Arthritis MiRNA Biomarker Detection by Means of LMR Based Fiber-Optic Biosensor. In Proceedings of the IEEE Sensors 2020; 2020.

59. Dominguez, I.; Del Villar, I.; Fuentes, O.; Corres, J.M.; Matias, I.R. Interdigital Concept in Photonic Sensors Based on an Array of Lossy Mode Resonances. *Scientific Reports 2021 11:1* **2021**, *11*, 1–11, doi:10.1038/s41598-021-92765-0.

60. Fuentes, O.; Corres, J.M.; Dominguez, I.; Del Villar, I.; Matias, I.R. Simultaneous Measurement of Refractive Index and Temperature Using LMR on Planar Waveguide. *Proceedings of IEEE Sensors* **2020**, *2020-October*, doi:10.1109/SENSORS47125.2020.9278727.

61. Dominguez, I.; Corres, J.M.; Fuentes, O.; Del Villar, I.; Matias, I.R. Multichannel Refractometer Based on Lossy Mode Resonances. *IEEE Sensors Journal* **2022**, *22*, 3181–3187, doi:10.1109/JSEN.2022.3142050.

62. Dominguez, I.; Del Villar, I.; Fuentes, O.; Corres, J.M.; Matias, I.R. Dually Nanocoated Planar Waveguides towards Multi-Parameter Sensing. *Scientific Reports 2021 11:1* **2021**, *11*, 1–8, doi:10.1038/s41598-021-83324-8.

63. Guo, T.; González-Vila, Á.; Loyez, M.; Caucheteur, C. Plasmonic Optical Fiber-Grating Immunosensing: A Review. *Sensors 2017, Vol. 17, Page 2732* **2017**, *17*, 2732, doi:10.3390/S17122732.

64. Erdogan, T. Cladding-Mode Resonances in Short- and Long-Period Fiber Grating Filters. *Journal of the Optical Society of America A* **1997**, *14*, 1760, doi:10.1364/josaa.14.001760.

65. Albert, J.; Shao, L.Y.; Caucheteur, C. Tilted Fiber Bragg Grating Sensors. *Laser and Photonics Reviews* 2013, *7*, 83–108.

66. Sipe, J.E.; Erdogan, T. Tilted Fiber Phase Gratings. *JOSA A, Vol. 13, Issue 2, pp. 296-313* **1996**, *13*, 296–313, doi:10.1364/JOSAA.13.000296.

67. Meltz, G.; Morey, W.W.; Glenn, W.H. Formation of Bragg Gratings in Optical Fibers by a Transverse Holographic Method. *Optics Letters* **1989**, *14*, 823, doi:10.1364/OL.14.000823.

68. Hill, K.O.; Meltz, G. Fiber Bragg Grating Technology Fundamentals and Overview. *Journal of Lightwave Technology* **1997**, *15*, 1263–1276, doi:10.1109/50.618320.

69. Hill, K.O.; Malo, B.; Bilodeau, F.; Johnson, D.C.; Albert, J. Bragg Gratings Fabricated in Monomode Photosensitive Optical Fiber by UV Exposure through a Phase Mask. *Applied Physics Letters* **1998**, *62*, 1035, doi:10.1063/1.108786.

70. Hill, K.O.; Malo, B.; Vineberg, K.A.; Bilodeau, F.; Johnson, D.C.; Skinner, I. Efficient Mode Conversion in Telecommunication Fibre Using Externally Written Gratings. *Electronics Letters* **1990**, *26*, 1270–1272, doi:10.1049/EL:19900818.

71. Malo, B.; Hill, K.O.; Bilodeau, F.; Johnson, D.C.; Albert, J. Point-by-Point Fabrication of Micro-Bragg Gratings in Photosensitive Fibre Using Single Excimer Pulse Refractive Index Modification Techniques. *Electronics Letters* **1993**, *29*, 1668–1669, doi:10.1049/EL:19931110.

72. Kashyap, R.; Armitage, J.R.; Wyatt, R.; Davey, S.T.; Williams, D.L. All-Fibre Narrowband Reflection Gratings at 1500nm. *Electronics Letters* **1990**, *26*, 730–732, doi:10.1049/EL:19900476.

73. Limberger, H.G.; Fonjallaz, P.Y.; Salathé, R.P.; Cochet, F. Compaction- and Photoelastic-induced Index Changes in Fiber Bragg Gratings. *Applied Physics Letters* **1998**, *68*, 3069, doi:10.1063/1.116425.

74. Sugden, K.; Mezentsev, V. *Fiber Bragg Gratings: Advances in Fabrication Process and Tools*; Bentham Science Publishers Ltd., 2011; ISBN 9781608053438.

75. He, J.; Xu, B.; Xu, X.; Liao, C.; Wang, Y. Review of Femtosecond-Laser-Inscribed Fiber Bragg Gratings: Fabrication Technologies and Sensing Applications. *Photonic Sensors 2021 11:2* **2021**, *11*, 203–226, doi:10.1007/S13320-021-0629-2.

76. Sahota, J.K.; Gupta, N.; Dhawan, D. Fiber Bragg Grating Sensors for Monitoring of Physical Parameters: A Comprehensive Review. *Optical Engineering* **2020**, *59*, 1, doi:10.1117/1.OE.59.6.060901.

77. Kashyap, R. *Fabrication of Bragg Gratings*; Academic Press, 2010; ISBN 978-0-12-372579-0.

78. Simpson, A.G.; Kalli, K.; Zhang, L.; Zhou, K.; Bennion, I. Type 1A Fibre Bragg Grating Photosensitivity and the Development of Optimum Temperature Invariant Type I-Type IA Strain Sensors. *Optical Sensing* **2004**, *5459*, 118, doi:10.1117/12.545299.

79. Liu, Y.; Williams, J.A.R.; Zhang, L.; Bennion, I. Abnormal Spectral Evolution of Fiber Bragg Gratings in Hydrogenated Fibers. *Optics Letters* **2002**, *27*, 586, doi:10.1364/OL.27.000586.

80. Riant, I.; Haller, F. Study of the Photosensitivity at 193 Nm and Comparison with Photosensitivity at 240 Nm Influence of Fiber Tension: Type IIa Aging. *Journal of Lightwave Technology* **1997**, *15*, 1464–1469, doi:10.1109/50.618378.

81. Canning, J.; Bandyopadhyay, S.; Stevenson, M.; Cook, K. Fiber Bragg Grating Sensor for High Temperature Application. *2008 Joint Conference of the Opto-Electronics and Communications Conference and the Australian Conference On Optical Fibre Technology, OECC/ACOFT 2008* **2008**, doi:10.1109/OECCACOFT.2008.4610456.

82. Ams, M.; Dekker, P.; Gross, S.; Withford, M.J. Fabricating Waveguide Bragg Gratings (WBGs) in Bulk Materials Using Ultrashort Laser Pulses. *Nanophotonics* **2017**, *6*, 743–763, doi:10.1515/NANOPH-2016-0119/ASSET/GRAPHIC/J_NANOPH-2016-0119_FIG_022.JPG.

83. Tosi, D. Review of Chirped Fiber Bragg Grating (CFBG) Fiber-Optic Sensors and Their Applications. *Sensors 2018, Vol. 18, Page 2147* **2018**, *18*, 2147, doi:10.3390/S18072147.

84. Palumbo, G.; Tosi, D.; Iadicicco, A.; Campopiano, S. Analysis and Design of Chirped Fiber Bragg Grating for Temperature Sensing for Possible Biomedical Applications. *IEEE Photonics Journal* **2018**, *10*, doi:10.1109/JPHOT.2018.2829623.

85. Othonos, A. Fiber Bragg Gratings. *Review of Scientific Instruments* **1998**, *68*, 4309, doi:10.1063/1.1148392.

86. Eggleton, B.J.; Krug, P.A.; Poladian, L.; Ouellette, F. Long Periodic Superstructure Bragg Gratings in Optical Fibres. *Electronics Letters* **1994**, *30*, 1620–1622, doi:10.1049/EL:19941088.

87. Chah, K.; Kinet, D.; Caucheteur, C. Negative Axial Strain Sensitivity in Gold-Coated Eccentric Fiber Bragg Gratings. *Scientific Reports 2016 6:1* **2016**, *6*, 1–6, doi:10.1038/srep38042.

88. Jung, J.; Nam, H.; Lee, B. Fiber Bragg Grating Temperature Sensor with Controllable Sensitivity. *Applied Optics, Vol. 38, Issue 13, pp. 2752-2754* **1999**, *38*, 2752–2754, doi:10.1364/AO.38.002752.

89. Hirayama, N.; Sano, Y. Fiber Bragg Grating Temperature Sensor for Practical Use. *ISA Trans* **2000**, *39*, 169–173, doi:10.1016/S0019-0578(00)00012-4.

90. Majumder, M.; Gangopadhyay, T.K.; Chakraborty, A.K.; Dasgupta, K.; Bhattacharya, D.K. Fibre Bragg Gratings in Structural Health Monitoring—Present Status and Applications. *Sensors and Actuators A: Physical* **2008**, *147*, 150–164, doi:10.1016/J.SNA.2008.04.008.

91. Li, K. Review of the Strain Modulation Methods Used in Fiber Bragg Grating Sensors. *Journal of Sensors* **2016**, *2016*, doi:10.1155/2016/1284520.

92. Campanella, C.E.; Cuccovillo, A.; Campanella, C.; Yurt, A.; Passaro, V.M.N. Fibre Bragg Grating Based Strain Sensors: Review of Technology and Applications. *Sensors 2018, Vol. 18, Page 3115* **2018**, *18*, 3115, doi:10.3390/S18093115.

93. Xu, M.G.; Reekie, L.; Chow, Y.T.; Dakin, J.P. Optical In-Fibre Grating High Pressure Sensor. *Electronics Letters* **1993**, *29*, 398–399, doi:10.1049/EL:19930267.

94. Wei, Z.; Song, D.; Zhao, Q.; Cui, H.L. High Pressure Sensor Based on Fiber Bragg Grating and Carbon Fiber Laminated Composite. *IEEE Sensors Journal* **2008**, *8*, 1615–1619, doi:10.1109/JSEN.2008.929070.

95. Liang, M. fu; Fang, X. qiu; Wu, G.; Xue, G. zhe; Li, H. wei A Fiber Bragg Grating Pressure Sensor with Temperature Compensation Based on Diaphragm-Cantilever Structure. *Optik (Stuttg)* **2017**, *145*, 503–512, doi:10.1016/J.IJLEO.2017.08.014.

96. Sheng, H.-J.; Liu, W.-F.; Lin, K.-R.; Bor, S.-S.; Fu, M.-Y.; Morey, W.W.; Meltz, G.; Glenn, W.H.; Kersey, A.D.; Davis, M.A.; et al. High-Sensitivity Temperature-Independent Differential Pressure Sensor Using Fiber Bragg Gratings. *Optics Express, Vol. 16, Issue 20, pp. 16013-16018* **2008**, *16*, 16013–16018, doi:10.1364/OE.16.016013.

97. Chang, H.Y.; Chang, Y.C.; Sheng, H.J.; Fu, M.Y.; Liu, W.F.; Kashyap, R. An Ultra-Sensitive Liquid-Level Indicator Based on an Etched Chirped-Fiber Bragg Grating. *IEEE Photonics Technology Letters* **2016**, *28*, 268–271, doi:10.1109/LPT.2015.2494611.

98. Diáz, C.A.R.; Leal-Junior, A.G.; André, P.S.B.; Da Costa Antunes, P.F.; Pontes, M.J.; Frizera-Neto, A.; Ribeiro, M.R.N. Liquid Level Measurement Based on FBG-Embedded Diaphragms with Temperature Compensation. *IEEE Sensors Journal* **2018**, *18*, 193–200, doi:10.1109/JSEN.2017.2768510.

99. Ameen, O.F.; Younus, M.H.; Aziz, M.S.; Azmi, A.I.; Raja Ibrahim, R.K.; Ghoshal, S.K. Graphene Diaphragm Integrated FBG Sensors for Simultaneous Measurement of Water Level and Temperature. *Sensors and Actuators A: Physical* **2016**, *252*, 225–232, doi:10.1016/J.SNA.2016.10.018.

100. Li, T.; Shi, C.; Ren, H. A Novel Fiber Bragg Grating Displacement Sensor with a Sub-Micrometer Resolution. *IEEE Photonics Technology Letters* **2017**, *29*, 1199–1202, doi:10.1109/LPT.2017.2712602.

101. Asseh, A.; Sandgren, S.; Åhlfeldt, H.; Sahlgren, B.; Stubbe, R. Fiber Optical Bragg Grating Refractometer. *http://dx.doi.org/10.1080/014680398245055* **1998**, *17*, 51–62, doi:10.1080/014680398245055.

102. Iadicicco, A.; Cusano, A.; Cutolo, A.; Bernini, R.; Giordano, M. Thinned Fiber Bragg Gratings as High Sensitivity Refractive Index Sensor. *IEEE Photonics Technology Letters* **2004**, *16*, 1149–1151, doi:10.1109/LPT.2004.824972.

103. Chryssis, A.N.; Lee, S.M.; Lee, S.B.; Saini, S.S.; Dagenais, M. High Sensitivity Evanescent Field Fiber Bragg Grating Sensor. *IEEE Photonics Technology Letters* **2005**, *17*, 1253–1255, doi:10.1109/LPT.2005.846953.

104. Sridevi, S.; Vasu, K.S.; Asokan, S.; Sood, A.K. Sensitive Detection of C-Reactive Protein Using Optical Fiber Bragg Gratings. *Biosensors and Bioelectronics* **2015**, *65*, 251–256, doi:10.1016/j.bios.2014.10.033.

105. Sridevi, S.; Vasu, K.S.; Jayaraman, N.; Asokan, S.; Sood, A.K. Optical Bio-Sensing Devices Based on Etched Fiber Bragg Gratings Coated with Carbon Nanotubes and Graphene Oxide along with a Specific Dendrimer. *Sensors and Actuators, B: Chemical* **2014**, *195*, 150–155, doi:10.1016/J.SNB.2013.12.109.

106. Sridevi, S.; Vasu, K.S.; Sampath, S.; Asokan, S.; Sood, A.K. Optical Detection of Glucose and Glycated Hemoglobin Using Etched Fiber Bragg Gratings Coated with Functionalized Reduced Graphene Oxide. *J Biophotonics* **2016**, *9*, 760–769, doi:10.1002/JBIO.201580156.

107. Schulze, S.; Wehrhold, M.; Hille, C. Femtosecond-Pulsed Laser Written and Etched Fiber Bragg Gratings for Fiber-Optical Biosensing. *Sensors* **2018**, *18*, doi:10.3390/s18092844.

108. Bekmurzayeva, A.; Dukenbayev, K.; Shaimerdenova, M.; Bekniyazov, I.; Ayupova, T.; Sypabekova, M.; Molardi, C.; Tosi, D. Etched Fiber Bragg Grating Biosensor Functionalized with Aptamers for Detection of Thrombin. *Sensors 2018, Vol. 18, Page 4298* **2018**, *18*, 4298, doi:10.3390/S18124298.

109. Mihailov, S.J. Fiber Bragg Grating Sensors for Harsh Environments. *Sensors 2012, Vol. 12, Pages 1898-1918* **2012**, *12*, 1898–1918, doi:10.3390/S120201898.

110. Liao, C.R.; Wang, D.N. Photonic Sensors Review of Femtosecond Laser Fabricated Fiber Bragg Gratings for High Temperature Sensing . *Photonic Sensors* **2013**, *3*, 97–101, doi:10.1007/s13320-012-0060-9.

111. Qiao, X.; Shao, Z.; Bao, W.; Rong, Q. Fiber Bragg Grating Sensors for the Oil Industry. *Sensors 2017, Vol. 17, Page 429* **2017**, *17*, 429, doi:10.3390/S17030429.

112. Busch, M.; Ecke, W.; Latka, I.; Fischer, D.; Willsch, R.; Bartelt, H. Inscription and Characterization of Bragg Gratings in Single-Crystal Sapphire Optical Fibres for High-Temperature Sensor Applications. *Measurement Science and Technology* **2009**, *20*, 115301, doi:10.1088/0957-0233/20/11/115301.

113. Habisreuther, T.; Elsmann, T.; Pan, Z.; Graf, A.; Willsch, R.; Schmidt, M.A. Sapphire Fiber Bragg Gratings for High Temperature and Dynamic Temperature Diagnostics. *Applied Thermal Engineering* **2015**, *91*, 860–865, doi:10.1016/J.APPLTHERMALENG.2015.08.096.

114. Lupi, C.; Felli, F.; Brotzu, A.; Caponera, M.A.; Paolozzi, A. Improving FBG Sensor Sensitivity at Cryogenic Temperature by Metal Coating. *IEEE Sensors Journal* **2008**, *8*, 1299–1304, doi:10.1109/JSEN.2008.926943.

115. Vendittozzi, C.; Felli, F.; Lupi, C. Modeling FBG Sensors Sensitivity from Cryogenic Temperatures to Room Temperature as a Function of Metal Coating Thickness. *Optical Fiber Technology* **2018**, *42*, 84–91, doi:10.1016/J.YOFTE.2018.02.017.

116. Hsu, C.Y.; Chiang, C.C.; Hsieh, T.S.; Hsu, H.C.; Tsai, L.; Hou, C.H. Study of Fiber Bragg Gratings with TiN-Coated for Cryogenic Temperature Measurement. *Optics & Laser Technology* **2021**, *136*, 106768, doi:10.1016/J.OPTLASTEC.2020.106768.

117. Kim, D.; Kim, H.; Song, M.; Sampath, U. Polymer-Coated FBG Sensor for Simultaneous Temperature and Strain Monitoring in Composite Materials under Cryogenic Conditions. *Applied Optics, Vol. 57, Issue 3, pp. 492-497* **2018**, *57*, 492–497, doi:10.1364/AO.57.000492.

118. Farrar, C.R.; Worden, K. An Introduction to Structural Health Monitoring. *Philosophical Transactions of the Royal Society A: Mathematical, Physical and Engineering Sciences* **2007**, *365*, 303–315, doi:10.1098/RSTA.2006.1928.

119. Jewart, C.M.; Wang, Q.; Canning, J.; Grobnic, D.; Mihailov, S.J.; Chen, K.P. Ultrafast Femtosecond-Laser-Induced Fiber Bragg Gratings in Air-Hole Microstructured Fibers for High-Temperature Pressure Sensing. *Optics Letters* **2010**, *35*, 1443, doi:10.1364/OL.35.001443.

120. Chen, T.; Chen, R.; Jewart, C.; Zhang, B.; Cook, K.; Canning, J.; Chen, K.P. Regenerated Gratings in Air-Hole Microstructured Fibers for High-Temperature Pressure Sensing. *Optics Letters* **2011**, *36*, 3542, doi:10.1364/OL.36.003542.

121. Diaz, C.A.R.; Leal-Junior, A.; Marques, C.; Frizera, A.; Pontes, M.J.; Antunes, P.F.C.; Andre, P.S.B.; Ribeiro, M.R.N. Optical Fiber Sensing for Sub-Millimeter Liquid-Level Monitoring: A Review. *IEEE Sensors Journal* **2019**, *19*, 7179–7191, doi:10.1109/JSEN.2019.2915031.

122. Liu, W.; Guo, Y.; Xiong, L.; Kuang, Y. Fiber Bragg Grating Based Displacement Sensors: State of the Art and Trends. *Sensor Review* **2019**, *39*, 87–98, doi:10.1108/SR-06-2017-0116.

123. Chiavaioli, F.; Baldini, F.; Tombelli, S.; Trono, C.; Giannetti, A. Biosensing with Optical Fiber Gratings. *Nanophotonics* 2017, *6*, 663–679.

124. Candiani, A.; Bertucci, A.; Giannetti, S.; Konstantaki, M.; Manicardi, A.; Pissadakis, S.; Cucinotta, A.; Corradini, R.; Selleri, S. Label-Free DNA Biosensor Based on a Peptide Nucleic Acid-Functionalized Microstructured Optical Fiber-Bragg Grating. *https://doi.org/10.1117/1.JBO.18.5.057004* **2013**, *18*, 057004, doi:10.1117/1.JBO.18.5.057004.

125. Bertucci, A.; Manicardi, A.; Candiani, A.; Giannetti, S.; Cucinotta, A.; Spoto, G.; Konstantaki, M.; Pissadakis, S.; Selleri, S.; Corradini, R. Detection of Unamplified Genomic DNA by a PNA-Based Microstructured Optical Fiber (MOF) Bragg-Grating Optofluidic System. *Biosensors and Bioelectronics* **2015**, *63*, 248–254, doi:10.1016/J.BIOS.2014.07.047.

126. Pevec, S.; Donlagic´, D.D.; Donlagic´*, D.D. Multiparameter Fiber-Optic Sensors: A Review. *https://doi.org/10.1117/1.OE.58.7.072009* **2019**, *58*, 072009, doi:10.1117/1.OE.58.7.072009.

127. Chen, Z.; Tang, J.; Fan, R.; Zhong, Y.; Zhang, J.; Li, S. Side Polished Fiber Bragg Grating Sensor for Simultaneous Measurement of Refractive Index and Temperature. *21st International Conference on Optical Fiber Sensors* **2011**, *7753*, 77538K, doi:10.1117/12.885183.

128. Iadicicco, A.; Campopiano, S.; Cutolo, A.; Giordano, M.; Cusano, A. Nonuniform Thinned Fiber Bragg Gratings for Simultaneous Refractive Index and Temperature Measurements. *IEEE Photonics Technology Letters* **2005**, *17*, 1495–1497, doi:10.1109/LPT.2005.848282.

129. James, S.W.; Tatam, R.P. Optical Fibre Long-Period Grating Sensors: Characteristics and Application. *Measurement Science and Technology* **2003**, *14*, doi:10.1088/0957-0233/14/5/201.

130. Shu, X.; Zhu, X.; Jiang, S.; Shi, W.; Huang, D. High Sensitivity of Dual Resonant Peaks of Long-Period Fibre Grating to Surrounding Refractive Index Changes. *Electronics Letters* **1999**, *35*, 1580–1581, doi:10.1049/EL:19991040.

131. Cusano, A.; Iadicicco, A.; Pilla, P.; Contessa, L.; Campopiano, S.; Cutolo, A.; Giordano, M.; Vengsarkar, A.M.; Lemaire, P.J.; Judkins, J.B.; et al. Mode Transition in High Refractive Index Coated Long Period Gratings. *Optics Express, Vol. 14, Issue 1, pp. 19-34* **2006**, *14*, 19–34, doi:10.1364/OPEX.14.000019.

132. Rees, N.D.; James, S.W.; Tatam, R.P.; Ashwell, G.J. Optical Fiber Long-Period Gratings with Langmuir–Blodgett Thin-Film Overlays. *Optics Letters, Vol. 27, Issue 9, pp. 686-688* **2002**, *27*, 686–688, doi:10.1364/OL.27.000686.

133. Del Villar, I.; Achaerandio, M.; Matías, I.R.; Arregui, F.J. Deposition of Overlays by Electrostatic Self-Assembly in Long-Period Fiber Gratings. *Optics Letters, Vol. 30, Issue 7, pp. 720-722* **2005**, *30*, 720–722, doi:10.1364/OL.30.000720.

134. Del Villar, I.; Matías, I.R.; Arregui, F.J.; Lalanne, P. Optimization of Sensitivity in Long Period Fiber Gratings with Overlay Deposition. *Optics Express, Vol. 13, Issue 1, pp. 56-69* **2005**, *13*, 56–69, doi:10.1364/OPEX.13.000056.

135. Cusano, A.; Iadicicco, A.; Pilla, P.; Contessa, L.; Campopiano, S.; Cutolo, A.; Giordano, M. Cladding Mode Reorganization in High-Refractive-Index-Coated Long-Period Gratings: Effects on the Refractive-Index Sensitivity. *Opt Lett* **2005**, *30*, 2536–2538, doi:10.1364/OL.30.002536.

136. Ma, C.; Wang, J.; Yuan, L. Review of Helical Long-Period Fiber Gratings. *Photonics 2021, Vol. 8, Page 193* **2021**, *8*, 193, doi:10.3390/PHOTONICS8060193.

137. Zhao, Y.; Shen, J. chun; Liu, Q.; Zhu, C. liang Optical Fiber Sensor Based on Helical Fibers: A Review. *Measurement: Journal of the International Measurement Confederation* **2022**, *188*, 110400, doi:10.1016/J.MEASUREMENT.2021.110400.

138. Fujimaki, M.; Nishihara, Y.; Ohki, Y.; Brebner, J.L.; Roorda, S. Ion-Implantation-Induced Densification in Silica-Based Glass for Fabrication of Optical Fiber Gratings. *Journal of Applied Physics* **2000**, *88*, 5534, doi:10.1063/1.1315616.

139. Hirao, K.; Nouchi, K.; Watanabe, M.; Kazansky, P.G.; Mitsuyu, T.; Kondo, Y. Fabrication of Long-Period Fiber Gratings by Focused Irradiation of Infrared Femtosecond Laser Pulses. *Optics Letters, Vol. 24, Issue 10, pp. 646-648* **1999**, *24*, 646–648, doi:10.1364/OL.24.000646.

140. Davis, D.D.; Gaylord, T.K.; Glytsis, E.N.; Kosinski, S.G.; Mettler, S.C.; Vengsarkar, A.M. Long-Period Fibre Grating Fabrication with Focused CO2 Laser Pulses. *Electronics Letters* **1998**, *34*, 302–303, doi:10.1049/EL:19980239.

141. Wang, Y. Review of Long Period Fiber Gratings Written by CO2 Laser. *Journal of Applied Physics* **2010**, *108*, 081101, doi:10.1063/1.3493111.

142. Rego, G. Arc-Induced Long Period Fiber Gratings. *Journal of Sensors* **2016**, *2016*, doi:10.1155/2016/3598634.

143. Lin, C.Y.; Wang, L.A. Loss-Tunable Long Period Fibre Grating Made from Etched Corrugation Structure. *Electronics Letters* **1999**, *35*, 1872, doi:10.1049/EL:19991143.

144. Savin, S.; Digonnet, M.J.F.; Kino, G.S.; Shaw, H.J. Tunable Mechanically Induced Long-Period Fiber Gratings. *Optics Letters* **2000**, *25*, 710, doi:10.1364/OL.25.000710.

145. Rao, Y.J.; Wang, Y.P.; Ran, Z.L.; Zhu, T. Novel Fiber-Optic Sensors Based on Long-Period Fiber Gratings Written by High-Frequency CO2 Laser Pulses. *Journal of Lightwave Technology* **2003**, *21*, 1320–1327, doi:10.1109/JLT.2003.810561.

146. Shu, X.; Allsop, T.; Gwandu, B.; Zhang, L.; Bennion, I. High-Temperature Sensitivity of Long-Period Gratings in B-Ge Codoped Fiber. *IEEE Photonics Technology Letters* **2001**, *13*, 818–820, doi:10.1109/68.935814.

147. Wang, Q.; Du, C.; Zhang, J.; Lv, R.; Zhao, Y. Sensitivity-Enhanced Temperature Sensor Based on PDMS-Coated Long Period Fiber Grating. **2016**, doi:10.1016/j.optcom.2016.05.039.

148. Du, C.; Wang, Q.; Zhao, Y.; Li, J. Highly Sensitive Temperature Sensor Based on an Isopropanol-Filled Photonic Crystal Fiber Long Period Grating. *Optical Fiber Technology* **2017**, *34*, 12–15, doi:10.1016/J.YOFTE.2016.11.013.

149. Zhong, X.; Wang, Y.; Qu, J.; Liao, C.; Liu, S.; Tang, J.; Wang, Q.; Zhao, J.; Yang, K.; Li, Z. High-Sensitivity Strain Sensor Based on Inflated Long Period Fiber Grating. *Optics Letters* **2014**, *39*, 5463, doi:10.1364/OL.39.005463.

150. Wang, Y.-P.; Xiao, L.; Wang, D.N.; Jin, W. Highly Sensitive Long-Period Fiber-Grating Strain Sensor with Low Temperature Sensitivity. *Optics Letters* **2006**, *31*, 3414, doi:10.1364/OL.31.003414.

151. Zhu, T.; Rao, Y.J.; Song, Y.; Chiang, K.S.; Liu, M. Highly Sensitive Temperature-Independent Strain Sensor Based on a Long-Period Fiber Grating with a CO2-Laser Engraved Rotary Structure. *IEEE Photonics Technology Letters* **2009**, *21*, 543–545, doi:10.1109/LPT.2009.2014566.

152. Rego, G. A Review of Refractometric Sensors Based on Long Period Fibre Gratings. *The Scientific World Journal* **2013**, *2013*, doi:10.1155/2013/913418.

153. Dey, T.K.; Tombelli, S.; Roy, A.; Biswas, P.; Giannetti, A.; Basumallick, N.; Baldini, F.; Bandyopadhyay, S.; Trono, C. Sensitivity Analysis of Sidelobes of the Lowest Order Cladding Mode of Long Period Fiber Gratings at Turn Around Point. *Sensors 2022, Vol. 22, Page 2965* **2022**, *22*, 2965, doi:10.3390/S22082965.

154. Zou, F.; Liu, Y.; Mou, C.; Zhu, S. Optimization of Refractive Index Sensitivity in Nanofilm-Coated Long-Period Fiber Gratings near the Dispersion Turning Point. *Journal of Lightwave Technology* **2020**, *38*, 889–897, doi:10.1109/JLT.2019.2949373.

155. Śmietana, M.; Koba, M.; Mikulic, P.; Bock, W.J. Towards Refractive Index Sensitivity of Long-Period Gratings at Level of Tens of µm per Refractive Index Unit: Fiber Cladding Etching and Nano-Coating Deposition. *Optics Express, Vol. 24, Issue 11, pp. 11897-11904* **2016**, *24*, 11897–11904, doi:10.1364/OE.24.011897.

156. Esposito, F.; Srivastava, A.; Sansone, L.; Giordano, M.; Campopiano, S.; Iadicicco, A. Label-Free Biosensors Based on Long Period Fiber Gratings: A Review. *IEEE Sensors Journal* **2021**, *21*, 12692–12705, doi:10.1109/JSEN.2020.3025488.

157. Pilla, P.; Sandomenico, A.; Malachovská, V.; Borriello, A.; Giordano, M.; Cutolo, A.; Ruvo, M.; Cusano, A. A Protein-Based Biointerfacing Route toward Label-Free Immunoassays with Long Period Gratings in Transition Mode. *Biosensors and Bioelectronics* **2012**, *31*, 486–491, doi:10.1016/j.bios.2011.11.022.

158. Chiavaioli, F.; Biswas, P.; Trono, C.; Bandyopadhyay, S.; Giannetti, A.; Tombelli, S.; Basumallick, N.; Dasgupta, K.; Baldini, F. Towards Sensitive Label-Free Immunosensing by Means of Turn-around Point Long Period Fiber Gratings. *Biosensors and Bioelectronics* **2014**, *60*, 305–310, doi:10.1016/J.BIOS.2014.04.042.

159. He, Z.; Tian, F.; Zhu, Y.; Lavlinskaia, N.; Du, H. Long-Period Gratings in Photonic Crystal Fiber as an Optofluidic Label-Free Biosensor. *Biosensors and Bioelectronics* **2011**, *26*, 4774–4778, doi:10.1016/j.bios.2011.05.048.

160. Bock, W.J.; Chen, J.; Mikulic, P.; Eftimov, T. A Novel Fiber-Optic Tapered Long-Period Grating Sensor for Pressure Monitoring. *IEEE Transactions on Instrumentation and Measurement* **2007**, *56*, 1176–1180, doi:10.1109/TIM.2007.899904.

161. Khaliq, S.; James, S.W.; Tatam, R.P. Fiber-Optic Liquid-Level Sensor Using a Long-Period Grating. *Optics Letters* **2001**, *26*, 1224, doi:10.1364/OL.26.001224.

162. Qi, L.; Zhao, C.-L.; Wang, Y.; Kang, J.; Zhang, Z.; Jin, S.; Ng, J.H.; Zhou, X.; Yang, X.; Hao, J. Compact Micro-Displacement Sensor with High Sensitivity Based on a Long-Period Fiber Grating with an Air-Cavity. **2013**.

163. Bhatia, V. Applications of Long-Period Gratings to Single and Multi-Parameter Sensing. *Optics Express* **1999**, *4*, 457, doi:10.1364/OE.4.000457.

164. Liu, Y.; Zhang, L.; Bennion, I. Fibre Optic Load Sensors with High Transverse Strain Sensitivity Based on Long-Period Gratings in B/Ge Co-Doped Fibre. *Electronics Letters* **1999**, *35*, 661–663, doi:10.1049/EL:19990457.

165. Lin, C.Y.; Wang, L.A.; Chern, G.W. Corrugated Long-Period Fiber Gratings as Strain, Torsion, and Bending Sensors. *Journal of Lightwave Technology* **2001**, *19*, 1159–1168, doi:10.1109/50.939797.

166. Wang, Y.P.; Rao, Y.J. Long Period Fibre Grating Torsion Sensor Measuring Twist Rate and Determining Twist Direction Simultaneously. *Electronics Letters* **2004**, *40*, 164–166, doi:10.1049/EL:20040117.

167. Bhatia, V.; Campbell, D.; Claus, R.O.; Vengsarkar, A.M. Simultaneous Strain and Temperature Measurement with Long-Period Gratings. *Optics Letters* **1997**, *22*, 648, doi:10.1364/OL.22.000648.

168. Esposito, F.; Srivastava, A.; Iadicicco, A.; Campopiano, S. Multi-Parameter Sensor Based on Single Long Period Grating in Panda Fiber for the Simultaneous Measurement of SRI, Temperature and Strain. *Optics & Laser Technology* **2019**, *113*, 198–203, doi:10.1016/J.OPTLASTEC.2018.12.022.

169. Hromadka, J.; Korposh, S.; Partridge, M.C.; James, S.W.; Davis, F.; Crump, D.; Tatam, R.P. Multi-Parameter Measurements Using Optical Fibre Long Period Gratings for Indoor Air Quality Monitoring. *Sensors and Actuators, B: Chemical* **2017**, *244*, 217–225, doi:10.1016/j.snb.2016.12.050.

170. Patrick, H.J.; Williams, G.M.; Kersey, A.D.; Pedrazzani, J.R.; Vengsarkar, A.M. Hybrid Fiber Bragg Grating/Long Period Fiber Grating Sensor for Strain/Temperature Discrimination. *IEEE Photonics Technology Letters* **1996**, *8*, 1223–1225, doi:10.1109/68.531843.

171. Jesus, C.; Caldas, P.; Frazão, O.; Santos, J.L.; Jorge, P.A.S.; Baptista, J.M. Simultaneous Measurement of Refractive Index and Temperature Using a Hybrid Fiber Bragg Grating/Long-Period Fiber Grating Configuration. *Fiber and Integrated Optics* **2009**, *28*, 440–449, doi:10.1080/01468030903290039.

172. Pang, B.; Gu, Z.; Ling, Q.; Wu, W.; Zhou, Y. Simultaneous Measurement of Temperature and Surrounding Refractive Index by Superimposed Coated Long Period Fiber Grating and Fiber Bragg Grating Sensor Based on Mode Barrier Region. *Optik (Stuttg)* **2020**, *220*, 165136, doi:10.1016/J.IJLEO.2020.165136.

173. Hewlett, S.J.; Love, J.D.; Meltz, G.; Bailey, T.J.; Morey, W.W. Cladding-Mode Coupling Characteristics of Bragg Gratings in Depressed-Cladding Fibre. *Electronics Letters* **1995**, *31*, 820–822, doi:10.1049/EL:19950533.

174. Wang, C.; Yin, G.; Wang, H.; Zhou, K.; Zhang, L.; Zhao, W.; Wang, Y.; Yan, Z.; Sun, Z. Theoretical and Experimental Analysis of Excessively Tilted Fiber Gratings. *Optics Express, Vol. 24, Issue 11, pp. 12107-12115* **2016**, *24*, 12107–12115, doi:10.1364/OE.24.012107.

175. Chen, C.; Albert, J. Strain-Optic Coefficients of Individual Cladding Modes of Singlemode Fibre: Theory and Experiment. *Electronics Letters* **2006**, *42*, 1027–1028, doi:10.1049/EL:20061631.

176. Caucheteur, C.; Chen, C.; Albert, J.; Mégret, P. Use of Weakly Titled Fiber Bragg Gratings for Strain Sensing Purposes. In Proceedings of the IEEE/LEOS Benelux; IEEE/LEOS Benelux Chapter: Eindhoven, The Netherlands, 2006; Vol. 11.

177. Guo, T.; Liu, F.; Guan, B.O.; Albert, J. Tilted Fiber Grating Mechanical and Biochemical Sensors. *Optics & Laser Technology* **2016**, *78*, 19–33, doi:10.1016/J.OPTLASTEC.2015.10.007.

178. Albert, J. Tilted Fiber Bragg Gratings as Multi-Sensors. *Optics and Photonics News* **2011**, *22*, 28, doi:10.1364/OPN.22.10.000028.

179. Shao, L.Y.; Xiong, L.; Chen, C.; Laronche, A.; Albert, J. Directional Bend Sensor Based on Re-Grown Tilted Fiber Bragg Grating. *Journal of Lightwave Technology* **2010**, *28*, 2681–2687, doi:10.1109/JLT.2010.2064158.

180. Guo, T.; Shao, L.; Tam, H.-Y.; Krug, P.A.; Albert, J.; Gerges, A.S.; Newson, T.P.; C Jones, J.D.; Jackson, D.A.; Wang, Y.J.; et al. Tilted Fiber Grating Accelerometer Incorporating an Abrupt Biconical Taper for Cladding to Core Recoupling. *Optics Express, Vol. 17, Issue 23, pp. 20651-20660* **2009**, *17*, 20651–20660, doi:10.1364/OE.17.020651.

181. Albert, J.; Shao, L.-Y. Compact Fiber-Optic Vector Inclinometer. *Optics Letters, Vol. 35, Issue 7, pp. 1034-1036* **2010**, *35*, 1034–1036, doi:10.1364/OL.35.001034.

182. Laffont, G.; Ferdinand, P. Tilted Short-Period Fibre-Bragg-Grating-Induced Coupling to Cladding Modes for Accurate Refractometry. *Measurement Science and Technology* **2001**, *12*, 765–770, doi:10.1088/0957-0233/12/7/302.

183. Chan, C.F.; Chen, G.; Jafari, A.; Laronche, A.; Thomson, D.J.; Albert, J. Optical Fiber Refractometer Using Narrowband Cladding-Mode Resonance Shifts. *Applied Optics, Vol. 46, Issue 7, pp. 1142-1149* **2007**, *46*, 1142–1149, doi:10.1364/AO.46.001142.

184. Shao, L.-Y.; Shevchenko, Y.; Albert, J. Intrinsic Temperature Sensitivity of Tilted Fiber Bragg Grating Based Surface Plasmon Resonance Sensors. *Optics Express* **2010**, *18*, 11464, doi:10.1364/oe.18.011464.

185. Mandia, D.J.; Albert, J.; Barry, S.T.; Zhou, W. Absolute Near-Infrared Refractometry with a Calibrated Tilted Fiber Bragg Grating. *Optics Letters, Vol. 40, Issue 8, pp. 1713-1716* **2015**, *40*, 1713–1716, doi:10.1364/OL.40.001713.

186. Zhou, W.; Zhou, Y.; Albert, J. A True Fiber Optic Refractometer. *Laser & Photonics Reviews* **2017**, *11*, 1600157, doi:10.1002/LPOR.201600157.

187. Kelly-Richard, A.; Albert, J. Multiresonant Analysis Improves the Limit of Detection of Tilted Fiber Bragg Grating Refractometers. *Optics Letters, Vol. 47, Issue 15, pp. 3740-3743* **2022**, *47*, 3740–3743, doi:10.1364/OL.462687.

188. Wang, Q.; Jing, J.Y.; Wang, B.T. Highly Sensitive SPR Biosensor Based on Graphene Oxide and Staphylococcal Protein A Co-Modified TFBG for Human IgG Detection. *IEEE Transactions on Instrumentation and Measurement* **2018**, doi:10.1109/TIM.2018.2875961.

189. Lobry, M.; Lahem, D.; Loyez, M.; Debliquy, M.; Chah, K.; David, M.; Caucheteur, C. Non-Enzymatic D-Glucose Plasmonic Optical Fiber Grating Biosensor. *Biosensors and Bioelectronics* **2019**, *142*, 111506, doi:10.1016/J.BIOS.2019.111506.

190. Lobry, M.; Fasseaux, H.; Loyez, M.; Chah, K.; Goormaghtigh, E.; Wattiez, R.; Chiavaioli, F.; Caucheteur, C. Plasmonic Fiber Grating Biosensors Demodulated through Spectral Envelopes Intersection. *Journal of Lightwave Technology* **2021**, *39*, 7288–7295, doi:10.1109/JLT.2021.3112854.

191. Lepinay, S.; Staff, A.; Ianoul, A.; Albert, J. Improved Detection Limits of Protein Optical Fiber Biosensors Coated with Gold Nanoparticles. *Biosens Bioelectron* **2014**, *52*, 337–344, doi:10.1016/J.BIOS.2013.08.058.

192. Huang, J.; Han, X.; Liu, F.; Gervillié, C.; Blanquer, L.A.; Guo, T.; Tarascon, J.M. Monitoring Battery Electrolyte Chemistry via In-Operando Tilted Fiber Bragg Grating Sensors. *Energy & Environmental Science* **2021**, *14*, 6464–6475, doi:10.1039/D1EE02186A.

193. Wang, R.; Zhang, H.; Liu, Q.; Liu, F.; Han, X.; Liu, X.; Li, K.; Xiao, G.; Albert, J.; Lu, X.; et al. Operando Monitoring of Ion Activities in Aqueous Batteries with Plasmonic Fiber-Optic Sensors. *Nature Communications 2022 13:1* **2022**, *13*, 1–11, doi:10.1038/s41467-022-28267-y.

194. Jiang, B.; Zhou, K.; Wang, C.; Zhao, Y.; Zhao, J.; Zhang, L.; Chen, W.; Saunders, J.E.; Barnes, J.A.; H Yam, S.S.; et al. Temperature-Calibrated High-Precision Refractometer Using a Tilted Fiber Bragg Grating. *Mater. Express* **2012**, *2*, 1588–1611, doi:10.1364/OE.25.025910.

195. Guo, T.; Ivanov, A.; Chen, C.; Albert, J. Temperature-Independent Tilted Fiber Grating Vibration Sensor Based on Cladding-Core Recoupling. *Optics Letters* **2008**, *33*, 1004, doi:10.1364/OL.33.001004.

196. Lu, Y.; Shen, C.; Chen, D.; Chu, J.; Wang, Q.; Dong, X. Highly Sensitive Twist Sensor Based on Tilted Fiber Bragg Grating of Polarization-Dependent Properties. *Optical Fiber Technology* **2014**, *20*, 491–494, doi:10.1016/J.YOFTE.2014.05.011.

197. Rahimi, S.; Ban, D.; Xiao, G.; Zhang, Z.; Albert, J. Temperature and Strain Sensors Based on Integration of Tilted Fiber Bragg Gratings With a Free Spectral Range Matched Interrogation System. *IEEE Sensors Journal* **2009**, *9*, 858–861, doi:10.1109/JSEN.2009.2024710.

198. Huang, J.; Albero Blanquer, L.; Bonefacino, J.; Logan, E.R.; Alves Dalla Corte, D.; Delacourt, C.; Gallant, B.M.; Boles, S.T.; Dahn, J.R.; Tam, H.Y.; et al. Operando Decoding of Chemical and Thermal Events in Commercial Na(Li)-Ion Cells via Optical Sensors. *Nature Energy 2020 5:9* **2020**, *5*, 674–683, doi:10.1038/s41560-020-0665-y.

Chapter 3

Optimization of Optical Structures Based on LMRs for Multisensing Purposes

3.1. Introduction

Lossy mode resonance (LMR) based sensors have multiple applications including refractive index sensing [1], gas detection [2], humidity sensing [3], pH sensing [4] or biosensing [5]. However, most of the sensors employed in these applications can measure only one parameter or variable. Only with the recent utilization of planar waveguides for developing LMR based sensors, the possibility of measuring two variables simultaneously with this type of sensors has become a reality. Several thin films can be deposited to generate independent resonances, as demonstrated in [6], each of which can be used for sensing a different parameter. The thicknesses of the different thin films have to be controlled in order to avoid the overlap of the corresponding resonances in the spectrum.

For instance, in [7] a LMR sensor for measuring simultaneously refractive index and temperature based on a coverslip is presented. The coverslip is coated with a CuO thin film and then partially coated with polydimethylsiloxane (PDMS), generating two resonances in the spectrum, each of them sensitive to one of the parameters of interest. A similar approach is employed in [8] where two independent thin films are deposited on the same coverslip to develop a multichannel refractometer. The shift of each LMR is separately controlled through its own microfluidic system, while the optical part of the setup is common. This way, the refractive indices of two different liquids were independently and simultaneously measured. A variant of this configuration was introduced in [9], where the thin films are deposited on both sides of the coverslip. Both faces are deposited with CuO and the upper face is coated with PDMS while the lower face is coated with agarose in order to make the resonances sensitive to temperature and humidity, respectively; variables that can be simultaneously measured.

In this sense, the purpose of this chapter is to find and study different structures and configurations based on LMRs that enable measuring more than one variable at the same time apart from the ones that had been previously mentioned.

As LMRs are generated with the deposition of a thin film of a metallic oxide or a polymer on a waveguide [10], such as an optical fiber or a coverslip, the first possibility that it was decided to explore was introducing a grating pattern on the thin film. It was expected that the thin film would continue generating the LMR in the transmission spectrum while the grating pattern would produce bands in the reflection spectrum, being the first time that these two phenomena are studied together. Having different effects in the same device could be employed for multisensing purposes. This way, several thin film grating patterns are analyzed in this chapter for two types of substrate: a coverslip (planar waveguide) and a D-shaped optical fiber. In the first place, the use of a pure grating pattern is assessed, being more focused in the case of

the D-shaped optical fiber, whose parameters (neck, thin film thickness, length) are optimized in order to improve the power, the sensitivity to the surrounding medium refractive index (SRI), and the figure of merit (FOM) of the reflection bands. Then, the combination of a section of constant thickness and a grating section on the thin film pattern is also studied, being capable of generating both an LMR in the transmission spectrum and reflection bands.

On the other hand, an important number of optical fiber refractometers based on LMRs and employing different materials such as ITO [11], SnO_2 [11,12] or TiO_2 [13], have been developed, but none of them includes a temperature compensation mechanism, being temperature a parameter that deeply impacts the measurement of the refractive index [14].

Gratings are a common choice for measuring the temperature and compensating its effect when evaluating the SRI. For example, a hybrid fiber grating configuration combining a long period fiber grating (LPG) and a fiber Bragg grating (FBG) in series is utilized in [15]. The LPG is used to monitor the SRI change while the FBG enables to measure the temperature. There are also FBG-based sensors for multi-parameter sensing, as in [16], where temperature and SRI are measured with a point by point FBG; or [17], in which a highly localized FBG (also known as eccentric FBG) is employed for measuring these two variables and the liquid level. Tilted fiber Bragg gratings (TFBGs) are also used in hybrid configurations for measuring both the SRI and the temperature. For example, in [18], where a LPG is employed for measuring the temperature while the TFBG enables to monitor the SRI, or in [19], in which a surface plasmon resonance (SPR) is combined with a TFBG for measuring the SRI while compensating the temperature. It is also common the use of TFBGs on its own to develop refractometers with temperature compensation, as in [20] (based on measuring the shift of the cladding modes) or in [21] (absolute refractometer that tracks the cutoff cladding mode). However, in the previous TFBG refractometers the temperature drift is compensated but the temperature is not directly measured.

Among the different gratings available (FBGs, LPGs, TFBGs), FBGs seem the simplest and most adequate option for compensating the temperature drift when measuring the SRI. FBGs are insensitive to SRI, since light coupling occurs between core modes and the core is separated from the external medium by the fiber cladding [22]. Therefore, the development of an LMR-based refractometer on a D-shaped optical fiber with temperature compensation by means of an FBG inscribed on its core is explored here for the first time in order to obtain a sensor capable of measuring simultaneously the SRI and the temperature.

The last part of this chapter describes for the first time the procedure to obtain several resonances in a D-shaped optical fiber and shows experimentally two different resonances within the same D-shaped optical fiber with independent resonance wavelength shift as a function of the SRI. In order to achieve this, a nanostructure with different thicknesses must be used. This strategy, previously tested with planar waveguides [6], was adopted for D-shaped optical fiber. The employment of different coating thicknesses takes advantage of the property of LMRs to progressively redshift the resonance position in the spectrum when increasing the thin film thickness [23].

3.2. Analysis on the combination of LMRs and Bragg gratings on thin films

3.2.1. Theory and methods

In this section, two different optical structures (coverslip and D-shaped single mode optical fiber) with different thin film patterns deposited on them are theoretically analyzed with the purpose of optimizing their parameters and determining which of them can be implemented. Four structures are studied:

1. Coverslip with a grating pattern on a thin film (see **Fig. 3.1a**)
2. Coverslip with a thin film with a section of constant thickness and a section with a grating pattern (see **Fig. 3.1b**)
3. D-shaped fiber with a grating pattern on a thin film (see **Fig. 3.1d**)
4. D-shaped fiber with a thin film with a section of constant thickness and a section with a grating pattern (see **Fig. 3.1e**)

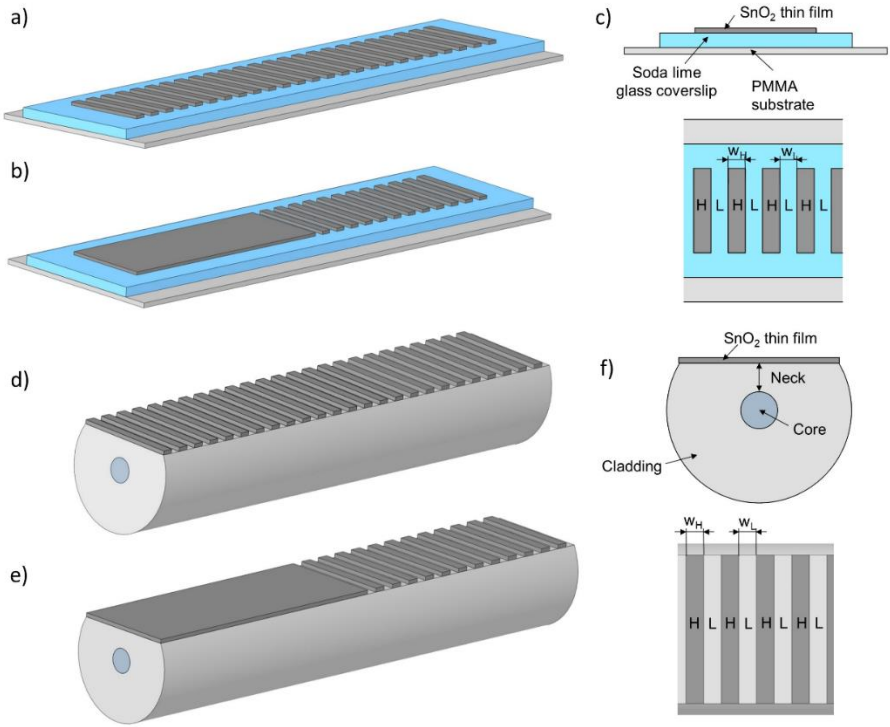

Fig. 3.1 a) 3D schematic diagram of a coverslip with a grating pattern on a thin film. b) Same as a) for a coverslip with a thin film with a section of constant thickness and a section with a grating pattern. c) Section of the coverslip and top view of the Bragg gratings. d) Same as a) but with an optical fiber as substrate instead of a coverslip. e) Same as b) but with an optical fiber as substrate instead of a coverslip. f) Section of the optical fiber and top view of the Bragg gratings. Dimensions not to scale. d,f) Reproduced under the terms of the CC BY 4.0 International License [24]. Copyright 2021, the Authors. Licensee MDPI, Basel, Switzerland.

In **Fig. 3.1c** and **Fig. 3.1f**, a close up of the section and a top view of the Bragg gratings are shown for the coverslip and optical fiber structures respectively. In **Fig. 3.1f**, in the case of the D-shaped optical fiber, the 'neck' is defined as the cladding thickness between the core and the flat surface of the D-shaped fiber, and is the term that will be used from here on.

The idea is to generate both an LMR and reflection bands with these structures to obtain multisensing platforms where several parameters can be measured at the same time. The material employed for the films is SnO_2, which fulfils the conditions for generating LMRs [10,25]. The gratings patterned on the thin films are known as Bragg gratings [26,27] (other names are also used such as Bragg stacks [28], multilayer stacks [29,30], or micrograting [31]) and they produce bands in the reflection spectrum whose central wavelength is given by the Bragg-Snell equation for normal incidence [28]:

$$m\lambda = 2\left(n_{effH}w_H + n_{effL}w_L\right) \tag{3.1}$$

where m is the diffraction order and n_{effH}, n_{effL}, w_H and w_L are the effective refractive indices and widths of the sections with the high- (H) and low- (L) refractive index materials respectively (see again **Fig. 3.1c** and **Fig. 3.1f**). In the performed analysis, it has been always used a 50% duty cycle (only half of each pitch is covered by the thin film), that is, $w_H = w_L$.

In the structures under study, n_{effH} and n_{effL} correspond to the effective refractive index of the sections with and without thin film, respectively. Nevertheless, the SnO_2 thin film does not appreciably affect the effective refractive index of the corresponding section. Therefore, it can be considered that $n_{effH} = n_{effL} = n_{eff}$, where n_{eff} is the effective refractive index of the structure (which is different for the optical fiber and the coverslip). If it is taken into account that the addition of w_H and w_L is equal to the pitch of the grating (Λ), then (1) can be simplified in our case to:

$$m\lambda = 2 \cdot n_{eff} \cdot \Lambda \tag{3.2}$$

The structures studied in this work were analyzed with the commercial software FIMMWAVE® (Photon Design Inc.). The propagation was calculated with FIMMPROP®, a module integrated with FIMMWAVE®. For Bragg grating sections, the finite difference method (FDM) with the Rigorous Coupled Mode Theory (RCMT) algorithm was employed because it enables efficient modeling of gratings. In most cases, a uniform mesh with 100 elements was employed in the X direction (horizontal axis in **Fig. 3.2**) while a non-uniform mesh of around 500 elements was utilized in the Y direction (vertical axis in **Fig. 3.2**). The non-uniform mesh is used in the Y direction because the SnO_2 thin film is much thinner (between 25 and 160 nm depending on the case) than the rest of the layers (from several μm to more than 100 μm) in both structures (optical fiber and coverslip).

The sections that are employed in FIMMWAVE® for modeling the coverslip and the D-shaped fiber are shown in **Fig. 3.2a** and **Fig. 3.2b** respectively. The mesh is not shown, as it would prevent us from distinguishing the shapes. In the case of the D-

shaped fiber, as it was demonstrated in [11], the results calculated with the employed section are equivalent to the ones obtained with the whole D-shaped section, but in this case computational time was saved. With respect to the boundary conditions, no perfectly matched layers (PML) were employed. In the case of the D-shaped fiber, electric walls were placed at the left and right boundary conditions and magnetic walls were used at the top and bottom boundary conditions; while for the coverslip, electric walls were utilized in all the boundaries.

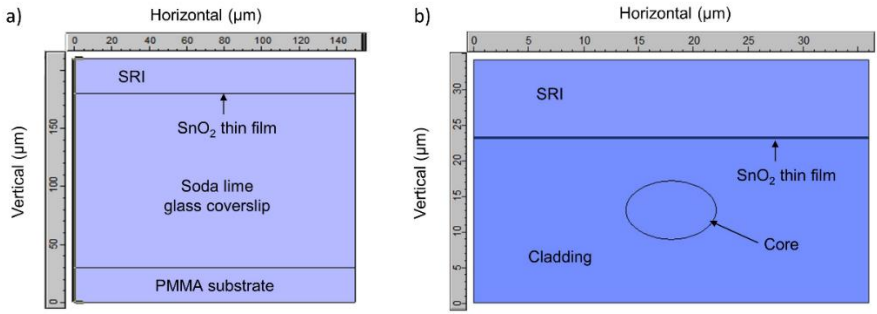

Fig. 3.2 a) Coverslip section as modeled in FIMMWAVE®. b) D-shaped fiber section as modeled in FIMMWAVE®. Please note that different scales are employed for each axis. b) Reproduced under the terms of the CC BY 4.0 International License [24]. Copyright 2021, the Authors. Licensee MDPI, Basel, Switzerland.

Regarding the materials, for the SnO_2 thin film, a refractive index of 1.9 + 0.01i was used based on ellipsometric measurements in [5]. In the case of the optical fiber, the model for SiO_2 was obtained from [32]. With respect to the coverslip, since the simulations are performed under the assumption that the coverslip is made of soda lime glass, the refractive index model was taken from [33]. The coverslip is placed on a poly(methyl methacrylate) (PMMA) substrate whose model is obtained from [34].

A schematic diagram of the setup that would be used for interrogating the structures under study is depicted in **Fig. 3.3**, although variations would have to be introduced in the setup depending on the particular structure under consideration. In the first place, it has to be taken into account that multimode fibers would be used in the setup for the coverslip case while single mode fibers would be employed for the D-shaped fiber case. In the measuring setup, a broadband light source (halogen for the coverslip and SLD for the D-shaped fiber) would be connected to input 1 of an optical circulator. Concerning light polarization, a linear polarizer (not shown) would be placed between the output of the optical fiber that couples the light into the coverslip and the coverslip itself [9]. Regarding the D-shaped fiber, a linear polarizer and a polarization controller, which enables selecting the TE- or TM-polarized state of light [5]; would be employed between the light source and input 1 of the optical circulator (they are not shown). One end of the device under study would be connected to output 2 of the optical circulator and the other end (if the transmitted power has to be monitored) would be connected to a spectrometer (coverslip) or an optical spectrum analyzer, OSA (D-shaped fiber). Output 3 of the optical circulator would be

connected to another spectrometer (coverslip) or OSA (D-shaped fiber) in order to measure the reflected power.

The values used for the parameters of each structure will be described in their corresponding results subsection. However, in all cases the grating pitch Λ is in the order of the μm. This way, the structures under study could be then implemented by means of a mask-assisted photolithography manufacturing process using an ultraviolet laser writer with a resolution below the μm, which is thought to be repetitive enough for this step. Once the mask has been fabricated, the rest of the process would consist of depositing the SnO_2 thin film by sputtering [11] or atomic layer deposition [35], and finally removing the mask to obtain the desired pattern on the deposited thin film.

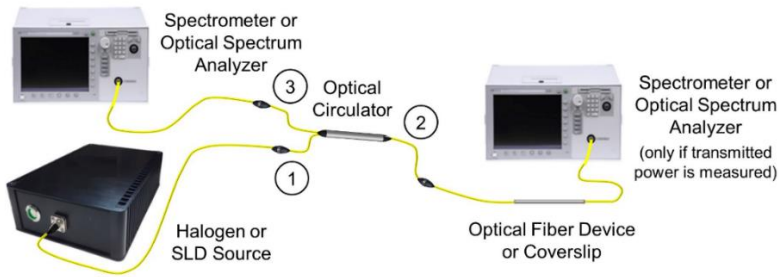

Fig. 3.3. Schematic diagram of the setup that would be employed for interrogating the devices under analysis. The elements required for light polarization are not shown.

3.2.2. Results

3.2.2.1. Coverslip (grating pattern)

In the first place, it was decided to check if the coverslip with a thin film having a grating pattern was able to generate an LMR, see **Fig. 3.1a**. In order to test it, a total grating length of 20 mm with different grating pitches (4 μm, 8 μm, 10 μm, 50 μm, 80 μm, 100 μm, 500 μm, 800 μm, 20,000 μm) and therefore a different number of periods (from 500 periods in the case of the 4 μm pitch down to 1 period for the 20,000 μm pitch) was simulated. The SnO_2 thin film has a thickness of 160 nm (this thickness has been selected so the LMR is centered in the studied window, 1200 - 1800 nm). Transverse electric (TE) polarized light is employed and the surrounding medium is air (SRI equal to 1). It has been decided to use TE polarization as it gave better results than TM (transverse magnetic) polarization in the case of the D-shaped optical fiber (see subsection 3.2.2.3) and similar results are expected here. The transmitted power for each value of the grating pitch is shown in **Fig. 3.4**. In all the cases, the transmission spectrum has been obtained after subtracting the transmitted power corresponding to the blank device (coverslip with a length of 20 mm and no thin film). The reflection bands for some cases are shown in **Fig. 3.5a** (pitch of 4 μm, 8 μm, and 10 μm) and **Fig. 3.5b** (pitch of 50 μm, 500 μm, and 20,000 μm)

Regarding the results in transmission, it can be seen in **Fig. 3.4** that with the lowest pitch values that have been tested (4 μm, 8 μm, and 10 μm), it is not possible to

generate an LMR. If the grating pitch is increased by one order of magnitude (50 µm, 80 µm, and 100 µm cases), it seems that some kind of LMR effect starts to appear, but it still is not very clear. It is required to increase the pitch another order of magnitude (500 µm, 800 µm) to clearly see the generation of an LMR. If the grating pitch is further increased (20,000 µm; which corresponds to only one period and can be hardly considered a grating), the LMR gains in definition and it can be observed that it has shifted to the red in comparison with the previous cases.

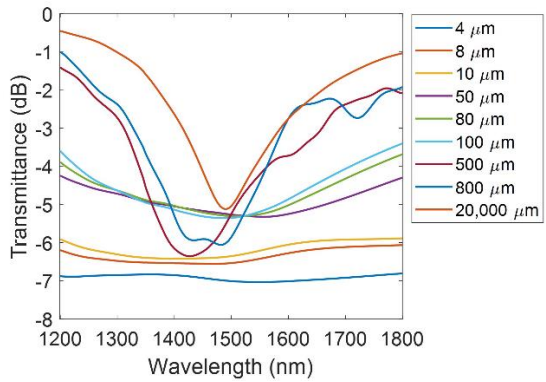

Fig. 3.4 Transmitted power for the coverslip with a thin film with a grating pattern for different values of the grating pitch (from 4 µm to 20,000 µm) over a total grating length of 20 mm.

In the case of the reflection bands, it can be checked in **Table 3.1** that their positions are the ones expected by using equation (3.2). Only the reflection bands corresponding to the cases with pitch values of 4 µm, 8 µm, and 10 µm (shown in **Fig. 3.5a**) are included in the table. The theoretical wavelengths have been calculated by employing n_{eff} = 1.508, which is the average refractive index value of soda lime glass in the studied range (from 1200 nm to 1800 nm) [33], as the refractive index of the structure will be close to this value. For clarity purposes, only the values that belong to the studied wavelength range are shown in the table.

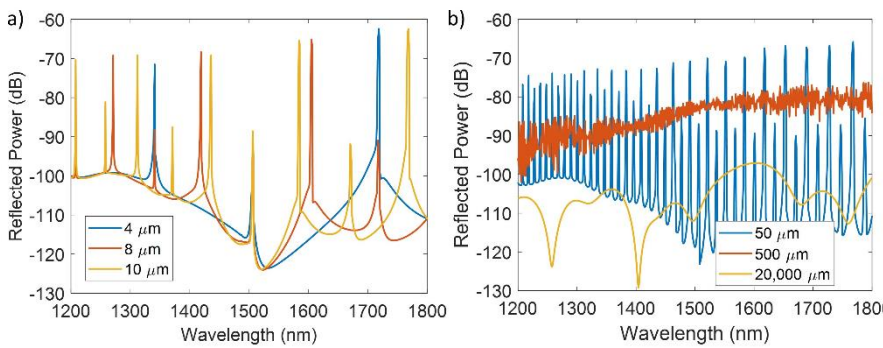

Fig. 3.5 Reflection bands for the coverslip with a thin film with a grating pattern for different values of the grating pitch over a total grating length of 20 mm. a) Results for a pitch of 4 µm, 8 µm, and 10 µm. b) Results for a pitch of 50 µm, 500 µm, and 20,000 µm.

Table 3.1 Theoretical and simulated wavelengths for the reflection bands generated with the grating pattern on the thin film deposited on the coverslip for different values of the grating pitch.

	Theoretical wavelengths from formula (nm)			**Wavelengths obtained in simulation (nm)**		
m	**Pitch**			**Pitch**		
	4 µm	**8 µm**	**10 µm**	**4 µm**	**8 µm**	**10 µm**
7	1723			1718		
8	1508			1506		
9	1340			1341		
10	1206			1208		
11-13						
14		1723			1717	
15		1609			1605	
16		1508			1506	
17		1419	1774		1419	1768
18		1340	1676		1341	1671
19		1270	1587		1271	1584
20		1206	1508		1208	1506
21			1436			1435
22			1371			1371
23			1311			1312
24			1257			1258
25			1206			1208

It can also be observed in **Fig. 3.5a** that the reflected power of the bands with odd *m* is higher than that of the bands with even *m* (see the values of *m* in **Table 3.1**). For instance, for a grating pitch of 4 µm, the reflection bands at 1723 nm (*m* = 7) and 1340 nm (*m* = 9) are more powerful than the ones at 1508 nm (*m* = 8) and 1206 nm (*m* = 10), with this last band hidden by the one located at the same wavelength corresponding to a grating pitch of 10 µm (more powerful because it corresponds to *m* = 25, odd value). Considering this distinction between bands with odd and even *m*, there are no relevant differences among the bands corresponding to different values of the grating pitch (peak values of around -70 dB for odd *m* values and -90 dB for even *m* values).

If the grating pitch is increased up to 50 µm (see **Fig. 3.5b**), the reflection bands are still visible, but as the pitch value is higher, these reflection bands correspond to higher values of *m* and are much closer together. It can still be appreciated the difference in power between the bands with odd and even m (although this difference is less important at shorter wavelengths). If the grating pitch is further increased to 500 µm (see again **Fig. 3.5b**), the reflection bands are so close to each other that they are no longer distinguishable with the employed resolution. It has to be considered that it was necessary to use this value for the grating pitch in order to generate an LMR (return to **Fig. 3.4**). For the largest grating pitch value that has been employed

(20,000 µm), no effect can be observed in **Fig. 3.5b**, except for some resonances that are considered artifacts without relevance.

In conclusion, after the performed analysis, to generate an LMR with the studied grating pattern it is necessary to employ a grating pitch (value around 500 µm) for which the reflection bands are no longer visible in the reflection spectrum. Therefore, this design is not adequate for generating both type of phenomena at the same time.

3.2.2.2. Coverslip (constant thickness section + grating pattern)

As a consequence of the problems that had been observed in the previous structure, it was decided to employ two different parts in the thin film pattern on the coverslip: a first homogeneous section without grating to generate the LMR and a second section with a grating pattern to produce the reflection bands, see again **Fig. 3.1b**. As in the previous case, TE polarization is used, the SnO_2 thin film thickness is 160 nm and SRI = 1. The length of the first section is 10 mm and the grating length of the second section is also 10 mm, where three cases had been assessed: grating pitch of 3 µm (3333 periods), 4 µm (2500 periods), and 5 µm (2000 periods). The reflections bands and the transmission spectrum for each of the cases are shown in **Fig. 3.6a** and **Fig. 3.6b** respectively.

It can be observed that the desired response is obtained, that is, bands appear in the reflection spectrum due to the gratings and an LMR is generated in transmission thanks to the homogeneous section. It can also be checked in **Table 3.1** that the positions of the reflection bands are the ones expected by using equation (3.2), calculated employing the same assumptions as in the previous case.

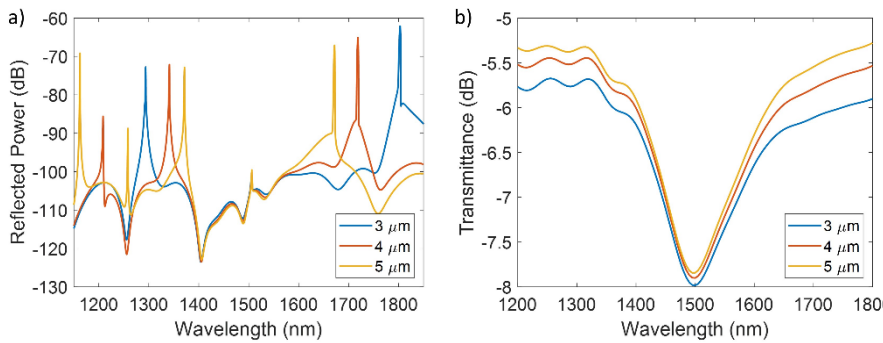

Fig. 3.6 Coverslip with a thin film with a section of constant thickness and a section with a grating pattern. a) Reflection bands for pitch values of 3 µm, 4 µm, and 5 µm. b) Transmission spectrum for pitch values of 3 µm, 4 µm, and 5 µm.

Nevertheless, it has to be considered that the LMR resonances are not very deep (between 2 and 2.5 dB depending on the value of the pitch) and the reflection bands are not very strong (the highest bands achieve values between -70 dB and -60 dB, which are not enough for a practical implementation of this device). In the case of the reflection bands located at around 1500 nm, the LMR resonances probably affect negatively their strength, but it is not the case of the other resonances. It has to be

remarked that it is not a question of resolution, as the resonance bands have been simulated with a precision of 10 pm. These problems could be solved, or at least attenuated, by increasing the length of the homogeneous section (the LMR resonances will get deeper) and the length of the grating section (the reflection bands will be stronger). However, this study has not been performed yet.

Table 3.2 Theoretical and simulated wavelengths for the reflection bands generated with the grating pattern on the thin film deposited on the coverslip for different values of the grating pitch.

	Theoretical wavelengths from formula (nm)			**Wavelengths obtained in simulation (nm)**		
m	**Pitch**			**Pitch**		
	3 µm	**4 µm**	**5 µm**	**3 µm**	**4 µm**	**5 µm**
5	1810			1803		
6	1508			1506		
7	1293	1723		1294	1718	
8		1508			1506	
9		1340	1676		1341	1672
10		1206	1508		1208	1506
11			1371			1371
12			1257			1258
13			1160			1162

3.2.2.3. D-shaped fiber (grating pattern)

As opposed to the previous two cases, here a D-shaped optical fiber was employed as substrate instead of a coverslip. In this subsection, the results obtained with a thin film with a grating pattern deposited on the D-shaped fiber (see **Fig. 3.1d**) are analyzed. A study of the impact of varying parameters from both the fiber and the grating is performed. For this device, only the reflection bands were studied, as it was not expected to be able to generate an LMR with an adequate pitch value for producing the reflection bands, based on the results that had been obtained for the coverslip.

It has to be remarked that the analysis that was performed for this structure is much deeper than the ones that have been carried out for the rest of devices. More parameters were assessed and not only the power but also the full width half maximum (FWHM) of the reflection bands (not studied for the rest of devices) was evaluated. Although it was desired to perform a study as detailed as the following one for the rest of the devices, the lack of time and the limited number of available software licenses narrowed the scope of the simulations for the rest of the structures. However, the results obtained for the current device enable to extract conclusions that are also valuable for the rest of structures.

An important difference between this study and those performed for the rest of structures is that in this case the surrounding medium is water (SRI = 1.33) as it was desirable to optimize this structure for its employment in biosensing applications. It would not be very problematic to repeat the analysis for the rest of devices using water instead of air as the surrounding medium and it is expected that their response would be very similar. The only relevant required change would be modifying the SnO_2 thin film thickness so the LMR (in the devices in which it is generated) was centered in the studied wavelength range in the new medium (a lower thickness would be needed in this case).

Initial results

The reflection bands obtained with this device are shown in **Fig. 3.7** for different pitches: 3 µm, 3.5 µm, 4 µm, 4.5 µm, 5 µm. These values were chosen because lower pitch values will increase the difficulty of manufacturing the structure while higher pitch values will lead to weaker resonances. The grating length is 20 mm (a typical length for the D-shaped section of the fiber [11]), the SnO_2 thin film thickness is 125 nm, the neck is 4 µm and TE polarized light is employed. It has to be remarked that the value of the neck (see again **Fig. 3.1f**) in a standard D-shaped fiber is 6.5 µm, but it has been decided to work with a 4 µm value because the reflection bands become stronger, as it will be seen afterwards.

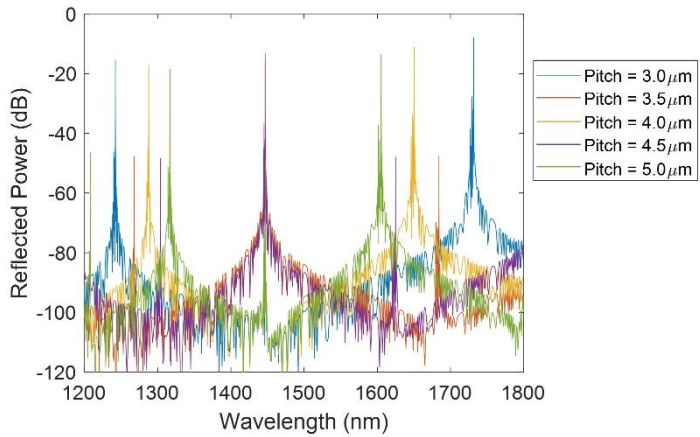

Fig. 3.7 D-shaped fiber with a thin film with a grating pattern. Reflection bands obtained for different values of the grating pitch from 3 µm to 5 µm and TE polarization. Reproduced under the terms of the CC BY 4.0 International License [24]. Copyright 2021, the Authors. Licensee MDPI, Basel, Switzerland.

In the analyzed wavelength range (1200 - 1800 nm), the refractive index of fused silica is approximately 1.445 [32] and the effective refractive index of the core mode (n_{eff}) is close to this value. The theoretical values for the position of the reflection bands, obtained by substituting n_{eff} = 1.44 in equation (3.2) and the different pitch values, are shown on the left side of Table 1. For the sake of clarity, only the points that fall in the studied range are shown. On the right side of **Table 3.3**, the values

obtained from the simulations are included, showing that there is a high correspondence between those values and the ones calculated with (2). It can be appreciated in **Fig. 3.7** that the reflected power of the bands with odd *m* is higher than that of the bands with even *m* (see the values of *m* in **Table 3.3**), a result that had already been observed in the case of the coverslip (see again **Fig. 3.5**).

Table 3.3 Theoretical and simulated wavelengths for the reflection bands generated with the grating pattern on the thin film deposited on the D-shaped optical fiber for different values of the grating pitch.

	Theoretical wavelengths from formula (nm)					**Wavelengths obtained in simulation (nm)**				
m	**Pitch**					**Pitch**				
	3.0 µm	**3.5 µm**	**4.0 µm**	**4.5 µm**	**5.0 µm**	**3.0 µm**	**3.5 µm**	**4.0 µm**	**4.5 µm**	**5.0 µm**
5	1734					1732				
6	1445	1686				1447	1684			
7	1239	1445	1651			1242	1447	1650		
8		1264	1445	1626	1806		1268	1447	1625	1802
9			1284	1445	1606			1288	1447	1605
10				1301	1445				1304	1447
11					1314					1317
12					1204					1208

In **Fig. 3.8**, the three reflection bands in the 1200 - 1800 nm range for a pitch of 4 µm are shown in detail for both polarizations. **Fig. 3.8a** corresponds to TE polarization and **Fig. 3.8b** to TM polarization. In the latter (TM), the reflection bands are lower in power (around 20 dB for $m = 7$ and $m = 9$, and 35 dB in the case of $m = 8$) and slightly blueshifted (the shift is between 5 and 20 pm and it is not perceptible in **Fig. 3.8**) compared to the former case (TE). Due to the better results obtained with TE polarization, the study will be focused on this case, to which **Fig. 3.7** corresponds.

For the following results, the simulations will be performed with a pitch of 4 µm, TE polarization, and focusing on the band located at 1650 nm as it is the most powerful one for the selected wavelength range and pitch. The study will focus on how the reflection band varies in power, wavelength, and FWHM by changing the different parameters of the structure (thickness of the thin film, neck, length). The optimum device will be selected considering the magnitude of the reflection, the FWHM, the sensitivity to the SRI, and the FOM.

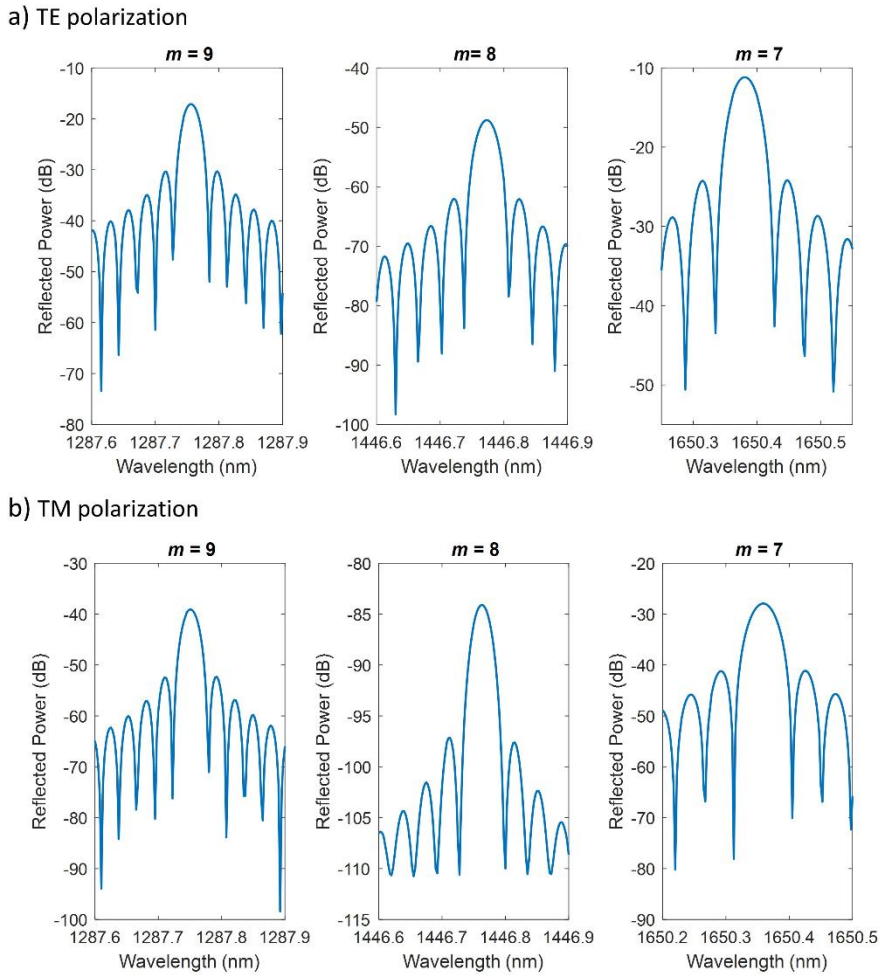

Fig. 3.8 D-shaped fiber with a SnO_2 thin film with a grating pattern with a pitch of 4 μm a) Close-up of the reflection bands for the TE polarization in the 1200 - 1800 range. b) Same as b) for the TM polarization. Reproduced under the terms of the CC BY 4.0 International License [24]. Copyright 2021, the Authors. Licensee MDPI, Basel, Switzerland.

Variations of the thin film thickness and the neck

In the first place, the effects of varying the thin film thickness and the neck were assessed. This analysis was carried out for SRI = 1.33 (water) and a length of the D-shaped zone of 20 mm (typical value). In **Fig. 3.9a**, the peak power of the reflection band is shown for values of the neck in the range from -2 μm to 6 μm and thin film thicknesses from 25 to 125 nm.

Regarding the neck, negative values mean that part of the core has been etched. For instance, a neck of -1 μm implies that 1 μm of the core has been etched. Lower (more

negative) values of the neck are not studied because they produce large mode loss and the peak is no longer recognizable in the reflection spectrum. Values of the neck higher than 6 µm are not assessed because the reflection band power decreases when the neck increases (see **Fig. 3.9a**). This is why it was decided to avoid working with D-shaped fibers standard neck value (6.5 µm). In the case of the thin film thickness, thicker values than 125 nm are not analyzed because the FWHM starts becoming higher (values of several tenths of nm), especially for low necks, which decreases the FOM and, hence, the performance of the device as a sensor.

In **Fig. 3.9a**, for a certain thin film thickness, in general, the peak power of the band slightly increases when the neck varies from -2 to -1 µm while it maintains a similar value for 0 µm and it clearly decreases in the range from 1 to 6 µm with a linear tendency of around -5dB/µm. The maximum occurs for a neck of -1 µm or 0 µm, with power values that are between -2.5 dB and -4.5 dB for thicknesses between 75 and 125 nm, around -7 dB for a thickness of 50 nm and -14 dB for a thickness of 25 nm. This behavior can be explained by the fact that with a lower neck the effective index of the core is more influenced by the thin film, and as the neck increases, the perturbation is reduced and hence the reflection band is not so clearly visualized in the optical spectrum.

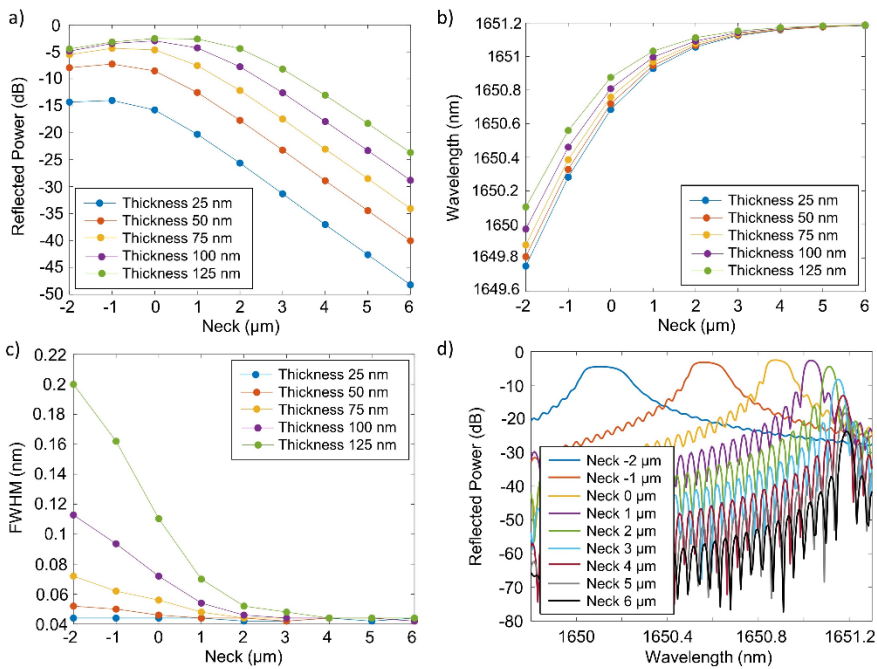

Fig. 3.9 a) Reflection band peak power (dB) versus neck (µm), b) Reflection band central wavelength (nm) versus neck (µm), and c) Reflection band FWHM (nm) versus neck (µm), for different values of the thin film thickness. d) Reflection bands for different necks and a thin film thickness of 125 nm. Reproduced under the terms of the CC BY 4.0 International License [24]. Copyright 2021, the Authors. Licensee MDPI, Basel, Switzerland.

In addition, in the case of a fixed neck, the power increases with the thin film thickness, which is again related to a higher perturbation in the effective index of the core mode with a thicker coating, closer to the mode transition region [36,37]. Here, two cases can be distinguished: for necks between -2 and 0 μm, the power variation as a function of thickness is not very relevant when the thickness is high (75 - 125 nm), whereas for positive values of the neck, the power difference among the different thicknesses tends to remain constant.

Regarding the central wavelength of the reflection band, it can be seen in **Fig. 3.9b** that this parameter is sensitive to the D-shaped fiber neck as well as to the deposited SnO_2 thickness. For a fixed thin film thickness, the band redshifts. This is much more evident for negative necks (0.4 - 0.5 nm) than for higher values of the neck (few pm), where the wavelength converges to 1651.2 nm. The higher sensitivity for lower necks is explained by the higher interaction of the core mode with the outer medium, which leads to a reduction of the core mode effective index [38]. On the other hand, the redshift drops with the thickness, as can be observed by comparing the wavelengths for the different thicknesses for a neck of -2 μm and a neck of 6 μm, where all the wavelengths have converged to 1651.2 nm. The higher sensitivity for lower thicknesses is explained by the countereffect produced by the mode transition phenomenon, which induces a higher increase in the core mode effective index as the coating thickness increases, reducing in this way the sensitivity induced by the reduction of the neck [36].

Another aspect that must be studied is the FWHM, which is shown in **Fig. 3.9c**. The FWHM increases with the thickness, but decreases with the neck, converging to values of around 45 pm. FWHM values start to be higher than 100 pm for negative values of the neck and thicknesses between 100 and 125 nm. FWHM could be even higher if the thickness is increased (points not shown).

As the main conclusion of this section, the highest power is achieved for thicker thin films (100, 125 nm) and low necks (0, -1 μm), but these values lead to wider FWHM. This increase in the FWHM has also been observed in the case of FBGs where the diameter of the cladding has been reduced [22], which is analogous to reducing the neck for the structure under study. In addition, it must be pointed out that, even though greater thin film thicknesses and lower necks have been avoided in order to prevent FWHM from further broadening, the FWHM is much more affected by the SRI, an effect that will be later studied along with the sensitivity.

To end this section, the reflections bands for a thickness of 125 nm and different values of the neck are included in **Fig. 3.9d**. This figure enables us to show some of the previously commented aspects. As the neck increases, the band decreases in power, shifts towards the red (the shift is greater for the lower necks), and its FWHM is reduced.

Variations of the length of the D-shaped zone

Until this point, the study has been carried out with a constant length of the D-shaped zone, 20 mm, a typical value for this parameter. Next, we describe the effect of varying the length of the D-shaped zone.

Simulations were carried out for thicknesses of 25, 75 and 125 nm with a neck of 0 µm and SRI = 1.33 (water). In **Fig. 3.10a**, it is shown that the power increases with the length, quickly achieving convergence for a thickness of 125 nm (length of 30 mm), requiring a bit more in the case of 75 nm (length of 50 mm) and still with some margin of improvement in the case of 25 nm (length of 80 mm). For all the thicknesses, it is notable that they tend to converge to a reflected power between -2.5 and -3 dB, although depending on the reflected power achieved for shorter lengths, they will require a smaller or greater increase in the length to converge. This agrees well with the conclusion obtained in the previous subsection, where thicker coatings led to reflection bands with higher power. Here, a higher perturbation was induced by a thicker coating, and with more periods, as it is analyzed in **Fig. 3.10a**, this lower reflected power observed with a thinner coating is progressively compensated.

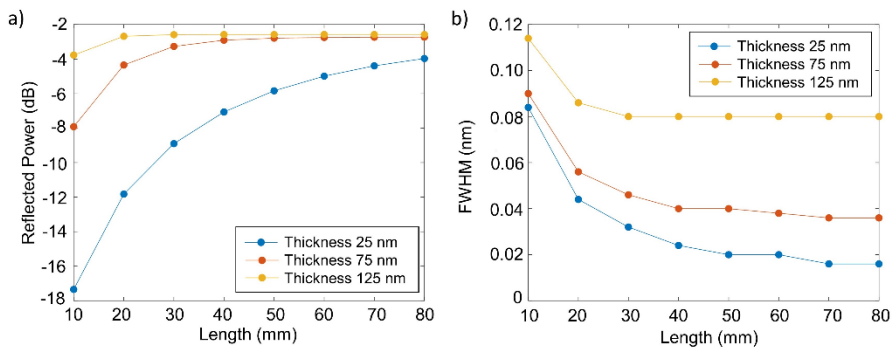

Fig. 3.10 a) Reflected band peak power (dB) vs. length (mm), and b) Reflected band FWHM (nm) vs. length (mm), for a neck of 0 µm and several thin film thicknesses. Reproduced under the terms of the CC BY 4.0 International License [24]. Copyright 2021, the Authors. Licensee MDPI, Basel, Switzerland.

On the other hand, in **Fig. 3.10b**, it can be observed that the FWHM decreases with the length, achieving a more or less constant value for a length of 40 mm: 80 pm for a thickness of 125 nm, 40 pm for 75 nm, and 20 pm for 25 nm. In the case of the thicknesses of 75 and 25 nm, the FWHM still drops a bit while the length continues increasing.

The main conclusion of this section is that the effect of increasing the length of the D-shaped zone is an increase in the power of the reflection band and a decrease in the FWHM width. This can also be observed in **Fig. 3.11**, where the reflection bands are shown for a thickness of 25 nm, neck of 0 µm, and lengths from 10 to 80 mm. However, it has been previously observed that a point is always reached where the power ceases increasing and the FWHM stops reducing. Finally, another aspect worth mentioning in **Fig. 3.11**, which had not appeared until now, is that the central wavelength of the reflection band is not sensitive to the length value.

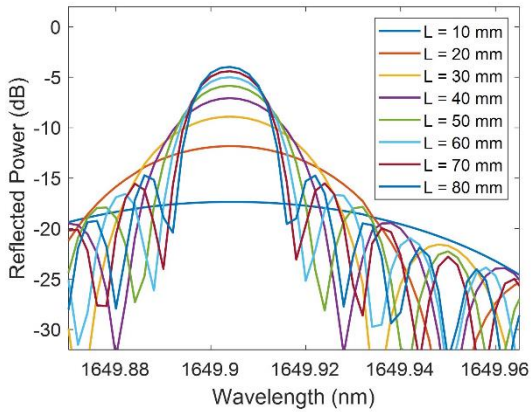

Fig. 3.11 Reflection bands for different values of the length of the D-shaped zone for a thin film thickness of 25 nm and a neck of 0 µm. Reproduced under the terms of the CC BY 4.0 International License [24]. Copyright 2021, the Authors. Licensee MDPI, Basel, Switzerland.

Variations of the SRI

First, the sensitivity to the SRI and the FOM of the reflection bands have been studied for a variation of the SRI between 1.33 and 1.4 for necks of -2, 0, and 2 µm. The D-shaped zone length was 20 mm because although increasing the grating length improves the reflected peak power, in practice it is not very realistic to work with lengths longer than 20 mm. The thickness of the SnO_2 thin film was fixed to 125 nm, a value that was selected because it leads to the reflection bands with the highest reflected power among the studied thicknesses.

In **Fig. 3.12a** the sensitivity increases with the value of the SRI and when the neck is thinner. This is coherent with the fact that FBGs have a greater sensitivity when the cladding diameter reduces [22], which happens because the effective index of the core is more affected by the external medium as the core is closer to it.

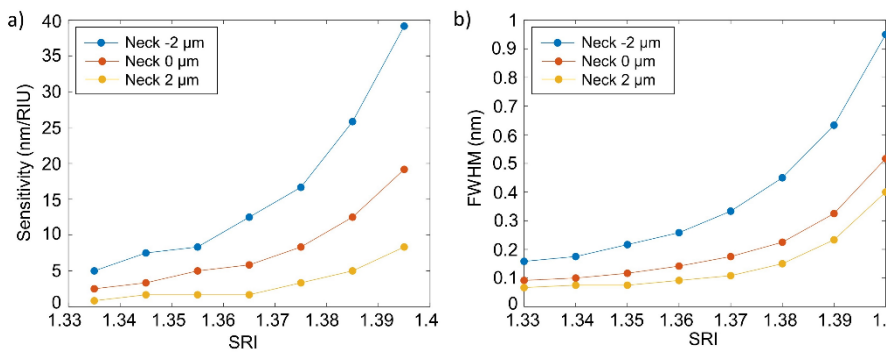

Fig. 3.12 a) Sensitivity to the SRI (nm/RIU) vs. SRI (RIU), and b) FWHM (nm) vs. SRI (RIU), for a thin film thickness of 125 nm and necks of -2, 0, and 2 µm. Reproduced under the terms of the CC BY 4.0 International License [24]. Copyright 2021, the Authors. Licensee MDPI, Basel, Switzerland.

Each point in the graph represents the sensitivity between the two refractive indices that are immediately below and above that point. It can be observed that for low values of the SRI, the sensitivity is around or below 5 nm/RIU. In the case of the highest SRI, the values achieved are in the 5 - 10 nm/RIU range for a neck of 2 μm, 10 - 20 nm/RIU for 0 μm, and 15 - 40 nm/RIU for -2 μm.

As it previously happened with the power, the main drawback of the sensitivity is that when it increases, the FWHM grows, achieving values of several tenths of nm for sensitivities that are above 10 nm/RIU if the corresponding points in **Fig. 3.12a** and **Fig. 3.12b** are compared.

In order to condense the information regarding the sensitivity to the SRI and the FWHM, the FOM was calculated for SRI = 1.34 and SRI = 1.40 (see **Table 3.4**). The lowest FOM values correspond to a neck of 2 μm, with values achieving at most 26.31 RIU^{-1} because, although the FWHM values are lower than for the rest of the neck values, the sensitivities are much lower. For a neck of 0 μm, the FOM increases from 26.08 to 45.54 RIU^{-1} between SRI = 1.34 and SRI = 1.40, while for a neck of -2 μm the FOM increases from 30.00 to 49.47 RIU^{-1}. The FOM values are similar because the higher sensitivities for a neck of -2 μm are compensated by narrower FWHMs in the case of the neck of 0 μm, although they are slightly better in the case of -2 μm.

Table 3.4 FOM (RIU^{-1}) for a thin film thickness of 125 nm.

	Neck		
SRI	**-2 μm**	**0 μm**	**2 μm**
1.34	30.00	26.08	11.76
1.40	49.47	45.54	26.31

Consequently, both a thin film thickness of 125 nm and a neck of -2 μm or 0 μm constitute a good parameter selection to implement a real device, as they have similar high FOMs and high power, as it was seen in **Fig. 3.9a**. The final choice between the neck of -2 μm or 0 μm depends on whether the sensitivity (higher for -2 μm) or the FWHM (narrower for 0 μm) is prioritized.

In **Fig. 3.13**, the FBG bands are shown for a thin film thickness of 125 nm and a neck of 0 μm for SRI ranging from 1.33 and 1.4. It is clear, as has been previously described, that the sensitivity rises with the SRI (the redshift in **Fig. 3.13** increases with the SRI), but the FWHM widens. The reflected power does not significantly change.

Finally, to end this study, the effect of reducing the thin film thickness was analyzed. From previous results, diminishing the thickness will lower the power and the FWHM but it is still unknown what will occur with the sensitivity and the FOM. In this last part of the analysis, the sensitivity of the reflection bands and the FOM were analyzed for a variation of the SRI between 1.33 and 1.4 for a neck of -2 μm and thicknesses of 25 nm, 75 nm, and 125 nm, while the length of the D-shaped zone was fixed to 20 mm.

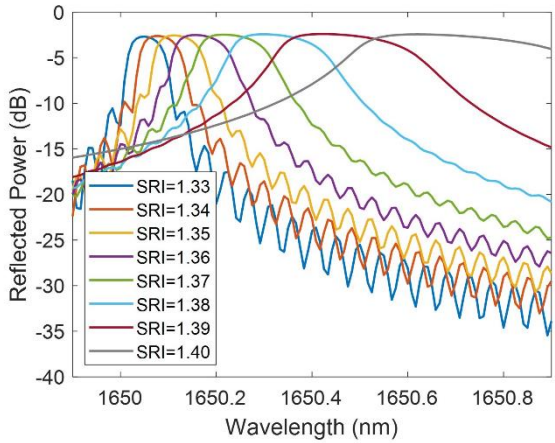

Fig. 3.13 Reflection band for different SRI for a thin film thickness of 125 nm and a neck of 0 µm. Reproduced under the terms of the CC BY 4.0 International License [24]. Copyright 2021, the Authors. Licensee MDPI, Basel, Switzerland.

It can be observed in **Fig. 3.14a** that the sensitivity increases as a function of the SRI and the thin film thickness, an effect that is related to the higher proximity to the mode transition region when the thin film is thicker [36]. For a thickness of 25 nm, the sensitivity is below 5 nm/RIU for most of the points, achieving a value of 6.67 only between SRI of 1.39 and 1.4. In the case of the 75 nm thickness, for an SRI between 1.33 and 1.37, the sensitivity is below 5 nm/RIU, while values between 5 and 15 nm/RIU are achieved between SRI of 1.38 and 1.4. With a thickness of 125 nm the highest sensitivities are obtained, with values between 5 and 10 nm/RIU between SRI of 1.33 and 1.36 that quickly rise for higher SRI, even reaching values of 39 nm/RIU.

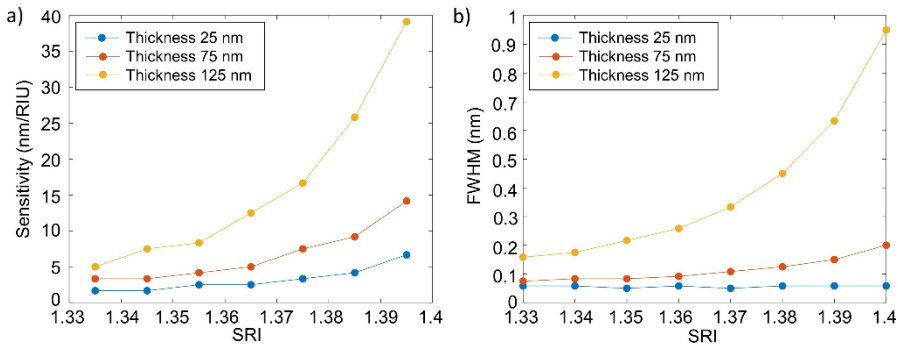

Fig. 3.14 a) Sensitivity to the SRI (nm/RIU) vs. SRI (RIU), and b) FWHM (nm) vs. SRI (RIU), for a neck of -2 µm and thin film thicknesses of 25nm, 75 nm, and 125 nm. Reproduced under the terms of the CC BY 4.0 International License [24]. Copyright 2021, the Authors. Licensee MDPI, Basel, Switzerland.

Again, the weakest point in attaining a high sensitivity is that the FWHM of the corresponding reflection band widens, as it can be seen in **Fig. 3.14b**. Nevertheless, in the case of the 75 nm thickness, the sensitivities are between 3 and 15 nm/RIU for FWHM between 70 and 200 pm, which can be considered an adequate trade-off between sensitivity and FWHM.

To summarize the information provided by the sensitivity to the SRI and the FWHM, the FOM is calculated for SRI = 1.34 and SRI = 1.40 (see **Table 3.5**). In this case, the FWHM has more influence in the comparison between the results for the different thicknesses. The best FOM values are achieved for a thickness of 25 nm due to their very low FWHMs, varying from 28.57 to 114.29 RIU^{-1} between SRI = 1.34 and SRI = 1.40. In the case of the thickness of 75 nm, the FOM increases for 42.10 to 80.95 RIU^{-1} in this range, while for 125 nm it varies from 30.00 to 49.47 RIU^{-1} as has been previously seen in **Table 3.4**.

Table 3.5 FOM (RIU^{-1}) for a neck of -2 µm.

	Thin film thickness		
SRI	**25 nm**	**75 nm**	**125 nm**
1.34	28.57	42.10	30.00
1.40	114.29	80.95	49.47

Therefore, it can be concluded that the FOM increases when the thin film is reduced. Consequently, doubt may arise as to whether a thickness of 125 nm and a neck of -2 µm constitute a good choice of parameters, as was previously mentioned, or whether it is better to reduce the thickness. It has to be considered that greater FOMs for low thicknesses are achieved thanks to lower FWHMs, while the sensitivities are much lower. As a result, a trade-off solution would be choosing a thickness of 75 nm with a neck of -2 µm. The sensitivities are not the highest ones (between 3 and 15 nm/RIU), but the power is high (see again **Fig. 3.9a**) and the FOM is high (between 40 and 80 RIU^{-1}).

In **Fig. 3.15**, the FBG bands are shown for a neck of -2 µm and a thin film thickness of 75 nm with SRI between 1.33 and 1.4. The sensitivity rises with the SRI (the redshift in **Fig. 3.15** increases with the SRI) but the FWHM broadens.

The first conclusion of this section is that the sensitivity is favored by a thicker thin film, a low (negative) neck and a high SRI. It is not difficult to reach sensitivities between 5 - 10 nm/RIU and even higher if the different parameters are properly combined to achieve the optimum. However, sensitivities higher than 10 nm/RIU come at the cost of increasing the FWHM up to several tenths of nanometers.

Regarding the FOM, it increases with a low (negative) neck and reduces with the thin film thickness. High values (between 40 and 80 RIU^{-1}) are obtained but they require a high sensitivity (which will have the disadvantage of a wide FWHM) or a narrow FWHM (which will present, as a drawback, a low sensitivity).

Comparing the results for the structure under analysis obtained in this section with the FBG-based sensors studied in [22], in the case of the maximum sensitivity (39 nm/RIU), it would be an acceptable value in spite of being far from the top sensitivities, which can reach values of hundreds or even thousands of nm/RIU. Regarding the FOM, values between 40 and 80 RIU^{-1} (the highest one was 114.29 RIU^{-1}) are quite high, only being surpassed by very few sensors from [22]. In the case of the FWHM, the lowest values, around 45 pm, are better than those attained with any FBG-based sensor in [22]. It has to be considered that not all the parameters (sensitivity, FOM, FWHM) of the structure can be optimized at the same time, so some of them will have to be prioritized.

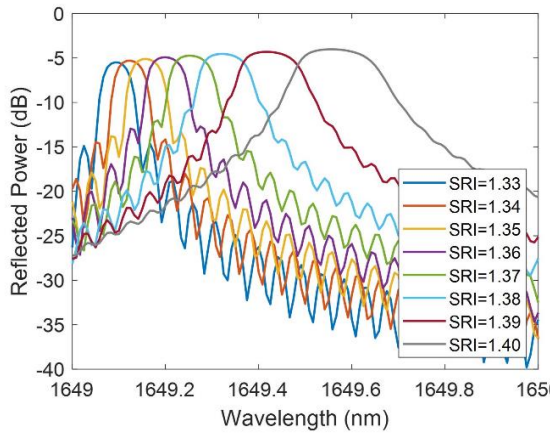

Fig. 3.15 Reflection band for different SRI for a neck of -2 µm and a thin film thickness of 75 nm. Reproduced under the terms of the CC BY 4.0 International License [24]. Copyright 2021, the Authors. Licensee MDPI, Basel, Switzerland.

3.2.2.4. D-shaped fiber (constant thickness section + grating pattern)

Initial results

Finally, the second thin film design (a section of constant thickness and a section with a grating pattern) has been simulated on the D-shaped optical fiber. TE polarization is employed, the SnO_2 thin film thickness is 150 nm (it has been selected so the LMR is centered in the studied wavelength range), the neck of the D-shaped fiber is 4 µm and SRI = 1. The length of the first section is 10 mm, the same as the grating length of the second section. As it is expected in this case, both the reflection bands (due to the grating pattern) and the LMR (thanks to the section of constant thickness) are generated, as it is shown in **Fig. 3.16a** and **Fig. 3.16b**, respectively, for values of the grating pitch of 3 µm, 4 µm, and 5 µm.

In the case of the reflection bands, they are obtained at the same wavelengths as in the previous device (see the cases corresponding to a grating pitch of 3 µm, 4 µm, and 5 µm in **Table 3.3**). The only exception are the bands located at 1447 nm, whose disappearance is considered to be caused by the LMR, which is approximately at 1500 nm. Regarding the LMR, the same result is obtained for all three cases, which

means that the grating section does not have any impact on its generation. Its great depth (around -70 dB) is due to the value chosen for the neck (-4 µm), selected to obtain powerful reflection bands, but the LMR would not be so deep in a real implementation.

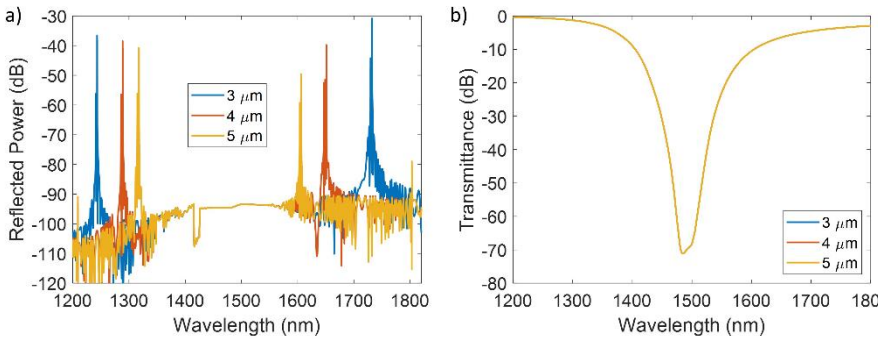

Fig. 3.16 D-shaped fiber with a thin film with a section of constant thickness and a section with a grating pattern. a) Reflection bands and b) Transmission spectrum, obtained for different values of the grating pitch from 3 µm to 5 µm.

Variations of the length of the sections

The length of both sections of the thin film has been varied to check their effect on the peak power of the reflection bands and the depth of the LMR. These analysis have been performed with a grating pitch of 4 µm and studying the reflected power of the bands located at 1289 nm (m = 9) and 1651 nm (m = 7).

In the first place, the length of the grating section has been varied from 5 mm to 35 mm (equivalent to increasing the number of grating periods from 1250 to 8750) while maintaining the length of the section of constant thickness equal to 10 mm. It can be observed in **Fig. 3.17a** that the peak power of the reflection bands rises with the grating length, being the increase very similar for both bands. The peak at 1289 nm goes from around -45 dB to -28 dB nm when varying the grating length from 5 mm to 35 mm (the increase is faster for the shorter lengths) and the peak at 1651 nm from approximately -46 dB to -29 dB. The reflection bands at 1289 nm for the different grating lengths are shown in **Fig. 3.17b**. Here, it can be noted that the peak wavelength does not change with the grating length. Moreover, it is important to note that the increase of the reflected power with the grating length is accompanied with a reduction of the FWHM. The same conclusions had been obtained for the gratings shown in the previous device.

Regarding the LMR, it can be appreciated in **Fig. 3.17c** that the general tendency when enlarging the grating length is an increase in the depth of the resonance, with a value of -69 dB for a grating length of 5 mm and a value of -90 dB for a grating length of 35 mm. However, the depth of the resonance reduces from 15 to 20 mm and from 25 to 30 mm. These changes in the tendency are attributed to the fact that the spectrum starts to deteriorate and present strange peaks (see **Fig. 3.17d**) with the increasing grating length, which is a common result when simulating resonances that

are far deeper than real ones. In a real implementation, it would be expected to have an increase in the depth of the resonance with the grating length without these artifacts, although the resonances would be not as deep as the ones seen in simulation.

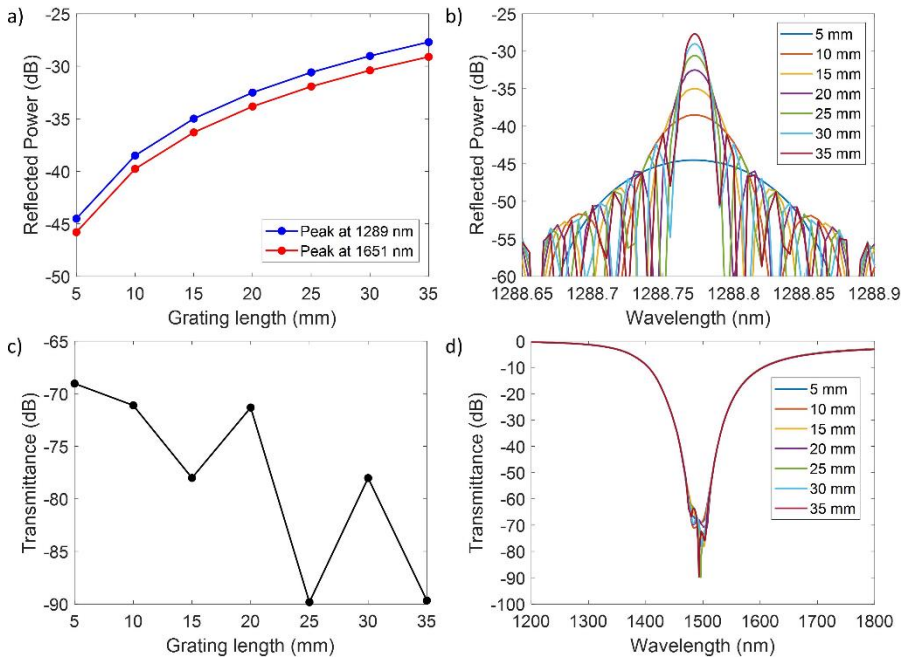

Fig. 3.17 Results for a variation of the grating length from 5 mm to 35 mm a) Peak power of the reflection bands at 1289 nm and 1651 nm. b) Reflection band at 1289 nm. c) Depth of the LMR resonance. d) Transmission spectrum.

Then, the length of the section of constant thickness has been increased from 5 mm to 35 mm while maintaining the grating length equal to 10 mm (2500 grating periods). It can be observed in **Fig. 3.18a** that the power of both studied reflection bands decreases with the length of the section of constant thickness. In particular, the band at 1651 nm is much more affected (decrease from -33.6 dB to -70 dB from 5 mm to 35 mm in an almost linear trend) than the band at 1289 nm (from -37.5 dB to -43.5 dB, also following a linear tendency). Previous observation is in accordance with the fact that the resonance located at 1651 nm is nearer to the LMR central wavelength (around 1500 nm) than the resonance located at 1289 nm (149 nm vs 211 nm). The reflections bands at 1651 nm as a function of the length of the section of constant thickness are shown in **Fig. 3.18b**, where it can be appreciated that neither the central peak wavelength nor the FWHM change. However, for lengths greater than 25 mm, the reflection band begins to distort.

At the same time, the depth of the LMR resonance increases with the length of the section of constant thickness (see **Fig. 3.18c**), as it was expected, with a value of - 40 dB for a length of 5 mm and a value of -119 dB for 35 mm. Again, in the case of the LMR, these results have to be mostly interpreted in a qualitative way. They

cannot be considered reliable as the transmission spectrum starts to distort as the length is increased (see **Fig. 3.*18*d**), because the resonances are too deep. In a real implementation, it would be expected to have an increase in the depth of the resonance with the length of the section of constant thickness without these artifacts, although the resonances would be not as deep as the ones seen in simulation. This increase in the depth would be larger than the one achieved by increasing the grating length by the same amount (previously studied case) as the effective length of material that is added in this case is half (the duty cycle of the grating is 0.5).

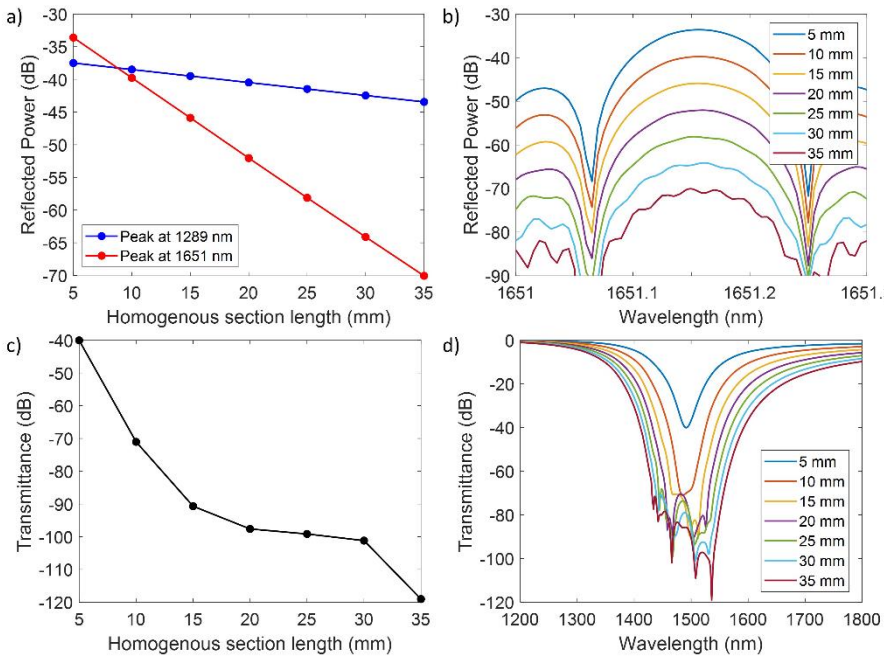

Fig. 3.18 Results for a variation of the length of the section with constant thickness from 5 mm to 35 mm a) Peak power of the reflection bands at 1289 nm and 1651 nm. b) Reflection band at 1651 nm. c) Depth of the LMR resonance. d) Transmission spectrum.

To summarize this section, two different thin film grating patterns have been studied on two different substrates: a coverslip and a D-shaped optical fiber. The first design consisted of a pure grating pattern and it has been demonstrated that the position of the bands in the reflection spectrum can be predicted with the Bragg-Snell equation for normal incidence. The influence of the different parameters over the reflection bands has been studied in more depth in the case of the D-shaped optical fiber. The second design consisted of the combination of a thin film section with constant thickness and another one with a grating pattern and it has been shown that this design is capable of generating both an LMR in transmission and bands in the reflection spectrum in both substrates, which was the original purpose behind this study. The next steps would be the practical implementation of these devices and the characterization of both phenomena (LMR and reflection bands) for different parameters (temperature, strain, SRI), in order to develop multisensing platforms.

3.3. LMR based refractometer with FBG temperature compensation

In this section, the combination of an LMR and an FBG is implemented on a D-shaped optical fiber for measuring simultaneously the SRI and the temperature with a single device. The LMR is obtained through the deposition of a TiO_2 thin film while the FBG is inscribed on the core of the optical fiber. First, the employed materials and methods are described and then, the device response to changes in the SRI and temperature is characterized. Finally, its performance is compared with other sensors with similar characteristics.

3.3.1. Materials and methods

D-shaped fibers were purchased from Phoenix Photonics LTD and consist of standard single mode fibers (Corning® SMF-28) with a cladding/core diameter of 125/8 µm and a polished length of 10 mm. These fibers are polished until obtaining an attenuation peak of 0.5 dB at 1550 nm in high refractive index oil (RI = 1.5).

Firstly, FBGs were inscribed in the core of the D-shaped region of the fiber with the FBG peak located around 1533 nm. Fiber writing was performed using the phase mask method (period of 529.8 nm over a length of 3 mm) using a Coherent® Xantos XS laser at 193 nm emission wavelength, 250 Hz repetition rate and 1.5 mJ/pulse.

Afterwards, a thin film of 60 nm of TiO_2 is deposited onto the D-shaped zone using the atomic layer deposition (ALD) technique with the Savannah G2 ALD System from Veeco Inc. The final structure can be observed in **Fig. 3.19**. TiO_2 has been selected because this material provides a good SRI sensitivity (4122 nm/RIU for a D-shaped LMR based refractometer with the resonant wavelength at 1300 nm in [13]).This thickness was chosen in order to obtain a first order LMR_{TE} (electric polarization) at a wavelength of around 1400 nm. This means that the FBG peak is far enough to guarantee that the resonance does not affect the intensity of the FBG.

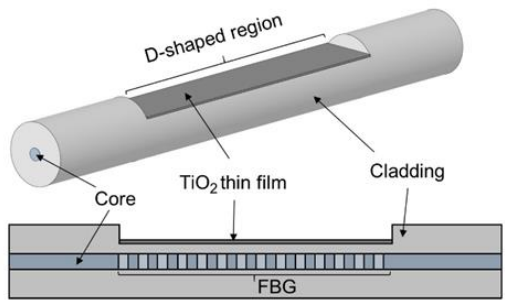

Fig. 3.19 Designed structure consisting of an FBG inscribed in the core and a TiO_2 nano-film covering the D-shaped region (top) and section view of the device (bottom). Reproduced under an Open Access License [39]. Copyright 2022, Optica Publishing Group.

In the measuring setup, see **Fig. 3.20**, a multi-SLD light source (FJORD-X3-1330-1650, Pyroistech S.L.) is connected to input 1 of an optical circulator through an in-line polarizer and a polarization controller (Phoenix Photonics Ltd), which enables selecting the TE- or TM-polarized state of light [5]. One end of the D-shaped optical

fiber is connected to output 2 of the circulator and the other end of the fiber is connected to an optical spectrum analyzer (MS9740A from Anritsu) to monitor the power in transmission. Once the polarization state has been adjusted, the fiber is fixed so the polarization state does not change. Output 3 of the optical circulator is connected to an interrogator (I-MON 512 USB from Ibsen Photonics A/S) that enables to monitor the FBG peak in reflection.

The D-shaped region is placed inside a microfluidic system that is thermo-stabilized by means of two Peltier cells, as in [40]. It consists of two equal-size bars, the upper one is made of ULTEM® and the lower one is made of stainless steel. A microfluidic channel is engraved on both bars with dimensions 1 mm × 1 mm × 50 mm (volume of 50 μL), with the D-shaped region fitting in this channel. A peristaltic pump allows to control the flow through the cell.

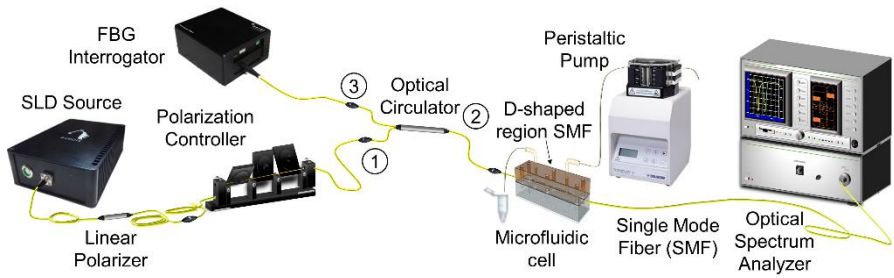

Fig. 3.20 Schematic representation of the experimental setup. Reproduced under an Open Access License [39]. Copyright 2022, Optica Publishing Group.

3.3.2. Results

Two assays were carried out with the setup shown in **Fig. 3.20**. In the first experiment, the device response to SRI was monitored, while the temperature was stabilized at 25ºC. The LMR response is shown in **Fig. 3.21** whilst the FBG response is shown in **Fig. 3.22**. The first refractive index corresponds to ultrapure water and the remaining correspond to solutions of glucose in ultrapure water with values of 1.3324, 1.3367, 1.3407, 1.3445 and 1.3479 respectively, measured at 589.3 nm with refractometer Refracto30GS (Mettler Toledo Inc). The device was tested with these indices because the aim is to use it with liquids of refractive index close to that of water.

In **Fig. 3.21** it can be observed that the resonance wavelength shifts linearly with a sensitivity of 3725.2 nm/RIU in the studied range. In **Fig. 3.22**, it can be seen that the FBG peak shift with refractive index is very small. In particular, the variation of the FBG peak in the studied SRI range was of only 12 pm, which corresponds to a sensitivity lower than 1 nm/RIU, which is negligible in comparison with the LMR sensitivity to the SRI. The FBG peak is slightly sensitive to the SRI as the cladding thickness between the core and the polished surface of the fiber is very thin (6.5 μm), as it happens in the case of FBGs inscribed in etched fibers [22].The axis limits in **Fig. 3.22** have been chosen in order to enable a direct comparison with Fig. 6. Before performing the second experiment, in which the temperature is varied, the system

returns to the initial operating conditions (ultrapure water). It can be checked that the starting operation points of both experiments (LMR resonance located at 1378 nm and FBG peak at 1533.1 nm) are virtually the same, although there is sometimes a small hysteresis (less than 5 nm) when returning to the initial operating conditions after a SRI variation and/or a temperature variation.

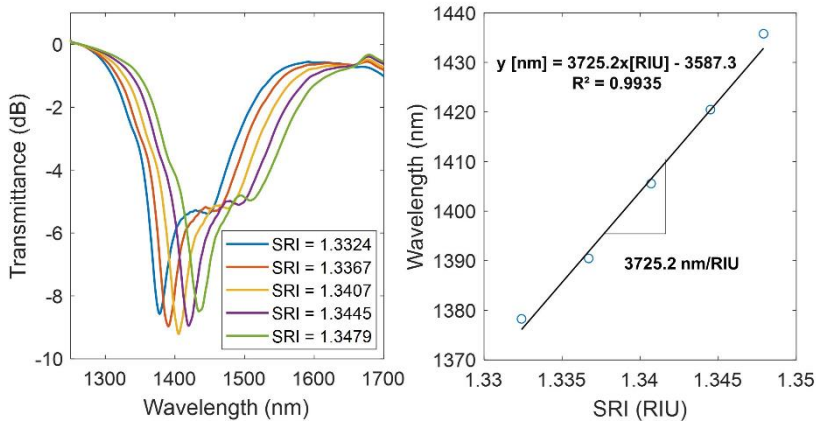

Fig. 3.21 Spectral response of the LMR when the D-shaped region is immersed in five different refractive index. Reproduced under an Open Access License [39]. Copyright 2022, Optica Publishing Group.

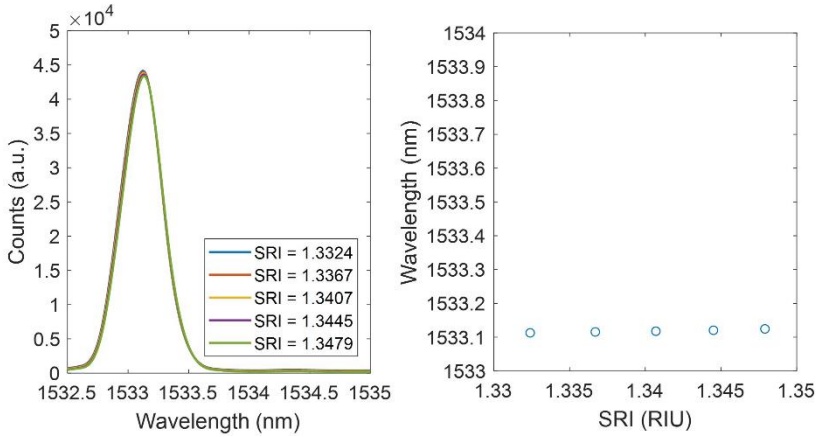

Fig. 3.22 Spectral response of the FBG when the D-shaped region is immersed in five different refractive index. Reproduced under an Open Access License [39]. Copyright 2022, Optica Publishing Group.

The second experiment consisted in varying the temperature from 25ºC to 45ºC in steps of 5ºC while maintaining the D-shaped region of the fiber immersed in ultrapure water. The LMR response for this assay is presented in **Fig. 3.23** while the FBG response is shown in **Fig. 3.24**. In this second experiment, the shape of the resonance is different compared to that observed in **Fig. 3.21**, because it is difficult to reproduce the very same polarization state in both experiments. Slight variations in the

polarization state can lead to differences in the depth of the main resonance around 1380 - 1400 nm (slightly deeper in **Fig. 3.21** compared with **Fig. 3.23**) and the residual lobe that appears at higher wavelengths (deeper in **Fig. 3.23**).

Regarding the results of the second experiment, in **Fig. 3.23**, the resonance wavelength shifts towards the blue when the temperature increases. The purpose of the plot on the right of **Fig. 3.23** will be explained afterwards. In **Fig. 3.24**, the FBG peak shifts towards the red when the temperature increases, with a linear sensitivity of 32.6 pm/ºC in the studied range. The expected temperature sensitivity for an FBG at around 1550 nm is approximately 13.7 pm/ºC [41]. In the case under study, the FBG is inscribed in the core of a fiber that is glued to the upper half of the microfluidic cell. Therefore, the dilatation of the microfluidic cell with temperature also affects the temperature sensitivity.

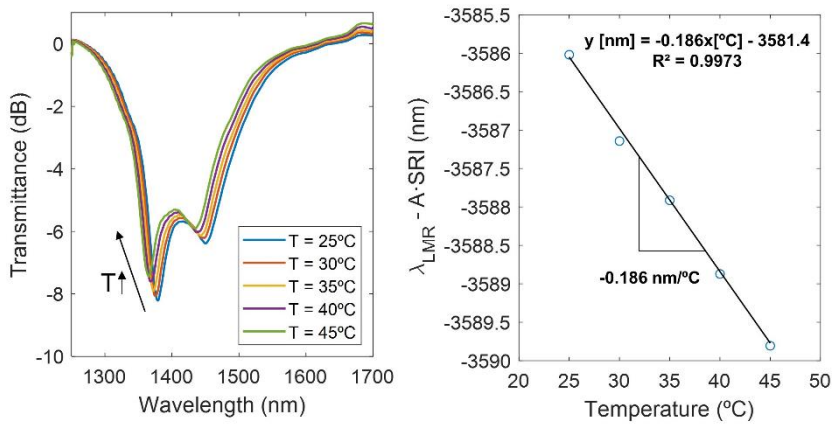

Fig. 3.23 Spectral response of the LMR when the temperature is varied (left) and calculation of coefficient B (right). Reproduced under an Open Access License [39]. Copyright 2022, Optica Publishing Group.

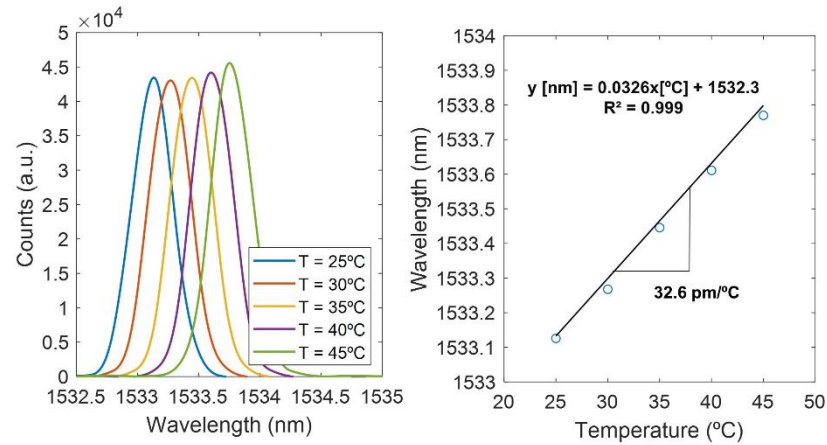

Fig. 3.24 Spectral response of the FBG when the temperature is varied. Reproduced under an Open Access License [39]. Copyright 2022, Optica Publishing Group.

The results from the previous experiments can be employed to obtain a sensitivity matrix that correlates the variation in the SRI and temperature (ΔSRI and ΔT respectively) between two operation points with the wavelength shifts of the LMR and the FBG ($\Delta\lambda_{LMR}$ and $\Delta\lambda_{FBG}$ respectively), as it is shown in equation (3.3).

$$\begin{pmatrix}\Delta\lambda_{LMR}\\ \Delta\lambda_{FBG}\end{pmatrix} = \begin{bmatrix}A & B\\ C & D\end{bmatrix}\begin{pmatrix}\Delta SRI\\ \Delta T\end{pmatrix} \tag{3.3}$$

In the first experiment $\Delta T = 0$, so $\Delta\lambda_{LMR} = A \cdot \Delta SRI$ and from **Fig. 3.21**, A = 3725.2 nm/RIU. The FBG sensitivity to the SRI is negligible in comparison to the LMR sensitivity, as it can be checked in **Fig. 3.22**, thus it can be considered that $C \approx 0$.

In the second experiment, both ΔSRI and ΔT are different from 0. The SRI changes because the refractive index of a liquid varies with temperature. However, as $C \approx 0$, $\Delta\lambda_{FBG} = D \cdot \Delta T$, and from **Fig. 3.24**, D = 32.6 pm/ºC. Finally, B can be calculated from equation (3.4) as:

$$B = \frac{\Delta\lambda_{LMR} - A \cdot \Delta SRI}{\Delta T} = \frac{\Delta(\lambda_{LMR} - A \cdot SRI)}{\Delta T} \tag{3.4}$$

Therefore, if $\lambda_{LMR} - A \cdot SRI$ is plotted vs the temperature, B is the slope of the linear response that is obtained, as it is shown on the right of **Fig. 3.23**, with B = -0.186 nm/ºC. The values of the SRI of water for the different temperatures have been obtained from [42].

The calibration to obtain these coefficients should be repeated each time a new fiber is employed by simply following the previous steps, which could be performed automatically if necessary.

If both sides of equation (3.3) are multiplied by the inverse of the sensitivity matrix, the unknown ΔSRI and ΔT for certain values of $\Delta\lambda_{LMR}$ and $\Delta\lambda_{FBG}$ can be obtained, as it is shown in equation (3.5). The values that correspond to this case are substituted in equation (3.6).

$$\begin{pmatrix}\Delta SRI\\ \Delta T\end{pmatrix} = \begin{bmatrix}A & B\\ C & D\end{bmatrix}^{-1}\begin{pmatrix}\Delta\lambda_{LMR}\\ \Delta\lambda_{FBG}\end{pmatrix} \tag{3.5}$$

$$\begin{pmatrix}\Delta SRI\\ \Delta T\end{pmatrix} = \begin{bmatrix}2.684 \cdot 10^{-4} & 1.532 \cdot 10^{-3}\\ 0 & 30.675\end{bmatrix}^{-1}\begin{pmatrix}\Delta\lambda_{LMR}\\ \Delta\lambda_{FBG}\end{pmatrix} \tag{3.6}$$

Once ΔSRI and ΔT are obtained, the temperature of the final operation point and the value of the SRI at that temperature can be calculated if these values are known at the initial operation point. Note that, as opposed to other sensors, the SRI value is not provided at the initial reference temperature, but at the temperature that is being measured simultaneously.

With this calibration, the intrinsic drift with temperature of the device is compensated, so the device can be employed to measure the temperature and the

refractive index not only of ultrapure water, the liquid used in the calibration, but also of other liquids. In order to demonstrate the importance of this calibration, the results of supposing $B = 0$, that is, not compensating the effect of the temperature over the device operation, are shown in **Table 3.6** for the results of the second experiment.

Table 3.6 Estimated error when supposing $B = 0$.

T (ºC)	SRI (RIU)	$\Delta\lambda_{LMR}$ (nm)	ΔSRI (RIU) ($B = 0$)	SRI (RIU) ($B = 0$)	Error (%)
25	1.3328	0	0	1.3328	0
30	1.3323	-3.10	-8.31E-04	1.3320	-0.02
35	1.3316	-6.36	-1.71E-03	1.3311	-0.04
40	1.3310	-9.85	-2.65E-03	1.3302	-0.06
45	1.3302	-13.73	-3.69E-03	1.3291	-0.08

The first three columns in **Table 3.6** correspond to the temperature (ºC), the real SRI (RIU) calculated from [42] and $\Delta\lambda_{LMR}$ (nm) respectively. The fourth column corresponds to ΔSRI (RIU) assuming $B = 0$ (wrong calculation). The fifth column corresponds to the wrong SRI (RIU) derived from the wrong ΔSRI and the last column to the relative error in %. It can be deduced from this table that the effect of temperature on the device operation cannot be ignored for applications where a precise measurement of the SRI is required, such as gas sensing or biosensing applications. Although the error might seem negligible in percentage, it becomes more relevant if it is taken into account that it can affect the fourth and third decimals of the SRI.

For the sake of comparison, a table is included with the main characteristics of this device and some works where both the SRI and the temperature are measured (see **Table 3.7**). Regarding the temperature sensitivity, its value is good compared with other sensors that employ FBGs [16,17] but low in the case of the sensors that combine resonances with the use of PDMS [43,44]. On the other hand, it can be observed that the SRI sensitivity of the obtained device is high when compared with sensors included in **Table 3.7** (only surpassed by [45]) and in particular taking into account that most of the devices are tested with higher values of the SRI. However, it must be considered that there are also similar refractometers to the one obtained here (based on a D-shape structure), with higher sensitivities. For example, the highly sensitive refractometers described in refs. [46] (5855 nm/RIU for an LMR based on ITO), [11] (14,501 nm/RIU for an LMR based on SnO_2) or [47] (22,779 nm/RIU for an SPR obtained with Au deposited on a polymer fiber), although they do not include temperature compensation. Therefore, it would be interesting to reach these sensitivities while at the same time maintaining the temperature measuring capability.

Table 3.7 Comparison with other works where both the SRI and the temperature are measured.

SRI sensing mechanism	SRI sensitivity (nm/RIU)	SRI range (RIU)	Temp. measuring mechanism	Temp. sensitivity	Temp. range (ºC)	Ref.
FBG	1.284 -12.77	1.3333 - 1.3800	FBG	9.39 - 10.07 pm/ºC	25 - 65.5	[16]
FBG	535.14	1.33 - 1.454	FBG	10.06 pm/ºC	20.3 - 99.5	[17]
TFBG	606.82	1.3761 - 1.4327	LPFG	268.79 pm/ºC	-30 - 70	[18]
TFBG-SPR	571.5	1.3325 - 1.3375	TFBG-SPR	6.3pm/ºC	23 - 59	[19]
LRSPR	4111.67	1.3317 - 1.3365	Terbium(III) absorption	0.05 dB/ºC	15 - 50	[45]
SPR	2260.1	1.333 - 1.390	SPR + PDMS	-2.41 nm/ºC	20 - 60	[43]
LMR	1460	1.3328 - 1.37	LMR + PDMS	-1.75 nm/ºC	20 - 40	[44]
Slot waveguide ring resonator	240	(not provided)	Slot waveguide ring resonator	16.6 pm/ºC	23 - 33	[48]
LMR	3725.2	1.3324 – 1.3479	FBG	32.6 pm/ºC	25 - 45	This work

3.4. Dual LMR based sensor on a single D-shaped optical fiber

The last device that is proposed in this chapter is a D-shaped optical fiber where two independent LMRs are obtained through the deposition of a nanocoating with two sections of different thickness. The fabrication process is explained in detail and it is studied how to optimize the length of the sections of the nanocoating so both resonances have a similar depth. The experimental results are supported with numerical simulations. Finally, the performance of the device as a refractometer is assessed.

3.4.1. Materials and methods

A thin film (120 nm) of titanium dioxide (TiO_2) is deposited onto the D-shaped zone (length of 10 mm) using the ALD technique with the Savannah G2 ALD System from Veeco Inc. Then, the D-shaped zone is partially covered using a mask (adhesive tape). The mask is placed so approximately half of the D-shaped zone is covered (5 mm) and the other half (5 mm) remains uncovered. A tin oxide (SnO_2) coating with a thickness of 20 nm is fabricated onto the D-shaped optical fiber by electron-beam deposition with the Nexdep physical vapor deposition platform from Angstrom Engineering Inc. The directionality of the electron beam deposition guarantees that SnO_2 is not deposited on the part of the D-shaped fiber that is covered.

After the second deposition, the mask is removed, therefore obtaining a nanostructure with a step shaped profile (see detail of **Fig. 3.25)**. The first section has a thickness of 120 nm of TiO_2, as the SnO_2 was deposited over the mask and it has been removed with it. The second section has a total thickness of 140 nm, the first 120 nm of TiO_2 and the remaining 20 nm of SnO_2. A schematic representation of the resulting structure can be observed in **Fig. 3.25**.

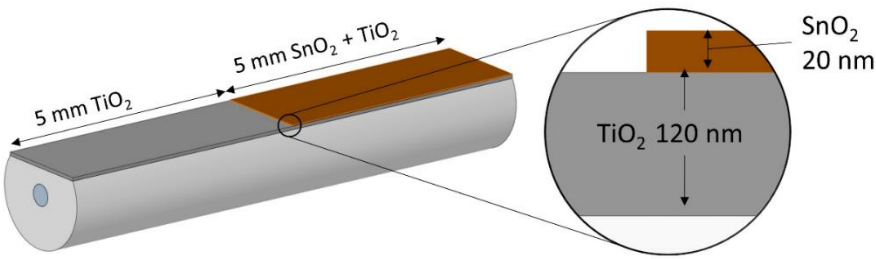

Fig. 3.25 Schematic representation of the obtained step shaped nanostructure with TiO_2 and SnO_2 on the D-shaped fiber. Dimensions are not to scale. Reproduced with permission from [49]. Copyright 2021, Optica Publishing Group.

These thicknesses for both sections were selected with the help of simulations carried out with FIMMWAVE. They were chosen in order to obtain two first order LMR_{TM} (magnetic polarization) close enough so they could be seen in the range of interest but far enough from each other so they did not overlap and could be clearly distinguished.

The refractive index of TiO_2 employed in the theoretical simulations was measured with an ellipsometer UVISEL 2 from Horiba Ltd. (n = 2.619 at 1250 nm, n = 2.16 at

1650 nm) while the extinction coefficient was set to 0.01 to fit the experimental results. It must be considered that the angle of incidence of the ellipsometer required to accurately measure the refractive index does not provide precise results for the extinction coefficient. In the case of SnO_2, a refractive index of 1.9 + 0.01i was used, as in [50], based on ellipsometric measurements performed in [5].

In the measuring setup, one end of the optical fiber is connected to a multi-SLED light source (FJORD-X3-1330-1650 from Pyroistech S.L.) through an in-line polarizer and a polarization controller (Phoenix Photonics Ltd), which enable selecting the TE- or TM-polarized state of light [5]. Once the polarization state has been adjusted, the fiber is fixed so the polarization state does not change. The other end is connected to an optical spectrum analyzer (MS9740A from Anritsu) to observe the resonance while the D-shaped zone is immersed in ultrapure water (18.1 MΩ/cm).

3.4.2. Results

The theoretical results for the previous nanostructure are shown in **Fig. 3.26**. Two first order LMR_{TM} can be observed. The resonance that is located at lower wavelengths (called blue LMR from here on) corresponds to the section with a thickness of 120 nm of TiO_2 whereas the LMR that appears at higher wavelengths (called red LMR from now on) corresponds to the section with a thickness of 140 nm (120 nm TiO_2 + 20 nm SnO_2). For the sake of simplicity, the combination of the blue LMR and the red LMR will be referred as dual LMR.

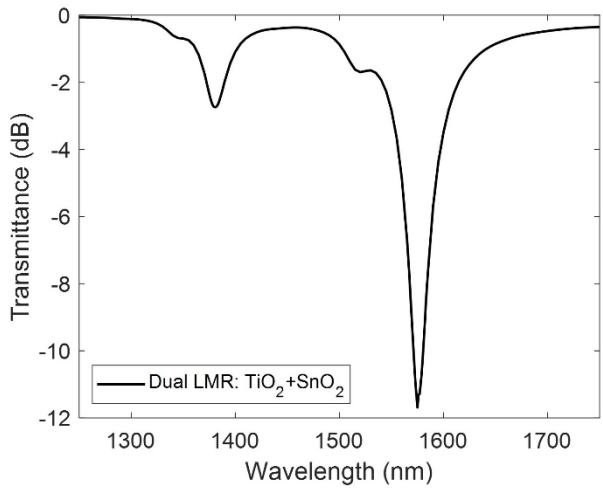

Fig. 3.26. Theoretical results for a dual LMR obtained with a first section 5 mm long with a thickness of 120 nm of TiO_2 and a second section 5 mm long with a thickness of 120 nm of TiO_2 and 20 nm of SnO_2 on a D-shaped SMF. Reproduced with permission from [49]. Copyright 2021, Optica Publishing Group.

The initial LMR (120 nm of TiO_2 over a length of 10 mm) and the final dual LMR can be observed in **Fig. 3.27**, corresponding to the experimental results. The dual LMR resembles the theoretical simulation in **Fig. 3.26**. The appearance of two clearly

distinguishable resonances indicates that the thickness difference between the two sections is far greater than the non-uniformities in each section, also corroborated by the simulations. Regarding the thickness change from one section to the other, no edge effects have been observed - neither experimentally nor theoretically. The tapered ends of the D-shaped region do not have either a high impact in the resonances [50].

In order to demonstrate the independence of both resonances of the dual LMR, each of them is shown separately. To achieve these results, the part of the D-shaped zone that corresponds to each LMR was immersed in ultrapure water while the rest of the device was left in air, obtaining only the desired resonance. It can be observed that the dual LMR is equal to the addition of the blue and red LMRs in **Fig. 3.27**.

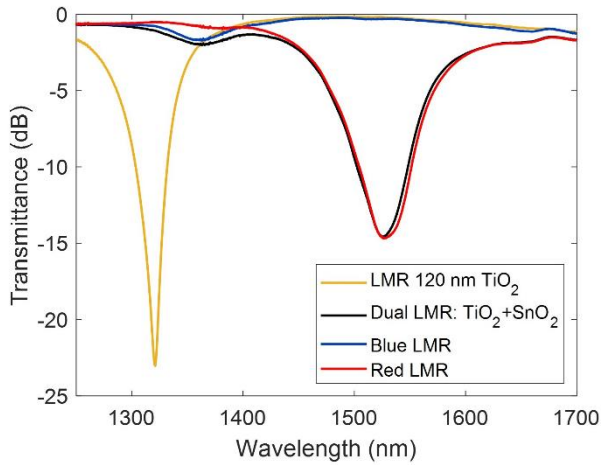

Fig. 3.27 Experimental results for a dual LMR obtained with a first section 5 mm long with a thickness of 120 nm of TiO_2 and a second section 5 mm long with a thickness of 120 nm of TiO_2 and 20 nm of SnO_2 on a D-shaped SMF. Reproduced with permission from [49]. Copyright 2021, Optica Publishing Group.

The blue LMR (corresponding to a 5 mm long section with a thickness of 120 nm of TiO_2) is located next to the initial LMR since both have the same thickness. The slight displacement may be due to oxidation of the material or the deposition of some SnO_2 under the mask. The blue LMR is not as deep as the original LMR with a thickness of 120 nm due to its shorter deposition length (5 mm instead of 10 mm). The red LMR of the final structure has undergone a redshift due to the thicker coating. The red LMR is deeper than the blue LMR, because with the same deposited length, the more the LMR redshifts, the deeper the LMR.

The sensitivity of the device to the SRI for values close to water has also been studied, considering its interest for biosensing applications. The setup is the same as the one that has been previously explained, but in this case the D-shaped region is placed inside a microfluidic system (same one as the one described in subsection 3.3.1), stabilized at 26ºC.

The device response has been monitored with five refractive indices, as it is shown in **Fig. 3.28**. The first refractive index corresponds to ultrapure water and the remaining four correspond to solutions of glucose in ultrapure water with refractive indices of 1.3327, 1.3371, 1.3412, 1.3448 and 1.3485 respectively, measured with refractometer Refracto30GS from Mettler Toledo Inc. The sensitivity values obtained are 4048 nm/refractive index unit (RIU) in the case of the blue LMR and 3914 nm/RIU in the case of the red LMR, with a FOM of 58 RIU^{-1} for the latter resonance. These sensitivities are near the typical values for LMR based sensors, which are around 5000 nm/RIU [40]. It can also be observed the widening of the resonances as they redshift [5].

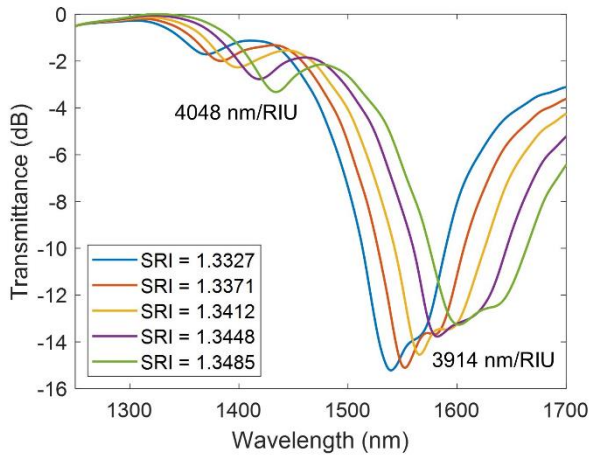

Fig. 3.28 Experimental sensitivity of the blue and the red LMR of the first device as a function of the SRI. Reproduced with permission from [49]. Copyright 2021, Optica Publishing Group.

The operation principle of LMR-based sensors consist of resonance wavelength or maximum power attenuation tracking. Nevertheless, in the previous device, the blue LMR is not very well defined (depth of only -2.0 dB) in comparison with the red LMR (depth of -14.6 dB) which can difficult its monitoring. It would be interesting for this type of devices that both resonances were similar in depth and that they had at least a minimum depth of -5 dB. Here, it has to be considered that the depth of the LMR increases at longer wavelengths and with the length of the D-shaped fiber [11].

Therefore, in order to obtain a twin LMR where the blue and the red LMR have similar depths, it has been decided to modify the length of each section. A new device is manufactured with this purpose. The length of the first section of the D-shaped zone (120 nm thick) is supposed to be around 7.5 mm while the length of the second section (140 nm thick) is approximately 2.5 mm.

Fig. 3.29 shows the theoretical results for different lengths of the two sections. In **Fig. 3.26** it can be appreciated that when both sections measure 5 mm, the theoretical depths of the blue and the red LMR are -2.7 dB and -11.7 dB respectively. However, for the lengths of 7.5 and 2.5 mm, see **Fig. 3.29**, the depths are very similar (-10.7 dB and -9.3 dB respectively), which is the desired result.

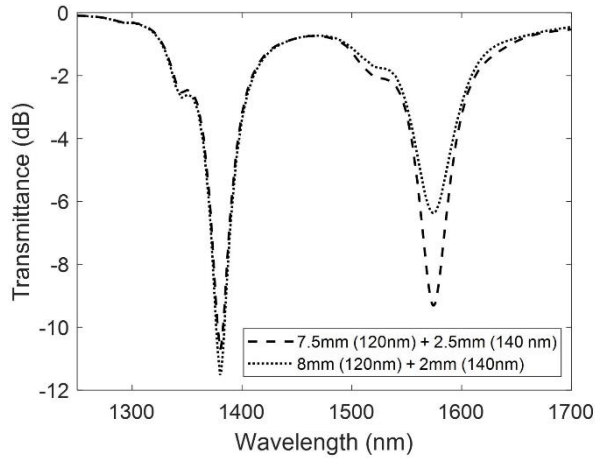

Fig. 3.29 Theoretical results for a dual LMR obtained with different lengths for the first section (thickness of 120 nm of TiO_2) and the second section (thickness of 120 nm of TiO_2 and 20 nm of SnO_2) on a D-shaped SMF. Reproduced with permission from [49]. Copyright 2021, Optica Publishing Group.

In **Fig. 3.30**, the initial LMR and the final twin LMR are shown for this new device. Comparing **Fig. 3.30** with the theoretical simulations in **Fig. 3.29**, it seems that due to technical issues in the fabrication process 8 mm of the D-shaped zone remained covered by the mask while only 2 mm stayed uncovered instead of the initially planned 7.5/2.5 mm proportion. In this case, the blue LMR reaches -13.8 dB while the red LMR achieves -6.3 dB, which is not the result expected to equalize both LMRs but improved considerably the results shown in **Fig. 3.27**.

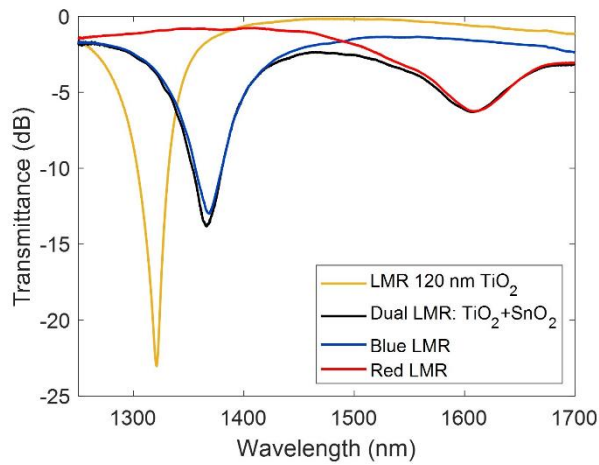

Fig. 3.30 Experimental results for a dual LMR obtained with a first section 8 mm long with a thickness of 120 nm of TiO_2 and a second section 2 mm long with a thickness of 120 nm of TiO_2 and 20 nm of SnO_2 on a D-shaped SMF. Reproduced with permission from [49]. Copyright 2021, Optica Publishing Group.

On the other hand, both the red and blue LMR are shown separately in **Fig. 3.30**, and it can be noted that the twin LMR is the addition of both. It is also worth mentioning that the position of the blue LMR has slightly shifted compared to the position of the initial LMR (120 nm thickness along 10 mm), as it happened in the first device. In this case, the depth of the blue LMR is very similar to the depth of the initial LMR, which is coherent with the fact that most of the D-shaped zone has been covered during the second deposition.

Finally, the sensitivity has also been studied for this second device with the previous five refractive indices, achieving 3977 nm/RIU in the case of the blue LMR and 4506 nm/RIU for the red one, as it can be observed in **Fig. 3.31**. The sensitivity is higher for the resonance located at a longer wavelength, as expected [5]. The FOM is respectively 126 RIU^{-1} for the blue LMR and 35 RIU^{-1} for the red LMR.

This way, two independent LMRs have been obtained on a single optical fiber, having high sensitivities, which improve by more than one order of magnitude the results achieved with the analogous device based on a planar waveguide (sensitivities of 140 nm/RIU and 200 nm/RIU in the 1.3447 - 1.3947 RI range, although they correspond to resonances located at shorter wavelengths [8]); and being equalized in power. Therefore, this device could be employed for the simultaneous and separate detection of multiple analytes in biosensing applications.

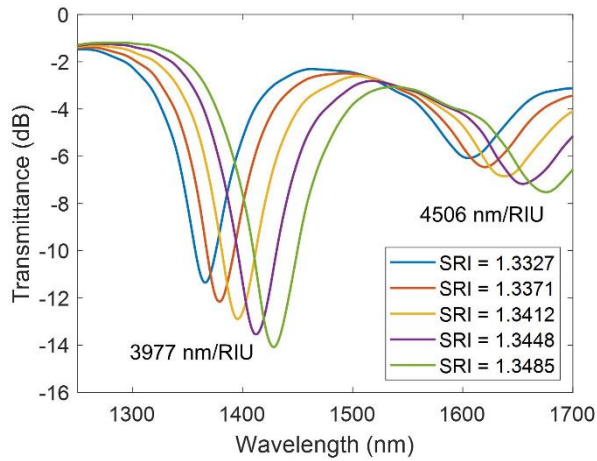

Fig. 3.31 Experimental sensitivity of the blue and the red LMR of the second device for five refractive indices. Reproduced with permission from [49]. Copyright 2021, Optica Publishing Group.

3.5. Conclusions

Different structures and configurations based on LMRs have been studied in this chapter with the purpose of developing sensing platforms that can measure more than one variable at the same time. Their main characteristics and the obtained results are synthesized in **Table 3.8** and described in the following paragraphs.

In the first place, two different thin film patterns deposited on two different substrates (a coverslip and a D-shaped optical fiber) have been theoretically studied. The first design (a pure grating pattern) was expected to generate a LMR associated to the thin film as well as reflection bands associated to the grating pattern, obtaining two different sensing phenomena. It was demonstrated that the position of the reflection bands for different pitches can be predicted with accuracy by adapting the Bragg - Snell law for normal incidence. In the case of the coverslip it was checked that the grating pitch needed to generate an LMR with this structure was too large to produce bands that could be distinguished in the reflection spectrum, so the generation of both types of phenomena with this design was discarded.

The second design consisted of a first section with a homogeneous thickness, that would generate the LMR; and a second section with a grating pattern, which would produce the reflection bands. This design was proven successful in the case of the coverslip, as both type of phenomena were obtained. Nevertheless, the main problem of this structure is that the power of the reflection bands is too low (less than -60 dB). It has still to be studied if increasing the grating length (which led to more powerful reflections bands in the case of the structures based on the D-shaped fiber) could contribute to solve this problem. It has to be considered that, in the case of a practical implementation, increasing the grating length on a planar waveguide would not increase the fragility of the device, as it happens in the case of the D-shaped fiber. In addition, the width, and not only the length of the grating, could also be modified if necessary to improve the performance of the device, a possibility that it is not available in the case of optical fibers and remains to be assessed.

In the case of the D-shaped optical fiber and the first design (pure grating pattern), due to the lessons learned with the coverslip, the attention was completely focused on the reflection bands. Although this was not the original intention, a deep analysis of how to optimize the performance of this structure was carried out. The main part of the analysis was focused on the reflection band located at 1650 nm, for a grating pitch of 4 μm, grating length of 20 mm, and SRI = 1.33 (water).

The reflected power and the FWHM were studied for variations in the thin film thickness, the neck and the length. The first conclusion is that the power increases (achieving values higher than -10 dB) for higher thin film thicknesses (50 nm - 125 nm) and lower necks (- 2 μm - 0 μm) at the cost of widening the FWHM (order of 100 pm). Increasing the length also produces a rise in the reflected power, but in practice it is not realistic to work with lengths greater than 20 mm. The sensitivity to the SRI, the FWHM and the FOM were also studied for variations in the SRI in the 1.33 - 1.4 range. In general, a trade-off between the sensitivity to the SRI and the FWHM is required and it seems the optimum would correspond to a thickness in the 75 nm - 125 nm range and a neck between -2 μm and 0 μm.

The main drawback of this structure is that low values of the neck (at least lower than 3 μm, even lower values, between -2 μm and 0 μm, are needed for optimum performance) are required to achieve an adequate power level of the reflection bands, while the neck value for a standard D-shaped optical fiber is 6.5 μm. Obtaining the desired neck values would require a very precise etching process which, in addition, would make the D-shaped zone more fragile. Another problem that has to be considered for a practical implementation is that the D-shaped section of the fiber would need to be placed perfectly perpendicular to the laser writer in order to manufacture the mask, a task that would be difficult to carry out.

Finally, the second design (homogeneous section and grating section) was simulated on the D-shaped fiber, generating both an LMR in the transmission spectrum and reflection bands, although this structure has not been studied in such great detail as the previous one. The main limitations of this structure are the ones that have already been commented for the previous one.

Regarding the combination of different phenomena an LMR-based refractometer with temperature compensation has been experimentally demonstrated and successfully validated. The proposed device consisted of a D-shaped fiber with an FBG inscribed on its core. In particular, the SRI has been measured in the range from 1.3324 to 1.3479 with a sensitivity of 3725.2 nm/RIU while the temperature varied from 25ºC to 45ºC. The effect of the temperature on the refractometer operation cannot be ignored as it has been calculated that the error can achieve values in the order of 10^{-3} if no correction is performed. In the fields where a precise measurement of the SRI is required, as in the case of gas sensing or biosensing, it is not affordable to make such error.

It must also be remarked that this is the first time that a fully integrated thermo-refractometer consisting of a thin film deposited on a D-shaped optical fiber and an FBG inscribed in its core has been presented. This device could be improved by using an exclusively reflection setup instead of requiring both reflection and transmission interrogation. This can be achieved with an Ag mirror on the tip of the fiber and monitoring the LMR in reflection as in [50]. Furthermore, the proposed device could be miniaturized in a 2 mm long device or even less, as it has been demonstrated that a 2 mm long D-shaped fiber with a nanocoating can generate LMRs for sensing purposes [50], while femtosecond laser technique permits to obtain very short FBGs, on the order of 100 μm [51]. This has special interest in the development of small size probes or the employment of multiple sensors is a small area.

These results also open the door for applications where the LMR shift permits to precisely monitor refractometric changes associated to a single parameter or analyte while the FBG is used to measure a different parameter or analyte, therefore obtaining a totally integrated dual sensor. This concept could be extrapolated to other grating based structures such as TFBGs or LPGs.

Finally, two independent LMRs were obtained in a single D-shaped optical fiber by employing a thin film with two sections of different thickness, a technique that had been previously reported for planar waveguides [6]. Each resonance only shifts when the SRI in which the corresponding section of the D-shaped fiber is immersed in

varies. It was also demonstrated, both theoretically and experimentally, that the depth of each of the resonances of the dual LMR depends on the length of the D-shaped section that generates it. The length of the section with a lower thickness must be greater if it is desired to obtain two resonances with a similar depth. The sensitivity of the fabricated devices was studied, reaching values of ~4000 nm/RIU with a maximum of 4506 nm/RIU for values of the SRI between 1.3327 and 1.3485, which improves by approximately a factor of 20 the results obtained with the analogous device based on a planar waveguide [8].

The developed device could be employed in applications where each resonance was made sensitive to a different parameter or analyte of interest, therefore obtaining multisensing platforms, including biosensors for the detection of several biomarkers. Further improvements of this device would include the generation of more than two resonances by using more thin film sections with different thicknesses (the possibility of obtaining up to nine independent resonances with this method was theoretically shown in the case of a planar waveguide in [6]), leading for instance to the detection of a panel of biomarkers, which has become a tendency in the medical field as it can improve considerably the accuracy in the diagnosis or monitoring of a disease [52–54].

Table 3.8 Main characteristics of the sensors introduced in Chapter 3.

Structure	Max SRI sensitivity (nm/RIU)	SRI range (RIU)	Other features or comments
Grating pattern on a SnO_2 thin film on D-shaped optical fiber	40	1.39 - 1.40	Different parameters (thin film thickness, neck, length, SRI) and their effect on the reflected power, FWHM, FOM have been theoretically studied. A coverslip has also been briefly studied as substrate instead of a D-shaped fiber.
Grating pattern + constant thickness section on a SnO_2 thin film on D-shaped fiber/coverslip	-	-	This thin film pattern is capable of producing both an LMR and reflection bands.
LMR (TiO_2 thin film) + FBG (inscribed on the core) on D-shaped optical fiber	3725.2 (LMR)	1.3324 - 1.3479	The sensor includes temperature compensation by means of the FBG.
Dual LMR on D-shaped optical fiber	4506 (red LMR)	1.3327 - 1.3485	First section of the thin film (TiO_2) is 120 nm thick and the second section (TiO_2 + SnO_2) is 140 nm thick. Different lengths of the sections have been studied.

Bibliography

1. Ozcáriz, A.; Ruiz-Zamarreño, C.; Arregui, F.J. A Comprehensive Review: Materials for the Fabrication of Optical Fiber Refractometers Based on Lossy Mode Resonance. *Sensors* **2020**, *20*, 1972, doi:10.3390/s20071972.

2. Vitoria, I.; Zamarreño, C.R.; Ozcáriz, A.; Matias, I.R. Fiber Optic Gas Sensors Based on Lossy Mode Resonances and Sensing Materials Used Therefor: A Comprehensive Review. *Sensors 2021, Vol. 21, Page 731* **2021**, *21*, 731, doi:10.3390/S21030731.

3. Zamarreño, C.R.; Hernáez, M.; Del Villar, I.; Matias, I.R.; Arregui, F.J. Tunable Humidity Sensor Based on ITO-Coated Optical Fiber. *Sensors and Actuators B* **2010**, *146*, 414–417, doi:10.1016/j.snb.2010.02.029.

4. Zamarreño, C.R.; Hernáez, M.; Del Villar, I.; Matías, I.R.; Arregui, F.J. Optical Fiber PH Sensor Based on Lossy-Mode Resonances by Means of Thin Polymeric Coatings. *Sensors and Actuators B: Chemical* **2011**, *155*, 290–297, doi:10.1016/J.SNB.2010.12.037.

5. Chiavaioli, F.; Zubiate, P.; Del Villar, I.; Zamarreño, C.R.; Giannetti, A.; Tombelli, S.; Trono, C.; Arregui, F.J.; Matias, I.R.; Baldini, F. Femtomolar Detection by Nanocoated Fiber Label-Free Biosensors. *ACS Sensors* **2018**, *3*, 936–943, doi:10.1021/acssensors.7b00918.

6. Dominguez, I.; Del Villar, I.; Fuentes, O.; Corres, J.M.; Matias, I.R. Interdigital Concept in Photonic Sensors Based on an Array of Lossy Mode Resonances. *Scientific Reports 2021 11:1* **2021**, *11*, 1–11, doi:10.1038/s41598-021-92765-0.

7. Fuentes, O.; Corres, J.M.; Dominguez, I.; Del Villar, I.; Matias, I.R. Simultaneous Measurement of Refractive Index and Temperature Using LMR on Planar Waveguide. In Proceedings of the Proceedings of IEEE Sensors; Institute of Electrical and Electronics Engineers Inc., October 25 2020; Vol. 2020-October.

8. Dominguez, I.; Corres, J.M.; Fuentes, O.; Del Villar, I.; Matias, I.R. Multichannel Refractometer Based on Lossy Mode Resonances. *IEEE Sensors Journal* **2022**, *22*, 3181–3187, doi:10.1109/JSEN.2022.3142050.

9. Dominguez, I.; Del Villar, I.; Fuentes, O.; Corres, J.M.; Matias, I.R. Dually Nanocoated Planar Waveguides towards Multi-Parameter Sensing. *Scientific Reports 2021 11:1* **2021**, *11*, 1–8, doi:10.1038/s41598-021-83324-8.

10. Del Villar, I.; Arregui, F.J.; Zamarreño, C.R.; Corres, J.M.; Bariain, C.; Goicoechea, J.; Elosua, C.; Hernaez, M.; Rivero, P.J.; Socorro, A.B.; et al. Optical Sensors Based on Lossy-Mode Resonances. *Sensors and Actuators B: Chemical* **2017**, *240*, 174–185, doi:10.1016/J.SNB.2016.08.126.

11. Arregui, F.J.; Del Villar, I.; Zamarreño, C.R.; Zubiate, P.; Matias, I.R. Giant Sensitivity of Optical Fiber Sensors by Means of Lossy Mode Resonance. *Sensors and Actuators, B: Chemical* **2016**, *232*, 660–665, doi:10.1016/j.snb.2016.04.015.

12. Ozcariz, A.; Zamarreño, C.R.; Zubiate, P.; Arregui, F.J. Is There a Frontier in Sensitivity with Lossy Mode Resonance (LMR) Based Refractometers? *Scientific Reports* **2017**, *7*, 1–7, doi:10.1038/s41598-017-11145-9.

13. Tien, C.L.; Lin, H.Y.; Su, S.H. High Sensitivity Refractive Index Sensor by D-Shaped Fibers and Titanium Dioxide Nanofilm. *Advances in Condensed Matter Physics* **2018**, *2018*, doi:10.1155/2018/2303740.

14. Beysens, D.; Calmettes, P. Temperature Dependence of the Refractive Indices of Liquids: Deviation from the Lorentz–Lorenz Formula. *The Journal of Chemical Physics* **1977**, *66*, 766, doi:10.1063/1.433954.

15. Alwis, L.; Sun, T.; Grattan, K.T.V. Optical Fibre Refractive Index Sensor in a Hybrid Fibre Grating Configuration. *Procedia Engineering* **2015**, *120*, 11–14, doi:10.1016/J.PROENG.2015.08.555.

16. Zhu, C.; Alla, D.; Huang, J.; Huang, J.; Huang, J. High-Temperature Stable FBGs Fabricated by a Point-by-Point Femtosecond Laser Inscription for Multi-Parameter Sensing. *OSA Continuum, Vol. 4, Issue 2, pp. 355-363* **2021**, *4*, 355–363, doi:10.1364/OSAC.415685.

17. Yang, K.; Liu, B.; Liao, C.; Wang, Y.; Cai, Z.; Tang, J.; Yang, Y.; Wang, Y. Highly Localized Point-by-Point Fiber Bragg Grating for Multi-Parameter Measurement. *Journal of Lightwave Technology* **2021**, *39*, 6686–6690, doi:10.1109/JLT.2021.3104102.

18. Fan, X.; Jiang, J.; Zhang, X.; Liu, K.; Wang, S.; Liu, T. Simultaneous Measurement of Refractive Index and Temperature Using a Hybrid-Grating Sensor. *Applied Physics Express* **2019**, *12*, 116501, doi:10.7567/1882-0786/AB4407.

19. Shao, L.-Y.; Shevchenko, Y.; Albert, J. Intrinsic Temperature Sensitivity of Tilted Fiber Bragg Grating Based Surface Plasmon Resonance Sensors. *Optics Express* **2010**, *18*, 11464, doi:10.1364/oe.18.011464.

20. Chan, C.F.; Chen, G.; Jafari, A.; Laronche, A.; Thomson, D.J.; Albert, J. Optical Fiber Refractometer Using Narrowband Cladding-Mode Resonance Shifts. *Applied Optics, Vol. 46, Issue 7, pp. 1142-1149* **2007**, *46*, 1142–1149, doi:10.1364/AO.46.001142.

21. Mandia, D.J.; Albert, J.; Barry, S.T.; Zhou, W. Absolute Near-Infrared Refractometry with a Calibrated Tilted Fiber Bragg Grating. *Optics Letters, Vol. 40, Issue 8, pp. 1713-1716* **2015**, *40*, 1713–1716, doi:10.1364/OL.40.001713.

22. Urrutia, A.; Del Villar, I.; Zubiate, P.; Zamarreño, C.R. A Comprehensive Review of Optical Fiber Refractometers: Toward a Standard Comparative Criterion. *Laser & Photonics Reviews* **2019**, *13*, 1900094, doi:10.1002/lpor.201900094.

23. Del Villar, I.; Hernaez, M.; Zamarreño, C.R.; Sánchez, P.; Fernández-Valdivielso, C.; Arregui, F.J.; Matias, I.R. Design Rules for Lossy Mode Resonance Based Sensors. *Applied Optics* **2012**, *51*, 4298–4307, doi:10.1364/AO.51.004298.

24. Imas, J.J.; Zamarreño, C.R.; Del Villar, I.; Matías, I.R. Optimization of Fiber Bragg Gratings Inscribed in Thin Films Deposited on D-Shaped Optical Fibers. *Sensors 2021, Vol. 21, Page 4056* **2021**, *21*, 4056, doi:10.3390/S21124056.

25. Sanchez, P.; Zamarreño, C.R.; Hernaez, M.; Matias, I.R.; Arregui, F.J. Optical Fiber Refractometers Based on Lossy Mode Resonances by Means of SnO2 Sputtered Coatings. *Sensors and Actuators, B: Chemical* **2014**, *202*, 154–159, doi:10.1016/j.snb.2014.05.065.

26. Ascorbe, J.; Corres, J.M.; Del Villar, I.; Arregui, F.J.; Matias, I.R. Fabrication of Bragg Gratings on the End Facet of Standard Optical Fibers by Sputtering the Same Material. *Journal of Lightwave Technology* **2017**, *35*, 212–219, doi:10.1109/JLT.2016.2640021.

27. Gallego, E.E.; Ascorbe, J.; Del Villar, I.; Corres, J.M.; Matias, I.R. Nanofabrication of Phase-Shifted Bragg Gratings on the End Facet of Multimode Fiber towards Development of Optical Filters and Sensors. *Optics & Laser Technology* **2018**, *101*, 49–56, doi:10.1016/J.OPTLASTEC.2017.11.001.

28. Pavlichenko, I.; Exner, A.T.; Guehl, M.; Lugli, P.; Scarpa, G.; Lotsch, B. V. Humidity-Enhanced Thermally Tunable TiO 2/SiO 2 Bragg Stacks. *Journal of Physical Chemistry C* **2012**, *116*, 298–305, doi:10.1021/jp208733t.

29. Wilkens, V.; Koch, C.; Molkenstruck, W. Frequency Response of a Fiber-Optic Dielectric Multilayer Hydrophone. *Proceedings of the IEEE Ultrasonics Symposium* **2000**, *2*, 1113–1116, doi:10.1109/ULTSYM.2000.921520.

30. Poxson, D.J.; Schubert, E.F.; Mont, F.W.; Kim, J.K.; Schubert, M.F.; Chhajed, S. Design of Multilayer Antireflection Coatings Made from Co-Sputtered and Low-Refractive-Index Materials by Genetic Algorithm. *Optics Express, Vol. 16, Issue 8, pp. 5290-5298* **2008**, *16*, 5290–5298, doi:10.1364/OE.16.005290.

31. Arregui, F.J.; Matias, I.R.; Cooper, K.L.; Claus, R.O. Fabrication of Micrograting on the Ends of Standard Optical Fibers by the Electrostatic Self-Assembly Monolayer Process. *Optics Letters, Vol. 26, Issue 3, pp. 131-133* **2001**, *26*, 131–133, doi:10.1364/OL.26.000131.

32. Malitson, I.H. Interspecimen Comparison of the Refractive Index of Fused Silica. *J Opt Soc Am* **1965**, *55*, 1205, doi:10.1364/josa.55.001205.

33. Rubin, M. Optical Properties of Soda Lime Silica Glasses. *Solar Energy Materials* **1985**, *12*, 275–288, doi:10.1016/0165-1633(85)90052-8.

34. Sultanova, N.; Kasarova, S.; Nikolov, I. Dispersion Properties of Optical Polymers. *Acta Physica Polonica A* **2009**, *116*, 585–587, doi:10.12693/APHYSPOLA.116.585.

35. Burnat, D.; Koba, M.; Wachnicki, Ł.; Gierałtowska, S.; Godlewski, M.; Śmietana, M. Refractive Index Sensitivity of Optical Fiber Lossy-Mode Resonance Sensors Based on Atomic Layer Deposited TiO x Thin Overlay . In Proceedings of the Sixth European Workshop on Optical Fibre Sensors; SPIE, May 30 2016; Vol. 9916, p. 99161G.

36. Del Villar, I.; Matías, I.R.; Arregui, F.J.; Lalanne, P. Optimization of Sensitivity in Long Period Fiber Gratings with Overlay Deposition. *Optics Express* **2005**, *13*, 56, doi:10.1364/opex.13.000056.

37. Cusano, A.; Iadicicco, A.; Pilla, P.; Contessa, L.; Campopiano, S.; Cutolo, A.; Giordano, M. Mode Transition in High Refractive Index Coated Long Period Gratings. *Optics Express* **2006**, *14*, 19, doi:10.1364/opex.14.000019.

38. Del Villar, I.; Cruz, J.L.; Socorro, A.B.; Corres, J.M.; Matias, I.R. Sensitivity Optimization with Cladding-Etched Long Period Fiber Gratings at the Dispersion Turning Point. *Optics Express* **2016**, *24*, 17680, doi:10.1364/oe.24.017680.

39. Imas, J.J.; Zamarreño, C.R.; Del Villar, I.; Da Silva, J.C.C.; Oliveira, V.; Matías, I.R. Optical Fiber Thermo-Refractometer. *Optics Express, Vol. 30, Issue 7, pp. 11036-11045* **2022**, *30*, 11036–11045, doi:10.1364/OE.450316.

40. Zubiate, P.; Urrutia, A.; Zamarreño, C.R.; Egea-Urra, J.; Fernández-Irigoyen, J.; Giannetti, A.; Baldini, F.; Díaz, S.; Matias, I.R.; Arregui, F.J.; et al. Fiber-Based Early Diagnosis of Venous Thromboembolic Disease by Label-Free D-Dimer Detection. *Biosensors and Bioelectronics: X* **2019**, *2*, 100026, doi:10.1016/j.biosx.2019.100026.

41. Othonos, A. Fiber Bragg Gratings. *Review of Scientific Instruments* **1998**, *68*, 4309, doi:10.1063/1.1148392.

42. Bashkatov, A.N.; Genina, E.A. Water Refractive Index in Dependence on Temperature and Wavelength: A Simple Approximation. In Proceedings of the Proceedings Volume 5068, Saratov Fall Meeting 2002: Optical Technologies in Biophysics and Medicine IV; SPIE, October 13 2003; Vol. 5068, pp. 393–395.

43. Liu, L.; Liu, Z.; Zhang, Y.; Liu, S. Side-Polished D-Type Fiber SPR Sensor for RI Sensing with Temperature Compensation. *IEEE Sensors Journal* **2021**, *21*, 16621–16628, doi:10.1109/JSEN.2021.3080290.

44. Fuentes, O.; Corres, J.M.; Dominguez, I.; Del Villar, I.; Matias, I.R. Lossy Mode Resonances Generated in Planar Configuration for Two-Parameter Sensing. *IEEE Sensors Journal* **2021**, doi:10.1109/JSEN.2021.3076557.

45. Wang, Q.; Jing, J.Y.; Wang, X.Z.; Niu, L.Y.; Zhao, W.M. A D-Shaped Fiber Long-Range Surface Plasmon Resonance Sensor with High Q-Factor and Temperature Self-Compensation. *IEEE Transactions on Instrumentation and Measurement* **2020**, *69*, 2218–2224, doi:10.1109/TIM.2019.2920187.

46. Zubiate, P.; Zamarreño, C.R.; Del Villar, I.; Matias, I.R.; Arregui, F.J. High Sensitive Refractometers Based on Lossy Mode Resonances (LMRs) Supported by ITO Coated D-Shaped Optical Fibers. *Optics Express* **2015**, *23*, 8045, doi:10.1364/oe.23.008045.

47. Cao, S.; Shao, Y.; Wang, Y.; Zhang, L.; Huang, Y.; Zhang, F.; Liao, C.; Wang, Y.; Sreekanth, K. V; Alapan, Y.; et al. Highly Sensitive Surface Plasmon Resonance Biosensor Based on a Low-Index Polymer Optical Fiber. *Optics Express, Vol. 26, Issue 4, pp. 3988-3994* **2018**, *26*, 3988–3994, doi:10.1364/OE.26.003988.

48. Kaźmierczak, A.; Carlborg, C.F.; Barrios, C.A.; Dortu, F.; Stemme, G.; Sohlström, H.; Gylfason, K.B.; Vivien, L.; Wijngaart, W. van der On-Chip Temperature Compensation in an Integrated Slot-Waveguide Ring Resonator Refractive Index Sensor Array. *Optics Express, Vol. 18, Issue 4, pp. 3226-3237* **2010**, *18*, 3226–3237, doi:10.1364/OE.18.003226.

49. Imas, J.J.; Zamarreño, C.R.; Zubiate, P.; Del Villar, I.; Pérez-Escudero, J.M.; Matías, I.R. Twin Lossy Mode Resonance on a Single D-Shaped Optical Fiber. *Optics Letters, Vol. 46, Issue 13, pp. 3284-3287* **2021**, *46*, 3284–3287, doi:10.1364/OL.425928.

50. Fuentes, O.; Vaiano, P.; Del Villar, I.; Quero, G.; Corres, J.; Consales, M.; Matías, I.; Cusano, A. Improving the Width of Lossy Mode Resonances in a Reflection Configuration D-Shaped Fiber by Nanocoating Laser Ablation. *Optics Letters* **2020**, *45*, 4738, doi:10.1364/ol.402177.

51. Hnatovsky, C.; Grobnic, D.; Mihailov, S.J. Through-the-Coating Femtosecond Laser Inscription of Very Short Fiber Bragg Gratings for Acoustic and High Temperature Sensing Applications. *Optics Express, Vol. 25, Issue 21, pp. 25435-25446* **2017**, *25*, 25435–25446, doi:10.1364/OE.25.025435.

52. Muinao, T.; Deka Boruah, H.P.; Pal, M. Multi-Biomarker Panel Signature as the Key to Diagnosis of Ovarian Cancer. *Heliyon* 2019, *5*, e02826.

53. Nozaki, T.; Sugiyama, S.; Koga, H.; Sugamura, K.; Ohba, K.; Matsuzawa, Y.; Sumida, H.; Matsui, K.; Jinnouchi, H.; Ogawa, H. Significance of a Multiple Biomarkers Strategy Including Endothelial Dysfunction to Improve Risk Stratification for Cardiovascular Events in Patients at High Risk for Coronary Heart Disease. *J Am Coll Cardiol* **2009**, *54*, 601–608, doi:10.1016/j.jacc.2009.05.022.

54. Shariat, S.F.; Karakiewicz, P.I.; Ashfaq, R.; Lerner, S.P.; Palapattu, G.S.; Cote, R.J.; Sagalowsky, A.I.; Lotan, Y. Multiple Biomarkers Improve Prediction of Bladder Cancer Recurrence and Mortality in Patients Undergoing Cystectomy. *Cancer* **2008**, *112*, 315–325, doi:10.1002/cncr.23162.

Chapter 4

Mode Transition Enhancement in Optical Fiber Gratings

4.1. Introduction

The term mode transition was first introduced in [1], although this phenomenon was previously observed in [2]. In this work, a thin film with a higher refractive index than that of the cladding was deposited on an optical fiber with a LPG written on its core, producing a wavelength shift and an amplitude change of the attenuation bands as a function of its thickness.

It was later demonstrated that the wavelength shift is caused by the gradual transfer of energy from a cladding mode to a leaky mode of the thin film as it becomes thick enough to support one, causing a reorganization of the cladding modes. Each cladding mode '*i*' shifts its effective refractive index value towards the effective index of the immediate lower order cladding mode '*i-1*' [3,4]. The range of thicknesses where this effect takes place is also connected with an apparent fiber mode loss (a decrease of the amplitude of the grating resonance) since the power transfer from the fiber core to the coating reduces the power density in the fiber core and consequently the coupling coefficient of the grating. The term "Lossy Mode Resonance" (LMR) can be used to describe such effects [5].

Furthermore, the fast shift of the cladding modes effective index in this region leads to an increase in the sensitivity of the attenuation bands (both are linked through the phase matching equation), which was demonstrated in [4]. Nevertheless, the first works on this phenomenon had to face the problem that the resonances faded during the transition because the deposition techniques employed (Langmuir Blodgett and Layer by Layer self-assembly) produced coatings with strong losses [2,3]. This obstacle was solved by using the dip coating technique, which provided higher quality films, demonstrating the applicability for sensing [6], and since then, the mode transition phenomenon has been employed in a large number of refractive index sensing [7,8], chemical [9] and biosensing [10] applications.

However, there is still room for improvement regarding the mode transition phenomena. In [11], the mode transition was theoretically studied for LPGs including an intermediate low refractive index (RI) layer acting as a second cladding between the cladding of the LPG and a high RI film, in which can be considered a double-clad LPG. It was observed that the mode transition obtained with this structure was more abrupt than the one achieved with a standard LPG with a high RI thin film, therefore providing a higher sensitivity. Furthermore, the sensitivity could be controlled through the thickness of the second cladding. This enhanced mode transition received the name of mode tunneling, in analogy to the tunnel effect observed in electronics. Here, the second cladding acts as a barrier for the guidance of the cladding mode in the thin film. Finally, the cladding mode can be guided in the thin film by tunneling the narrow thickness of the low RI region. Nevertheless, experimental evidence of this phenomenon has not yet been demonstrated, but it must be pointed out that the experiment is extremely challenging.

It must be mentioned that the mode transition has been demonstrated in double-clad fibers [10,12], although the configuration is completely different from the one proposed in the previous paragraph. In [12], a LPG inscribed in a fiber with a W-type RI profile was employed for the first time, that is, the refractive index of the second cladding is higher than that of the first cladding; and no thin film is deposited. It can be noted that the number of layers and the RI profile is the same as in the case of the standard LPG with a high RI thin film, although in this work the mode transition is achieved by etching the second cladding instead of by depositing a thin film.

In consequence, there is still no experimental study about the mode transition obtained through the deposition of a high RI thin film on a double-clad fiber where the refractive index of the second cladding is lower than that of the first cladding. The first part of this chapter will be dedicated to performing this analysis. In the first place, fibers with different second cladding thicknesses will be obtained by means of etching. The final thickness will be controlled through the wavelength shift during the etching process. Then, the mode transition obtained through the deposition of a high RI thin film will be studied for these fibers, assessing the impact of the second cladding thickness on the sensitivity to the thin film thickness. Finally, the sensitivity to the surrounding medium refractive index (SRI) in the 1.33 - 1.47 range will be analyzed for fibers working at the mode transition with different second cladding thicknesses.

On the other hand, the mode transition phenomenon has also been observed in single-mode multimode single-mode (SMS) structures, but these provide only differential thickness information as they are based on mode interferometry [13]. Another sensor technology based on tilted fiber Bragg gratings (TFBGs) is widely used in applications involving the fabrication of nanoscale functional coatings [14–17]. While mode transitions on TFBGs with a high RI coating (indium tin oxide - ITO) have been predicted and analyzed theoretically, no experimental evidence has provided [18].

Therefore, the second part of this chapter will be focused on studying the mode transition both theoretically and experimentally on TFBGs. Several materials (indium tin oxide, ITO; and titanium dioxide, TiO_2) and deposition methods (sputtering, atomic layer deposition) will be employed. Both polarization states (P-polarization, corresponding to EH modes; and S-polarization, corresponding to HE modes) will be studied during the mode transition. Finally, the mode transition will be applied to calculate the thickness of a thin film deposited on a TFBG considering that the refractive index of the thin film material is known.

4.2. Mode transition in double-clad LPGs

4.2.1. Materials and methods

The LPGs that were employed in this work were manufactured by the Laboratory of Fiber Optics of the University of Valencia. The LPGs were inscribed in hydrogen-loaded double-clad fibers SMM900 from Fibercore with a grating period of 176 μm. These fibers had the following characteristics: first cladding with a diameter of 102 μm and numerical aperture equal to 0.18, second cladding with a diameter of 124.7 μm and numerical aperture equal to 0.24, cut-off wavelength at 895 nm and modal field diameter of the core mode of 7.8 μm. The gratings were photo-inscribed with the point by point technique with a doubled argon laser and then stored for 240 hours to allow the out-diffusion of the remaining hydrogen and hence the grating stabilization

Six fibers with the previously described characteristics were manufactured. Four were utilized in the analysis of the sensitivity to the thin film thickness while two were employed in the refractive index sensitivity analysis. **Fig. 4.1a** shows a schematic representation of the employed optical fibers where the four layers (core, first and second cladding and thin film) can be distinguished. The second cladding is a key point for the increase in sensitivity on the basis of the field enhancement induced by the presence of this layer in the transition mode region. The relationships between the real part of the refractive indices (*n*) of the four layers are represented in **Fig. 4.1b**.

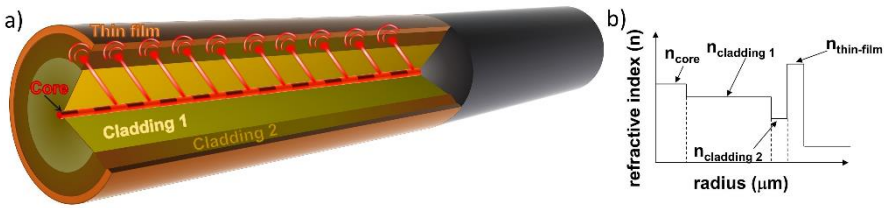

Fig. 4.1 a) Schematic representation of the optical fibers that are employed in this work, with a four-layer structure with core, two claddings and a thin film. b) Schematic diagram of the relationships between the real part of the refractive indices (*n*) of the four layers (not to scale).

Regarding the etching process, a 30-mm-long segment including the photo-inscribed part of the LPG was introduced into a plastic cuvette [19]. The cuvette was filled with 25% (v/v) hydrofluoric acid (HF) solution from Panreac. This concentration enabled a slow and uniform etching process at a rate of 0.7 μm/min in the region of interest. The thicknesses of the fibers after etching were measured with a Leica DM2500M microscope equipped with a Leica DMC2900 camera, both from Leica Microsystems.

With respect to the depositions, the atomic layer deposition method (Savannah G2 ALD System from Veeco Inc) was employed, using ultrapure water and tetrakis(dimethylamido) titanium(IV) (669008, Sigma-Aldrich) as precursors and performing the deposition at a constant temperature of 100ºC. During the deposition, one end of the fiber was connected to a multi-SLD source (FJORD-X3, Pyroistech

S.L.) while the other end was connected to an optical spectrum analyzer (HP-86142A from Agilent), see **Fig. 4.2**. The ALD system was used with the dome lid. This lid counts with a pass through hole, sealed with resin, that allows two fibers to go inside the chamber, one for the input light and the other for the output light, enabling the deposition monitoring.

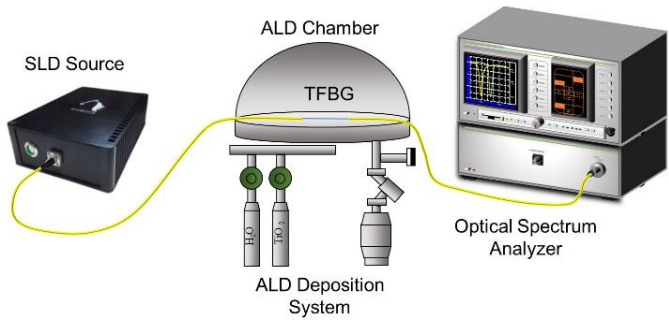

Fig. 4.2 Schematic of the setup used for monitoring the LPGs deposition in the ALD system.

The two LPGs designed for the RI sensitivity analysis were immersed in glycerol solutions with RI values ranging from 1.33 to 1.47. The RI of the solutions was characterized with a commercial refractometer (Mettler Toledo® Refracto 30GS) operating at a wavelength of 589 nm with a precision of 0.001.

An ellipsometer (UVISEL 2, Horiba Scientific Thin Film Division) with a spectral range of 0.6–6.5 eV (190–2100 nm), an angle of incidence of 70º, a spot size of 1 mm and software DeltaPsi2™ (from Horiba Scientific Thin Film Division) was used to characterize the thickness, the real part of the refractive index (n) and the imaginary part of the refractive index or extinction coefficient (k) of the deposited thin films. The analyzed samples were pieces of silicon wafers that were placed next to the TFBGs inside the sputtering or ALD chamber during the depositions.

The modal fields and the effective indices of the modes in each section of the LPG were calculated by the finite difference method (FDM) using FIMMWAVE® (Photon Design Inc.), as this is the most accurate method for a cylindrical waveguide simulation. On this basis, the transmission spectra were calculated with FIMMPROP, a module integrated within FIMMWAVE. For the input and output sections of the fiber, only the core mode was simulated, whereas in the grating region both the core mode and up to 14 other modes were calculated in order to include the highest-order mode responsible for the resonances observed in the transmission spectra. Each period consisted of two segments of different RI, implementing in this way a square-wave profile, which resembled the experimental profile, where a point-by-point technique based on the displacement of the laser and passing the light through a slit permitted the generation of a quasi-square-wave profile with a 50% duty cycle. The peak-to-peak modulation in the grating region that best fitted the experimental results was 0.001. The model for SiO_2 was obtained from [20] and the real part (n) and the imaginary part (k) of the refractive index of TiO_2 employed in the simulations were taken from the ellipsometry measurements (n varies from 2.44 to 2.47 in the studied wavelength range, 1250 - 1550 nm, and $k = 0$ in all the considered range).

4.2.2. Results

4.2.2.1. Control of second-cladding thickness by etching

In order to verify the hypothesis that the thickness of the second cladding controls the further sensitivity of the device in the mode transition region, four LPGs with the same characteristics were manufactured and each of them was subjected to an etching process. The final thickness of the second cladding can be controlled through the duration of this etching process. Regarding the modes, the notation will be the following: $HE_{1,1}$ for the core mode; $HE_{1,2}$ for the first $HE_{1,x}$ cladding mode, $HE_{1,4}$ for the second $HE_{1,x}$ cladding mode, and so on; and $EH_{1,3}$ for the first $EH_{1,x}$ cladding mode, $EH_{1,5}$ for the second $EH_{1,x}$ cladding mode, and so on.

The experimental spectrum of one of the employed LPGs is shown in **Fig. 4.3**. The experiments will be focused on the resonance that is located at longer wavelengths in this spectrum, which corresponds to cladding mode $HE_{1,14}$. The simulated wavelength shift of this resonance as a function of the second cladding thickness is shown in **Fig. 4.4**. The x-axis covers up to a thickness of 11.35 μm, which is the initial thickness of the second cladding before etching.

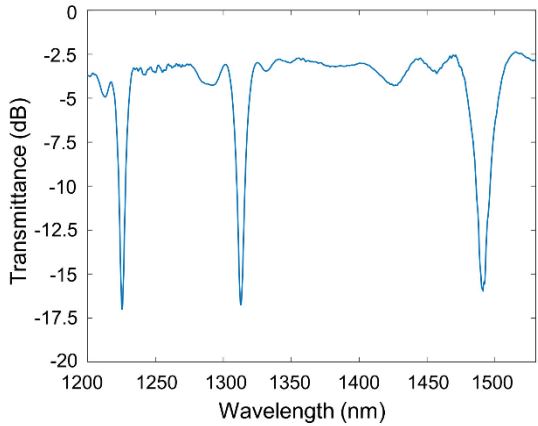

Fig. 4.3. Experimental spectrum of one of the employed double clad LPGs.

LPGs 1, 2, 3 and 4 experienced a wavelength shift of 7, 11 nm, 18 and 50 nm, respectively, as a result of the etching process. The experimental points (second cladding thickness, central wavelength of the resonance) corresponding to these LPGs, as well as the simulated ones, are plotted in as red squares and blue circles, respectively. If the wavelength shift is higher than 36 nm, it means that the second cladding has been completely removed. The different experimental and numerical values are summarized in **Table 4.1**. It has to be noted that in LPG4 the second cladding was completely etched and part of the first cladding was etched too.

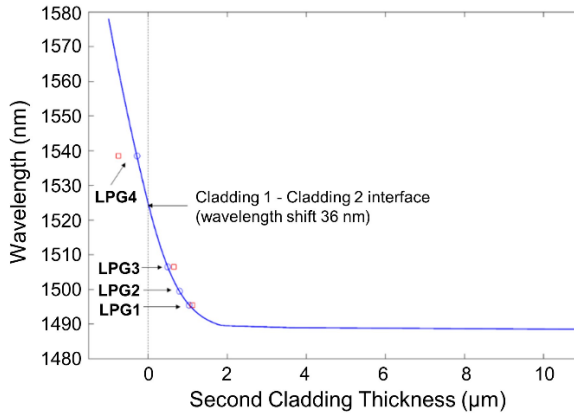

Fig. 4.4 Wavelength shift of the $HE_{1,14}$ resonance as a function of the second-cladding thickness. The blue circles indicate the theoretical diameters for LPGs 1-4 and the red squares correspond to the experimental values for LPG1,3,4 (this value is not available for LPG2).

Table 4.1 Parameters of the etched LPGs

	Wavelength shift (nm)	**Fiber Ø experimental (μm)**	**Fiber Ø numerical (μm)**	**Ø cladding 1 numerical (μm)**	**Thickness cladding 2 numerical (μm)**
LPG 1	7	104.25	104.12	102	1.06
LPG 2	11	-	103.58	102	0.79
LPG 3	18	103.31	102.96	102	0.48
LPG 4	50	100.49	101.44	101.44	0

4.2.2.2. Atomic layer deposition and sensitivity to thickness

Before carrying out the depositions, the evolution of the effective indices of the cladding modes as a function of the TiO_2 coating thickness is analyzed theoretically at a wavelength of 1450 nm for different thicknesses of the second cladding (no cladding, 0.49, 0.79 and 1.06 μm), which correspond to LPGs 1-4. The results are shown in **Fig. 4.5** and the conclusion is that when the second-cladding thickness increases, the mode transition generated when one of the cladding modes is guided in the thin film is more abrupt and happens at a slightly higher thickness.

This phenomenon has an immediate effect in the evolution of the resonances as a function of the thin film thickness, since the effective index of each cladding mode and the wavelength of its corresponding attenuation band is given by the phase matching condition [21]:

$$\lambda = \left(n_{core}(\lambda) - n^{i}_{cladding}(\lambda)\right) \cdot \Lambda \qquad (4.1)$$

where $n_{core}(\lambda)$ is the effective refractive index of the core mode at λ, $n^{i}_{cladding}(\lambda)$ is the effective refractive index of the ith cladding mode at λ, and Λ is the grating period.

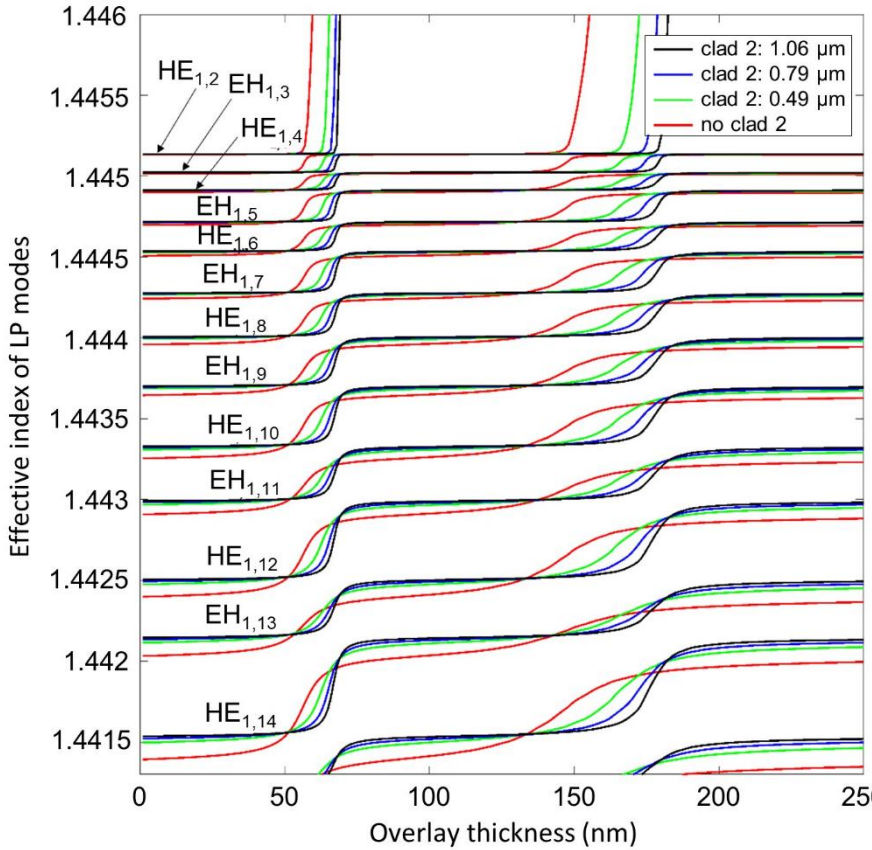

Fig. 4.5 Effective indices of $HE_{1,x}$ and $EH_{1,x}$ modes as a function of the TiO_2 thin-film thickness for LPG1 (cladding 2 thickness of 1.06 μm), LPG2 (0.79 μm), LPG3 (0.49 μm) and LPG4 (no cladding 2). The sensitivity to the thin film thickness increases with the thickness of the second cladding.

In order to verify this relationship, the four LPGs were deposited with TiO_2 employing the ALD system and the transmission spectra were registered during the deposition process. **Fig. 4.6** shows both the experimental results (on the left) and the corresponding simulations (on the right) for each LPG. The final thicknesses were measured with the ellipsometer in silicon wafer samples deposited in close proximity to each LPG. These thicknesses are the ones used in the simulations and they enable the conversion of the experimental times into thicknesses assuming a constant deposition rate. The experimental and theoretical results for the wavelength shifts of the resonances (yellow bands) shown in **Fig. 4.6** present the same tendency as that observed for the effective indices of the cladding modes in **Fig. 4.5**. For a thicker second cladding, the wavelength shifts in the resonances are more abrupt, that is, the sensitivity to the thin film thickness increases.

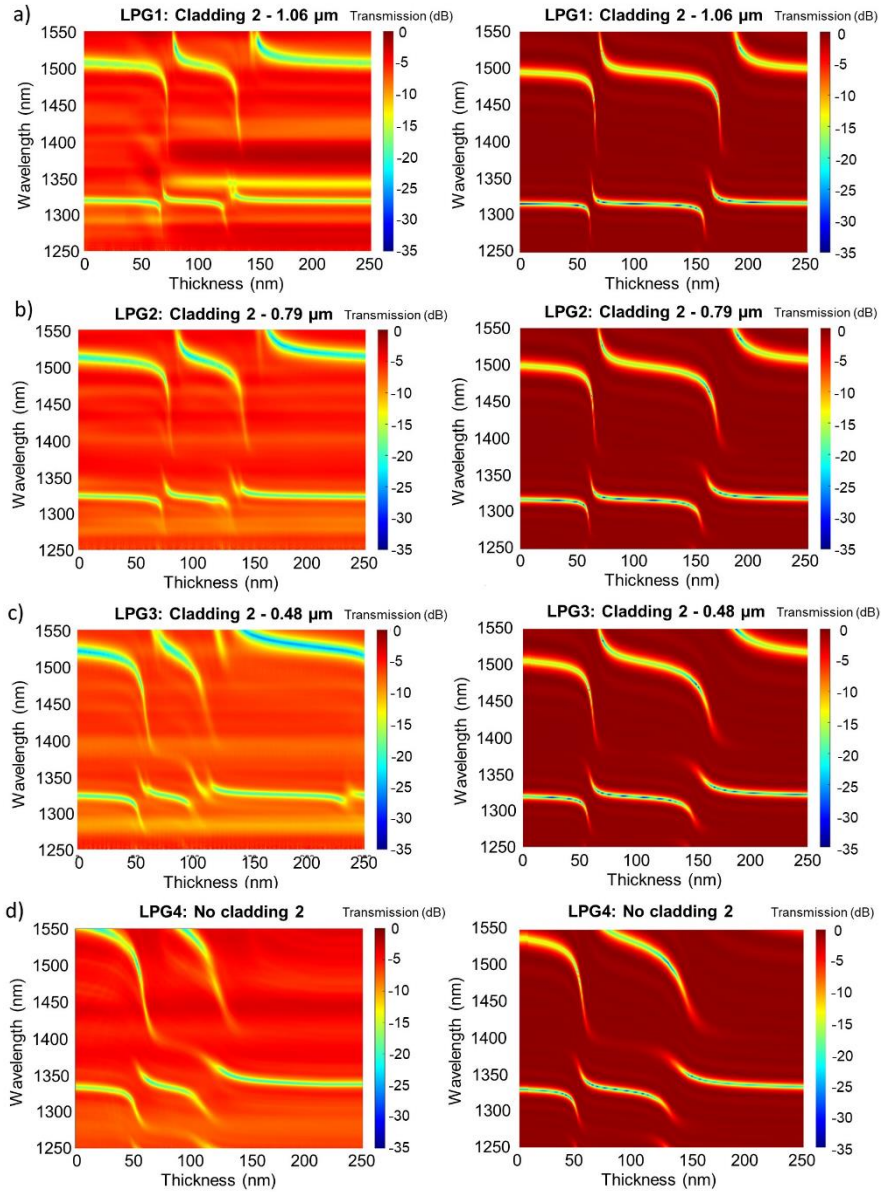

Fig. 4.6 Experimental (left) and numerical (right) results of the wavelength shift in the attenuation bands due to the transitions of the cladding modes with the TiO_2 thin-film thickness. a) LPG1: Cladding 2, 1.06 µm b) LPG2: Cladding 2, 0.79 µm c) LPG3: Cladding 2, 0.48 µm. d) LPG4: No cladding 2, and Cladding 1 etched 0.28 µm.

However, it is also important to remark that the increase in sensitivity is not unlimited. **Fig. 4.7a** shows the wavelength shift of the $HE_{1,14}$ band (the one initially

located around 1500 nm before the deposition) as a function of the TiO_2 thin film thickness for LPGs 1-4, both experimental and theoretical, extracted from **Fig. 4.6**. The more abrupt wavelength shift for a thicker second cladding is evident. Nevertheless, the increase in the second-cladding thickness also leads to a fading of the resonance in the mode transition region for two of the cases under study: LPG1 (second cladding of 1.06 µm) and LPG2 (0.79 µm), which is why in a certain region of **Fig. 4.7a** no values are shown for these two cases. Therefore, a trade-off between sensitivity and the ability to track the resonance band must be established.

Furthermore, the experimental (left) and theoretical (right) derivative of the wavelength shift with respect to the TiO_2 thin film thickness for LPGs 1-4 is shown in **Fig. 4.7b**. According to the numerical results, the maximum of the derivative increases and is shifted to a higher thickness when the second cladding is thicker, which is coherent with the results that had been observed for the effective indices of the cladding modes in **Fig. 4.5**. The experimental results agree regarding the maximum value of the derivative but not in the case of the thickness where this maximum is achieved. This is attributed to slightly different deposition rates in the different experiments due to inaccuracies in the ALD machine.

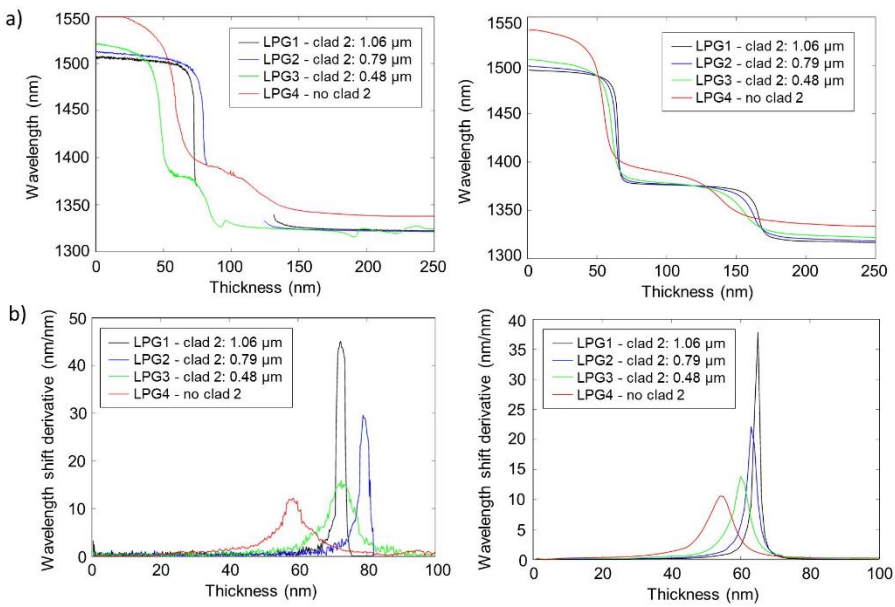

Fig. 4.7 a) Wavelength shift of the $HE_{1,14}$ band as a function of the TiO_2 thin film thickness (0 - 250 nm) for LPGs 1-4: experimental (left) and numerical (right) results. b) Derivative of the wavelength shift in a) in the 0 - 100 nm range: experimental (left) and numerical (right) results.

In order to understand the phenomenon better, **Fig. 4.8a** shows the optical field intensity for LPG 4 for thicknesses ranging from 55 to 70 nm in 5 nm steps, where the mode transition takes place. It is evident that the $HE_{1,2}$ mode is guided in the thin film for thicknesses above 65 nm, whereas mode $EH_{1,3}$ takes the shape of $HE_{1,2}$. This agrees with the evolution of the effective index in **Fig. 4.5**, where the mode $HE_{1,2}$

increases its effective index abruptly and $EH_{1,3}$ takes the effective index of $EH_{1,2}$ at the end of the transition. This occurs for all the remaining cladding modes.

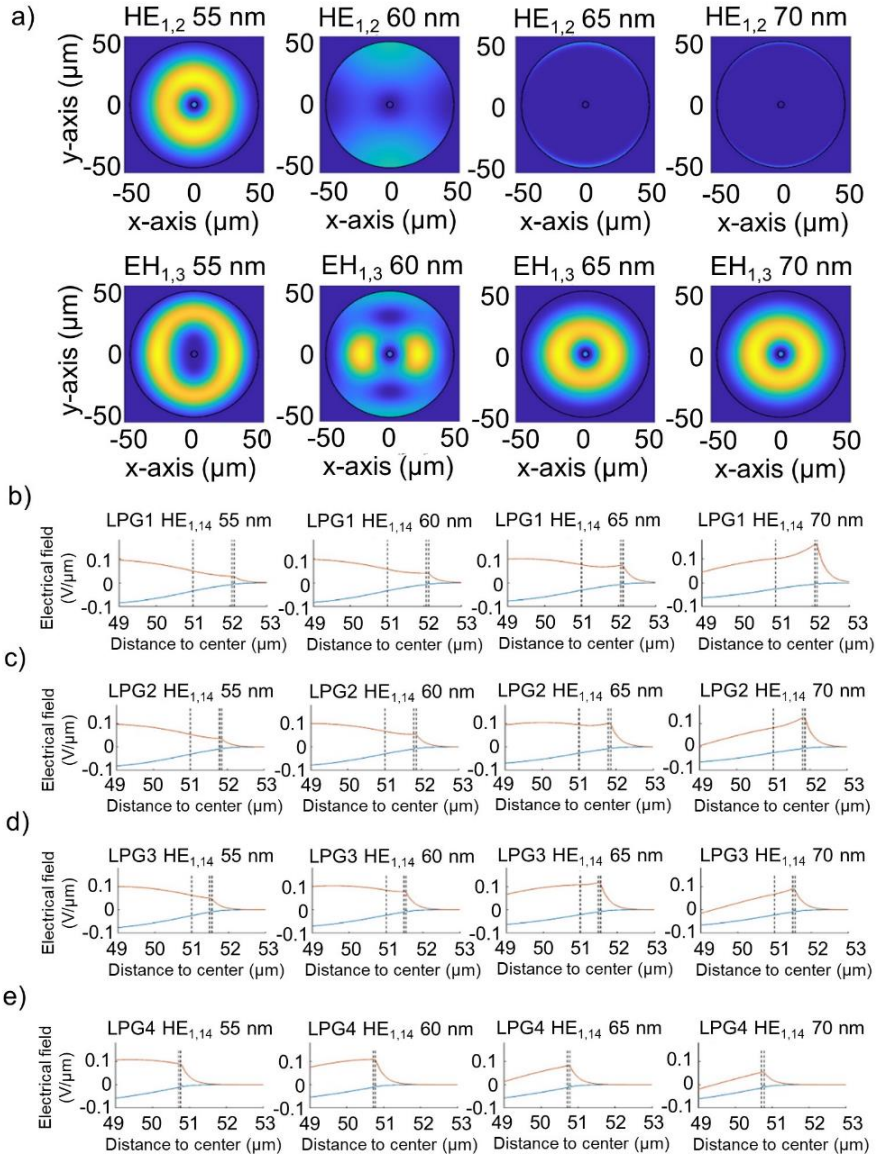

Fig. 4.8. Calculation of the fields. a) Field intensity distribution of $HE_{1,2}$ and $EH_{1,3}$ mode in the cross-section of LPG4 for TiO_2 thin film thicknesses in the 55 - 75 nm range. b-e) Radial (blue) and azimuthal (orange) field of $HE_{1,14}$ for LPGs 1-4, respectively, and the same thickness range as in a).

Moreover, in the range of 160 - 180 nm another transition takes place, something that is observed in **Fig. 4.5** for the effective index. Both transitions are also observed in **Fig. 4.6** in the evolution of the transmission spectra. The same effects take place for the rest of LPGs although the mode transitions happen at greater thicknesses (see again **Fig. 4.5**) due to the presence of the second cladding between the first cladding and the thin film, acting as a barrier for the guidance of the mode in the thin film.

In addition, **Figs. 4.8b-e** show the radial (in blue) and azimuthal (in orange) electric field of the $HE_{1,14}$ mode for thicknesses ranging from 55 to 70 nm in 5 nm steps. The transitions between layers are indicated with a dashed vertical line, with the two vertical lines that are close to each other corresponding to the TiO_2 thin film. It is evident, especially at 70 nm, that a higher azimuthal field is observed in the TiO_2 thin film for LPG1, the fiber with the thickest second cladding, thus establishing a connection between this enhancement of the field and the sensitivity increase observed in **Fig. 4.5** and **Fig. 4.6**.

4.2.2.3. Refractive index sensitivity

In this subsection the capability to control the thickness of the second cladding to optimize the sensitivity to RI in the mode transition will be assessed. For this purpose, two new LPGs (LPG5 and LPG6) were employed. Their wavelength shifts during the etching process were 6 and 15 nm, respectively; which correspond in **Fig. 4.4** to second-cladding thicknesses of 1.13 and 0.61 µm, respectively.

Then, both LPGs were deposited with TiO_2 using the ALD system until the first mode transition started, see **Fig. 4.9a** (LPG5 on the left and LPG6 on the right). The goal was to stop the deposition in the middle of the mode transition, where the sensitivity is the highest. This objective was achieved in the case of LPG6. In the case of LPG5, after some failed attempts with other similar LPGs, the deposition was stopped just after the mode transition had started (wavelength shift of only 8 nm). This decision was made because, with a thicker second cladding, the mode transition is more abrupt, making it difficult to stop the deposition in the exact desired point. Being excessively ambitious and waiting more before stopping the deposition can lead to skipping the whole transition, which happened in previous cases.

The characterization of both deposited LPGs was performed by immersing them in liquids with RI in the range from 1.33 to 1.47, the typical values studied when assessing the performance of optical fiber sensors [21], is shown in **Fig. 4.9b** (LPG5 on the left and LPG6 on the right). It is evident that a much higher sensitivity is achieved with LPG6, which has a thicker second cladding than LPG5, which was the expected result. For instance, in LPG6 the sensitivities for the upper wavelength band (in purple, corresponding to mode $EH_{1,15}$) are doubled in the 1.435 - 1.45 RI range compared to the ones achieved with LPG5 in that region. Moreover, values around 5000 nm/RIU are obtained at RI of 1.43 - 1.44, a result that could be improved with an LPG operating at the dispersion turning point (DTP), a case that for the sake of simplicity was not studied but that could be explored in a future work.

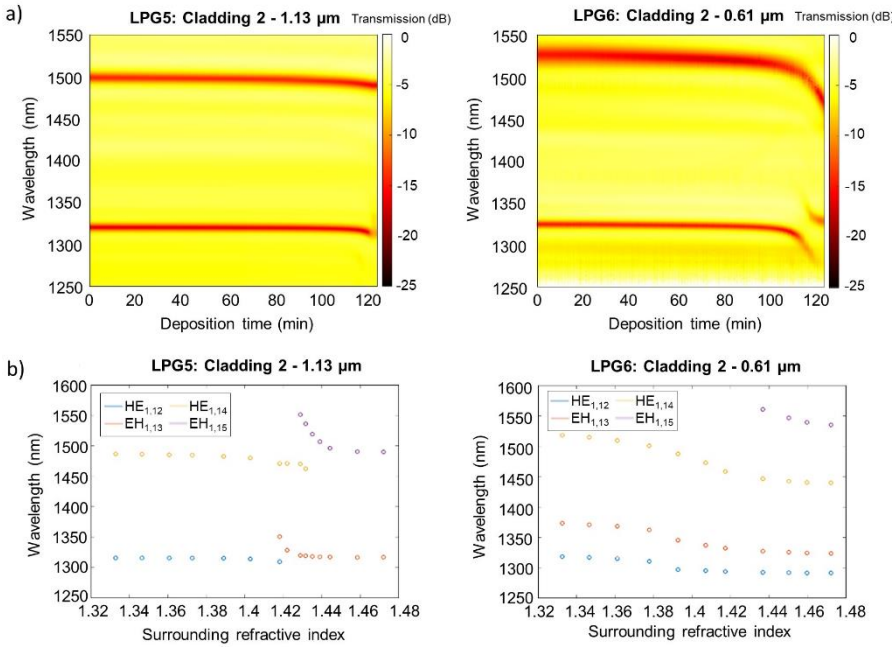

Fig. 4.9 a) Monitoring of the TiO_2 thin film deposition on LPG5 (left) and LPG6 (right). b) Wavelength shift of the LPG attenuation bands as a function of the surrounding medium refractive index (SRI): LPG5 (left) and LPG6 (right).

4.3. Mode transition in TFBGs

4.3.1. Materials and methods

The TFBGs that were used for studying the mode transition were in all cases inscribed over a length of 1 cm on a standard single mode fiber (Corning® SMF-28) with a core/cladding diameter of 8/125 µm. A pulsed KrF excimer laser (PM-800, Light Machinery) was used to fabricate the grating by the phase mask technique and hydrogen loading of the fiber to enhance its photosensitivity. The FBG peak was located at approximately 1610 nm, the grating period along the fiber axial direction was around 554 nm and the tilt angle was 9.5º

During the deposition, one end of the fiber was connected to a multi-SLD source (FJORD-X3, Pyroistech S.L.) through an in-line polarizer and a polarization controller (Phoenix Photonics Ltd), which enabled selecting a P or S linearly polarized state (relative to the tilt plane) for the core-guided light incident on the TFBG. The other end of the fiber was connected to an optical spectrum analyzer (MS9740A from Anritsu in the case of the ITO deposition, HP-86142A from Agilent in the case of the TiO_2 deposition) to monitor the spectrum, see **Fig. 4.10**.

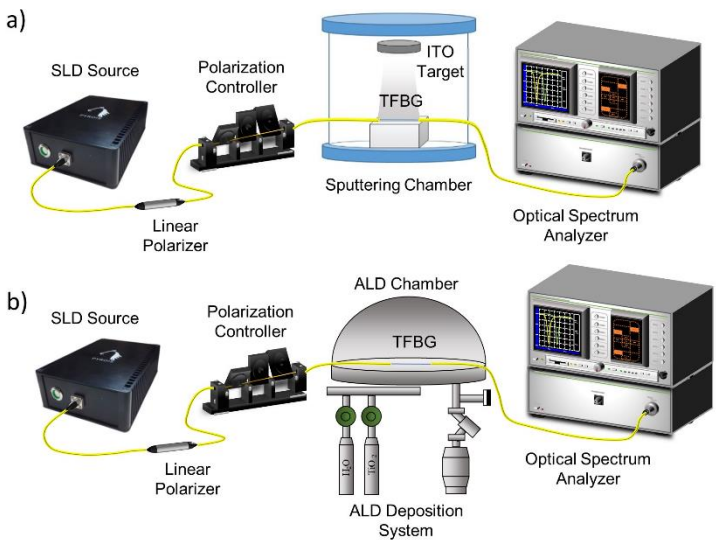

Fig. 4.10 a) Schematic of the setup used for monitoring the mode transition in the TFBG while depositing a ITO thin film with the sputtering system. b) Same as a) but for depositing TiO_2 with an ALD system. It can be appreciated that the only relevant difference is the deposition system. a) Reproduced from [22]. Copyright 2022, Optica Publishing Group. b) Reproduced from [23]. Copyright 2022, IEEE.

The main difference between the ITO and the TiO_2 depositions was that in the first case the thin film was deposited over the TFBG using a DC sputtering machine (Emitech K675X, Quorum Technologies Ltd.) while in the second the atomic layer deposition method (Savannah G2 ALD System from Veeco Inc) was employed, see again **Fig. 4.10**. Regarding the materials, an ITO target (90% In_2O_3, 10% SnO_2) from

Loyal target Technology Co was utilized whereas for the TiO_2, ultrapure water and tetrakis(dimethylamido) titanium(IV) (669008, Sigma-Aldrich) were employed as precursors.

It was decided to change to the ALD deposition system after analyzing the results obtained with the deposition done using the sputtering technique. Sputtering deposition technique presents several disadvantages that will be shown in detail in the results section. In the first place, the sputtering deposition time of the employed machine is limited to 4 minutes, which was not enough to deposit the desired thickness. In addition to this, the temperature in the sputtering chamber during the deposition process is not constant, rising at the beginning and dropping at the end, causing an overlap of the shift due to the mode transition and the shift caused by the temperature change, thus leading to a more complex data treatment. In the ALD deposition process, the temperature is constant and equal to 100ºC. The change of material (from ITO to TiO_2) was due to the available materials in the ALD system. Both materials (ITO [24], TiO_2 [25]) meet the conditions for the mode transition, i.e. a higher refractive index than the substrate (~1.444 for SiO_2 at these wavelengths) and a low imaginary part of the refractive index [26].

An ellipsometer (UVISEL 2, Horiba Scientific Thin Film Division) with a spectral range of 0.6–6.5 eV (190–2100 nm), an angle of incidence of 70º, a spot size of 1 mm and software DeltaPsi2™ (from Horiba Scientific Thin Film Division) was used to characterize the thickness, the real part of the refractive index (n) and the imaginary part of the refractive index or extinction coefficient (k) of the deposited thin films. The analyzed samples consisted of small pieces of silicon wafers that were placed next to the TFBGs inside the sputtering or ALD chamber during the depositions. In the case of the TiO_2 depositions, the thin film thickness was also measured with a field-emission scanning electron microscope (UltraPlus FESEM, Carl Zeiss, Inc.) with an in-lens detector at 3 kV and an aperture diameter of 30 μm. The thickness was measured on different points of several transversal cuts for each TFBG.

The first simulation regarding the evolution of the effective indices of the cladding modes as a function of the thin film thickness was calculated with the commercial software FIMMWAVE® (Photon Design Inc.). Three sections were defined: a single-mode fiber (SMF) segment, a SMF segment with a TFBG inscribed on the core and another SMF segment. In all the sections, the finite difference method (FDM) was employed because it is the most accurate method available for a cylindrical waveguide. In the case of the TFBG, the Eigen-Mode Expansion (EME) algorithm was chosen for the gratings. 85 modes were simulated because they are enough to simulate the high order cladding modes that correspond to the wavelength range that was studied in the experimental depositions. The model for SiO_2 was obtained from [20] and the real part (n) and the imaginary part (k) of the refractive index of TiO_2 employed in the simulations were taken from the ellipsometry measurements (see **Fig. 4.11**). At the wavelength range used in this work, $n = 2.14$ and $k = 0$).

More detailed simulations concerning the effective index and the mode power distribution evolution were performed in MATLAB© using a combination of two

algorithms: a fiber mode solver and complex coupled-mode program to calculate TFBG transmission spectra [27]. The mode solver algorithm is based on the finite difference method with a resolution of 3 nm over the 80 mm radius of the calculation window in the radial direction and independent calculations for mode azimuthal orders 0 to 7. The mode solver allows for any number of azimuthally uniform layers in the radial direction, and in particular coatings of any thickness on the cladding surface. The coupled mode approach to calculate transmission spectra is based on [28], with improvements as follows. At each wavelength in a calculated spectrum, 28 modes are calculated (by the mode solver) around an effective index value determined by the requirement of phase matching from the core mode at this wavelength. Then, coupling coefficients for all these modes are calculated and the coupled mode equations solved over the grating length by a Runge-Kutta algorithm. The refractive indices of the core and cladding materials are also recalculated at each wavelength to account for dispersion, using pure silica values for the cladding (obtained from [20]), a constant value of 1.0 for the surrounding medium, and the core index dispersion determined for each grating used. The values employed for TiO_2 are again the ones from the ellipsometry measurements (see **Fig. 4.11**).

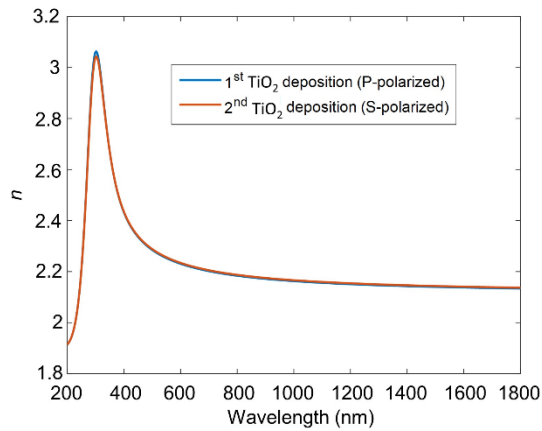

Fig. 4.11 Ellipsometric measurement of the real part of the refractive index (n) of the TiO_2 coatings fabricated onto silicon wafers at the end of each of the two monitored depositions done using this material. Reproduced from [23]. Copyright 2022, IEEE.

4.3.2. Results

4.3.2.1. Real time spectral evolutions during deposition

The P- and S-polarized states can be recognized unambiguously by rotating the input polarization before the deposition since TFBG come in pairs where the shortest member of the pair corresponds to the EH mode (P-polarized state) and the other one to the HE mode (S-polarized state) [29], as it can be observed in **Fig. 4.12**. It must also be noted that high order EH modes have radially polarized electric fields at the cladding surface while HE modes are azimuthally polarized [28,29].

In the first place, a monitored ITO deposition on a TFBG was carried out in the sputtering machine. The TFBG was measured employing S-polarized light (coupling to HE modes only). **Fig. 4.13a** shows the evolution of the central part of the transmission spectrum (1560 - 1570 nm) during the experiment (one spectrum is acquired every 8.5 s). The results were recorded for this wavelength window because the resonances are the narrowest and the deepest, making them easier to track. During the 25 minutes previous to t = 0, the pump was making vacuum in order to achieve the required pressure (this time interval has been removed because it does not add information). It must also be mentioned that a constant value has been added to the spectra to compensate the losses of the setup so their baseline is located at 0 dB.

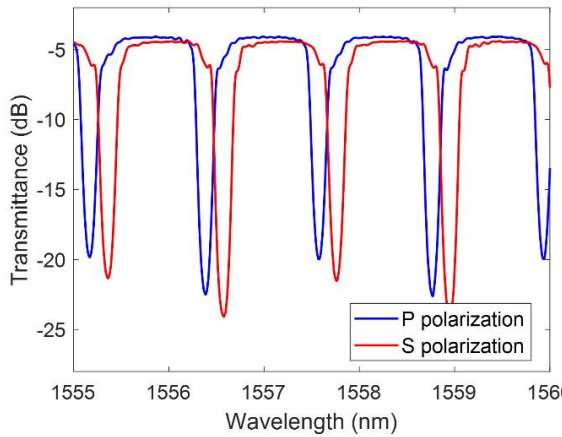

Fig. 4.12 P- and S-polarized spectrum of a TFBG with similar characteristics to the ones used in these experiments in the range 1555 - 1560 nm.

Nevertheless, the results shown in **Fig. 4.13a** are difficult to directly understand. This happens due to several reasons. In the first place, in the employed sputtering machine, the deposition time is limited to 4 min. Two deposition cycles were done, but a time of 6 min had to be waited between both. In **Fig. 4.13a**, the two deposition cycles correspond approximately to time intervals [2.5 6.5] and [12.5 17.5] while in the 6 min. interval between them, no material was deposited. This time interval must be removed to achieve a good understanding of the deposition process. In the second place, the temperature was not constant during the deposition process so the shift of the resonances due to the mode transition is overlapped with the shift caused by the temperature change. This effect can be easily removed by measuring the wavelength shift of the Bragg peak (see **Fig. 4.13b**), which is not affected by the mode transition, and subtracting this shift from the cladding mode resonances, as the temperature sensitivity of all the resonances is approximately the same (10 pm/ºC) [30]. It can be observed in **Fig. 4.13b**, considering the temperature sensitivity, that a temperature rise of approximately 80ºC took place in both deposition cycles and that the initial temperature was not recovered during the 6 min between both of them.

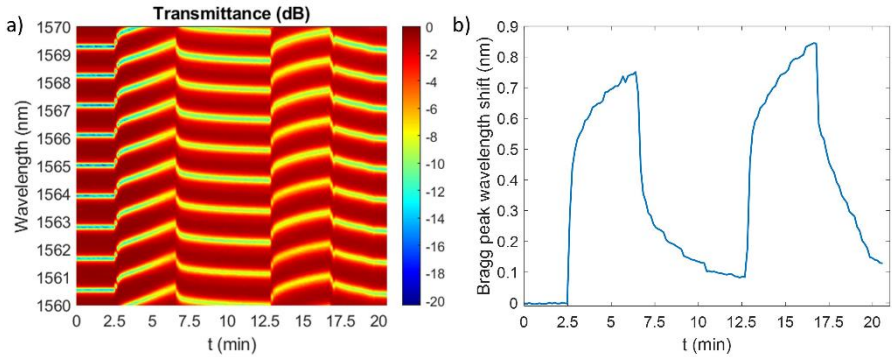

Fig. 4.13 a) Experimental ITO deposition with S-polarized input light in the 1560 - 1570 nm range with the sputtering system. b) Bragg peak wavelength shift during the deposition.

In consequence, to provide a better comprehension of the deposition process, the 6 intermediate minutes where no deposition takes place have to be removed and the temperature shift has to be compensated. If these changes are implemented, and some minor discontinuities between the different time intervals are also erased, **Fig. 4.13a** transforms into **Fig. 4.14**, where the mode transition effect caused by the lossy mode resonance (LMR) phenomenon can be clearly observed. There is an acceleration of the wavelength shift with time (and hence thickness), achieving the maximum change rate approximately at t = 6 min. In this new time axis, the deposition takes place approximately between t = 2 min and t = 10 min, which corresponds to a thin film thickness of about 400 nm, measured with an ellipsometer UVISEL 2 from Horiba Ltd.

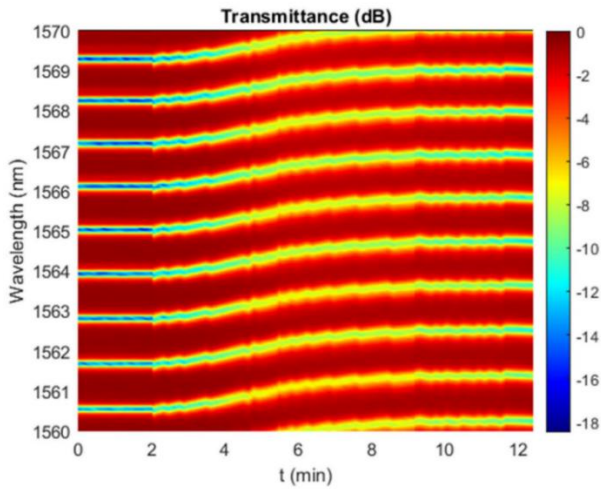

Fig. 4.14 Experimental ITO deposition with S-polarized input light in the 1560 - 1570 nm range with the sputtering system after the removal of the time between the two deposition intervals and the temperature compensation. The mode transition is clearly recognizable after these corrections. Adapted from [22]. Copyright 2022, Optica Publishing Group.

A fading phenomenon can also be observed in **Fig. 4.14**. While the deposition takes place, the resonances become shallower until around t = 6 min, when the resonances start becoming deeper again, partially regaining the depth that they initially had. This phenomenon has been observed in LPGs [3,6]. However, the particularity is that here, with a material with a non-negligible imaginary part, the resonances do not completely fade. This can be attributed to the fact that the studied resonances are due to higher order modes, located far from the mode that is guided in the thin-film. Hence, according to [26] the fading effect is diminished. It is also important to remark that the fading phenomenon has no relationship with the temperature shift that was previously compensated, as the TFBG spectrum is invariant under temperature changes, apart from the global shift of the resonances [30].

In order to observe this fading phenomenon in detail, **Fig. 4.15a** and **Fig. 4.15b** show the resonances of the TFBG spectrum in the 1564 - 1566 nm range. For example, for the resonance that starts at a wavelength of 1564 nm, the initial depth is around -15 dB, which starts progressively decreasing once the deposition begins, with a value of -12 dB for t = 3 min and -9.7 dB for t = 4.5 min, until attaining a value of -9 dB for t = 6 min. The resonances maintain a similar depth until t = 9 min, becoming deeper afterwards, with around -10 dB for t = 10.5 min and -12 dB for t = 12 min.

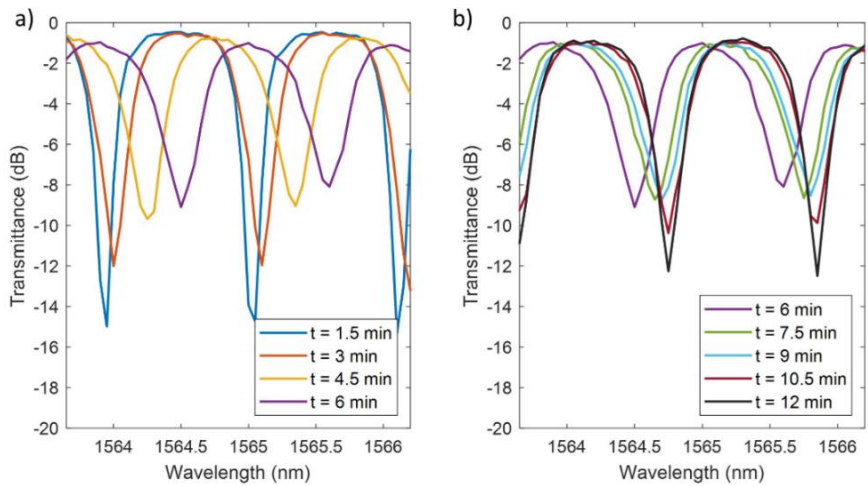

Fig. 4.15 a) TFBG resonances between 1564 and 1566 nm during the mode transition, t = 1.5 - 6 min b) Same as a) but with t = 6 - 12 min. Reproduced from [22]. Copyright 2022, Optica.

After this monitored deposition in the sputtering machine with ITO, it was decided to repeat the process with the ALD system due to the problems that had been observed with the sputtering (deposition time limited to 4 min and not constant temperature). In the ALD system the deposition time is not limited and the temperature remains constant (in case of the employed recipe, the temperature inside the chamber is set to 100ºC). The dome lid was employed. It has a pass through hole, sealed with resin, that enables two fibers to go inside the chamber, one for the input light and the other for the output light. The deposited material was changed from ITO to TiO_2 as ITO was not among the materials that were available for the ALD system.

Two TiO_2 depositions, each one on a different TFBG, were carried out with a duration of 500 minutes in the ALD system (it must be remarked that the deposition rate is much slower than for sputtering). In the first one, see **Fig. 4.16a**, the TFBG was measured using P-polarized light (which couples to EH modes of the cladding) while in the second one, see **Fig. 4.16b**, S-polarized light was used (coupling to HE modes only). Fig. 4 shows the evolution of the central part of the transmission spectrum of each TFBG as a function of deposition time. Note that in both cases the modes corresponding to the other polarization can be observed, in spite of being very faint (HE modes in **Fig. 4.16a** and EH modes in **Fig. 4.16b**), due to incomplete polarization alignment in the non-polarization maintaining fiber used.

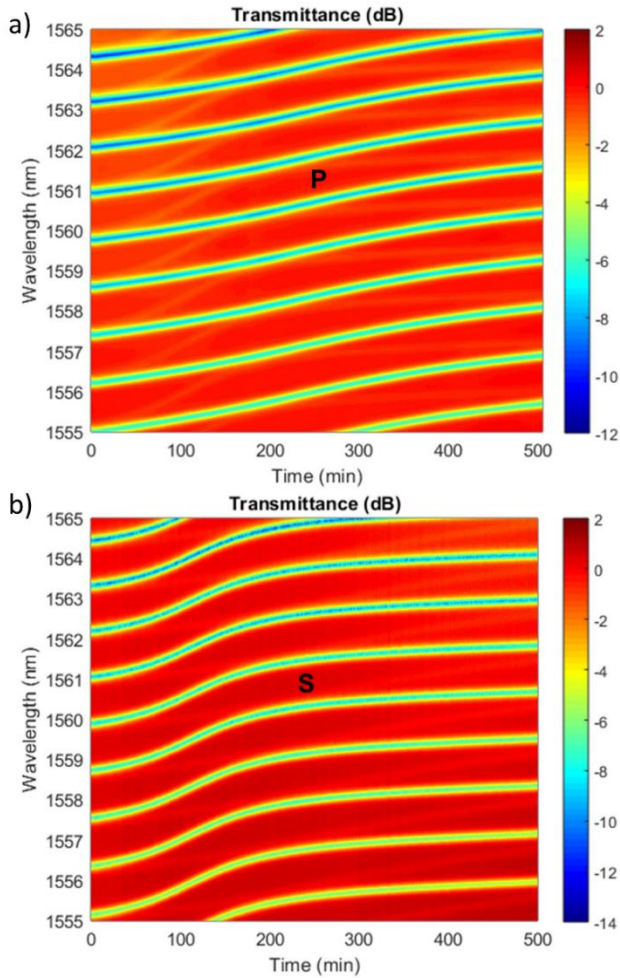

Fig. 4.16 a) Experimental TiO_2 deposition with P-polarized input light in the 1555 - 1565 nm range with the ALD system. b) Same as a) but with S-polarized light. Reproduced from [23]. Copyright 2022, IEEE.

The experimental results were recorded for the 1555 - 1565 nm window, a similar range to the one used in the ITO deposition (1560 - 1570 nm), because the resonances are the narrowest and the deepest and the wavelength shift is larger than in the case of the resonances located at higher wavelengths. The effect of the mode transition caused by the LMR phenomenon can be observed in both graphs as an acceleration of the wavelength shifts with time (and thus thickness) across the initial wavelengths of lower order resonances. The mode transition is much sharper for HE modes (see again **Fig. 4.16b**), where the electric field of the cladding modes is polarized along the fiber surface (i.e. in the plane of the deposited film). It must also be remarked that the difficulties present in the ITO deposition data treatment, which were associated to the sputtering deposition system characteristics, did not appear in this case, as it was expected.

4.3.2.2. Modelling the mode transition

In order to explain the spectral changes measured experimentally for both types of modes, simulations were carried out to calculate how the effective index of cladding modes change as a function of coating thickness: they should replicate closely the measured wavelength shifts as a function of time because of the one-to-one relationship between resonance wavelength and effective index given by the phase matching condition:

$$\lambda = \left(n_{core}(\lambda) + n^{i}_{cladding}(\lambda)\right) \cdot \frac{\Lambda}{cos\theta} \tag{4.2}$$

where $n_{core}\ (\lambda)$ is the effective refractive index of the core mode at λ, $n^{i}_{cladding}\ (\lambda)$ is the effective refractive index of the *i*th cladding mode at λ, Λ is the grating period and θ is the tilt angle. The simulations will be focused on the TiO_2 depositions.

In the first place, **Fig. 4.17** shows the evolution of the effective indices of the cladding modes as a function of the TiO_2 coating thickness at a wavelength of 1560 nm for a generic TFBG with similar characteristics to the ones used in these experiments (please note that the vertical scale is not the same for the low order modes, **Fig. 4.17a**; and the high order modes, **Fig. 4.17b**). The employed value for *n* was 2.14, given by the ellipsometry, as shown in **Fig. 4.11**. Similar results would have been obtained with ITO, although the transitions would be smoother as the refractive index of ITO is lower than that of TiO_2. It can be observed that the evolution of the effective indices of the high order modes (**Fig. 4.17b**) with the increasing thin film thickness follows the same tendency as the wavelength shifts with time shown in **Fig. 4.14** (ITO) and **Fig. 4.16** (TiO_2), as these resonances correspond to high order cladding modes. Obviously, resonances have to be compared with the corresponding modes, that is, S-polarized resonances (**Fig. 4.14**, **Fig. 4.16b**) with $HE_{1,x}$ modes and P-polarized resonances (**Fig. 4.16a**) with $EH_{1,x}$ modes

Although only high order modes are interesting regarding their comparison with the previous experimental results, both low order (**Fig. 4.17a**) and high order modes (**Fig. 4.17b**) have been simulated as they enable to illustrate some relevant aspects. Low order cladding modes are typically used with LPGs, while high order modes

have been employed in our experiments with TFBGs. By comparing **Fig. 4.17a** and **Fig. 4.17b**, it can be appreciated that the sharpness of mode transitions diminishes with decreasing mode index (higher order mode) and subsequent mode transitions occur at larger thicknesses. It can also be remarked that for low order cladding modes, the transition takes place in a double step (first step at around a thickness of 100 nm and second step at approximately 200 nm in this case) while for high order cladding modes the transitions become smoother and they fuse into a single smooth transition. Finally, higher order modes are preferentially used in most TFBG research because, as it is shown in **Fig. 4.17**, the resonances corresponding to low order modes are very tightly grouped and tend to overlap in measured spectra, making it difficult to follow individual wavelength shifts with precision.

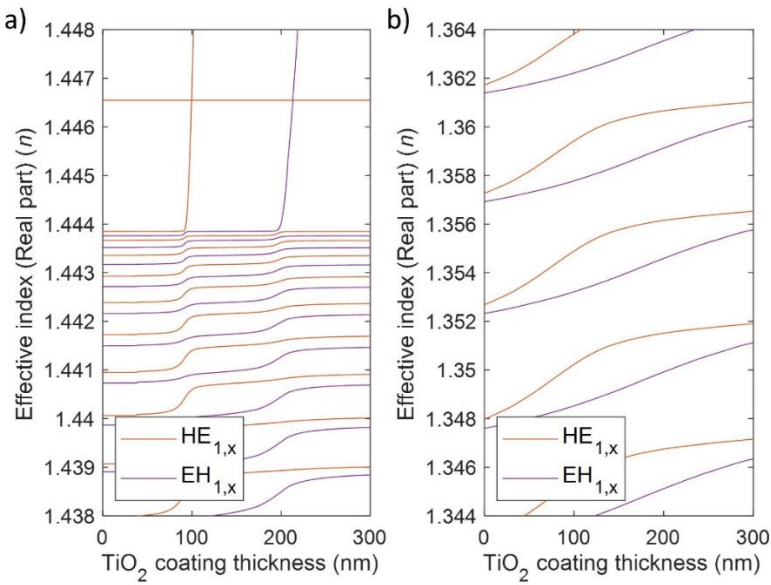

Fig. 4.17 a) Simulation of the evolution of the effective indices of some $HE_{1,x}$ and $EH_{1,x}$ low order modes as a function of the TiO_2 (n = 2.14) coating thickness. b) Same for some high order cladding modes. Adapted from [23]. Copyright 2022, IEEE.

After this initial simulation, a more detailed simulation of the effective index of some cladding modes and the power distribution of the mode fields was carried out for the TFBGs employed in the TiO_2 depositions. The purpose of simulating the power distribution of the mode fields was to understand why wavelength shifts accelerate at certain times/thicknesses and why there is such a pronounced difference between EH and HE modes.

Before simulations, the core index at the Bragg wavelength and its dispersion were determined from a calibration of the grating used in each experiment to adjust the simulated spectra to the experimental one measured in air prior to deposition. This calibration is necessary due to the fact that the laser irradiation used to create the grating increases the refractive index and dispersion of the doped silica glass used in

the fiber core, and these changes vary significantly for each grating fabricated [31]. The calibrated core index vs wavelength (λ) is expressed as: $n(\lambda) = n(\lambda_B) + (\lambda_B - \lambda) \cdot S$ where λ_B is the Bragg wavelength of the grating in nm, and S the dispersion in nm^{-1}. For the two gratings used in the TiO_2 depositions, the calibration results are listed in **Table 4.2**. Once calibrated, the errors in the resonance positions of the simulated spectra relative to those of the corresponding bare TFBG are minimized over the spectral ranges used with an average value of less than 1 pm and a standard deviation under 10 pm.

Table 4.2 Parameters used in the simulations for the TFBGs

Grating	λ_B (nm)	$n(\lambda_B)$	S (nm^{-1})
P-polarized (TiO_2)	1609.781	1.4517697	0.000018150
S-polarized (TiO_2)	1609.794	1.4519956	0.000019123

The origin of the mode transition is best explained from the simulations shown in **Fig. 4.18** where the effective index and the power fraction in the coating of selected modes (with resonances near 1560 nm) are plotted as a function of the TiO_2 thin film thickness for one EH mode (corresponding to the P-polarized deposition) and one HE mode (corresponding to the S-polarized deposition). It can be observed that the evolution of the effective indices of the modes with the increasing thin film thickness follows the same tendency as the wavelength shifts with time shown in **Fig. 4.14** (ITO, in spite of not being the same material, the general tendency should be the same) and **Fig. 4.16** (TiO_2). This result was expected because wavelength shift is equivalent to effective index shift due to the phase matching condition for the resonances (see again equation (1)), as it has been previously stated.

It can also be realized that the rate of change of the mode effective index is closely linked to the power density of the mode in the overlay: the maximum rate of change matches quite closely a maximum in the mode power fraction in the TiO_2 coating (around 230 nm in the case of the EH mode and approximately 90 nm in the case of the HE mode). This was expected from perturbation analysis, where changes in mode effective indices are directly proportional to the fraction of the mode power in the fiber cross section where changes (in dimensions or refractive index) are occurring.

What is less clear is why the mode transition is sharper and occurring at a much smaller thickness for HE modes than for EH modes, and yet almost exactly equal in terms of total wavelength shift (or effective index shift, which is equivalent because of the phase matching condition for the resonances). This represents one more example of the differential sensing capabilities of TFBGs in various situations, arising from the fact that each resonance corresponds to different mode groups.

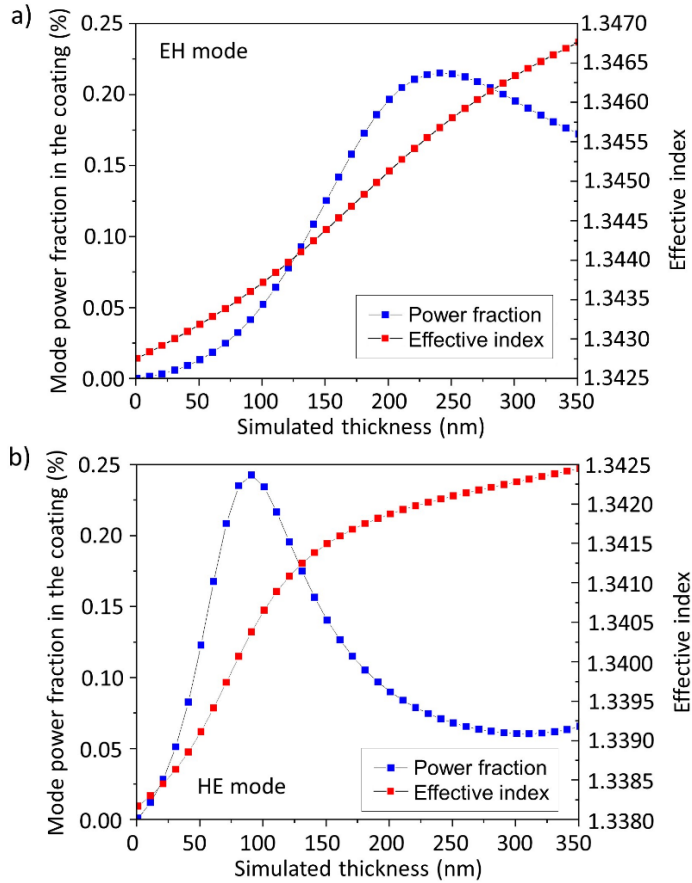

Fig. 4.18 a) Mode power fraction in the coating (%) and effective index vs simulated TiO_2 thickness for a EH mode in the 1555 - 1565 nm window. b) Same for a HE mode. Reproduced from [23]. Copyright 2022, IEEE.

4.3.2.3. Thin film thickness measurements during deposition

The success of the spectrum and mode simulations in replicating the experimental results points to a method for using TFBG spectra to measure thin film thicknesses as a function of time, in situ inside a deposition chamber. This is particularly true for ALD since coatings in this case are conformal and depend minimally on the shape of the coated surfaces [32].

In order to validate this hypothesis, a representative resonance in each spectrum of the TFBGs that had been used for the TiO_2 depositions was selected and its central wavelength measured as a function of time. Then, simulations were carried out to determine how the chosen resonance shifts as a function of the thin film thickness, for a thin film index of n = 2.14 (the separately determined experimental value for TiO_2, see **Fig. 4.11**).

Based on the assumption that the deposition rate is constant, it is then possible to match the two data sets to determine a deposition rate that makes the simulated and experimental shifts coincide. The deposition rates that provide the best agreement between the experimental and theoretical mode transitions are 669 pm/min and 638 pm/min for the P-measured grating and the S-measured grating respectively and the corresponding results are shown in **Fig. 4.19**. These deposition rates provide final thickness values of 334 nm and 319 nm respectively. These results are compared with the ones obtained with the scanning electron microscope (SEM) and the ellipsometer in **Table 4.3** and **Table 4.4**.

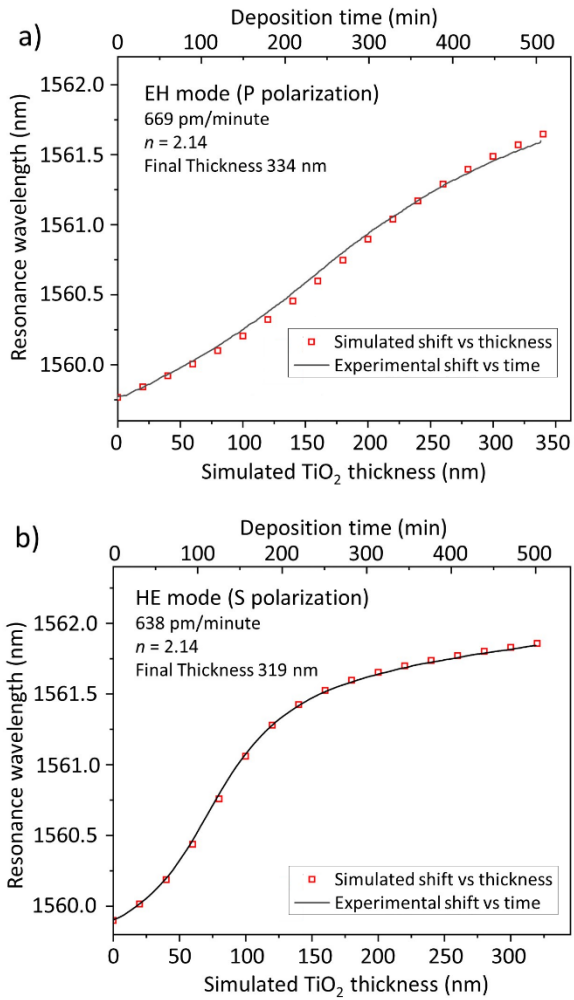

Fig. 4.19 a) Comparison of the experimental and theoretical wavelength shifts for the P-polarized TiO_2 deposition for the mode transitions that begins at 1560 nm. b) Same for the S-polarized deposition. The deposition rate and final thickness are determined by scaling the thickness scale until it fits the time scale. Reproduced from [23]. Copyright 2022, IEEE.

Table 4.3 Measured TiO_2 thin film thickness for the two deposited TFBGs with different methods.

	Measured TiO_2 thin film thickness (nm)		
Method	**P-polarized TFBG**	**S-polarized TFBG**	**Difference (%)**
Our method	334	319	5%
SEM ($\mu \pm \sigma$)	367 ± 63 (304, 430) (13 measurements)	323 ± 74 (249, 397) (15 measurements)	14%
Ellipsometer	396	390	2%

Table 4.4 Comparison of the measured TiO_2 thin film thickness between the different methods.

	P-polarized TFBG		**S-polarized TFBG**	
Method	**SEM**	**Ellipsometer**	**SEM**	**Ellipsometer**
Our method	-9%	-16%	-1%	-18%
Ellipsometer	8%	-	21%	-

In the first place, it has to be mentioned that the employment of the dome lid in the ALD system resulted in not very homogeneous coatings as it is shown by the high standard deviation of the SEM measurements (63 and 74 nm respectively for each fiber). This SEM measurements were performed on different points on several transversal cuts of each TFBG, as opposed to the ellipsometer measurements, which were done by analyzing pieces of silicon wafers that were placed next to the TFBGs during the deposition. Similar measurements done with fibers that were deposited by using the ALD system with the flat lid gave a much lower standard deviation, between 10 and 25 nm (3 to 6 times lower). Unfortunately, the flat lid cannot be used for monitored depositions as it will have to be closed over a section of the input and output fibers, squeezing and breaking them.

Regarding the P-polarized TFBG, the difference between the results obtained with our method and the ones from the SEM is very similar to the difference between the SEM's and the ellipsometer's results (around 8-9 %) while the difference between our method and the ellipsometer is larger, around 16%. In the case of the S-polarized TFBG, our method's thickness is very similar to the average thickness given by the SEM (1%) and differs a lot from the one obtained with the ellipsometer (18%). It must be also be remarked that both depositions were done in the same conditions and lasted the same time (500 min) so the final thickness should be same. Both our method and the ellipsometer present a reasonable difference (5% and 2%, respectively), while it is larger in the case of the SEM (14%).

It has to be mentioned that SEM results should be, in principle, more reliable than the ones from the ellipsometer. The SEM values are based on a direct measurement while the ellipsometer uses an indirect measurement, determining both the refractive index (n, k) and the thin film thickness from two measured angles [33]. Considering this, it is positive that the results from our method are closer to the SEM ones than to the ellipsometer's. In case of the S-polarized TFBG almost the same result is obtained, while for the P-polarized TFBG the difference is larger (9%). Nevertheless, it can be observed that our method achieves a much better fit for the S-polarized transition (see **Fig. 4.19b**) than for the P-polarized one (see **Fig. 4.19a**), which may explain the worse result for the P-polarized TFBG when using the SEM results as reference. In spite of testing other deposition rates for the P-polarized TFBG, no better fit was obtained than the one shown before. However, it must be taken into account that our method uses the refractive index value given by the ellipsometer measurements. Therefore, the next step is to improve the current method so it is capable of measuring simultaneously the thin film thickness and its refractive index without employing any data from the ellipsometer.

4.4. Conclusions

In this chapter, the mode transition phenomenon has been studied, both numerically and experimentally, in two types of optical fiber structures: double-clad LPGs in which the refractive index of the second cladding is lower than that of the first cladding, and TFBGs. In both cases the mode transition has been obtained by the deposition of high RI thin film. The main aspects that have been studied for both structures are synthesized in **Table 4.5** and the obtained results are explained in the following paragraphs.

In the first case, it has been demonstrated that the proposed structure enhances the sensitivity during the mode transition compared with an LPG operating at the same point but without a second cladding. Many years have passed since this idea was first proposed theoretically [11]. This is a result of the great challenge of finding a material with low RI and low absorption, which has been solved by double-clad fibers whose second cladding is doped with fluorine to reduce the refractive index. Another difficulty was to reduce the thickness of the second cladding, which initially was too thick, around 10 µm. Therefore, it was necessary to apply a smooth etching process that enabled a precise control of the second-cladding thickness.

With these two conditions, it was possible by means of an ALD process to monitor four different cases where the effect of the low RI second cladding was evident in air, demonstrating that the mode transition phenomenon is tunable with an intermediate low RI layer. The concept was also demonstrated in liquid, where the device with a thicker second cladding showed better sensitivity, with values above 5000 nm/RIU. All this was achieved in a non-optimal device whose period was far from the dispersion turning point. Consequently, there is still room to improve the performance of the proposed devices.

In addition, the required technology can be greatly simplified. Here, an ALD process was employed because it permitted observing the evolution of the phenomenon very

slowly, but other techniques, such as sputtering, could also be used. Regarding the optical fiber, once an optimal design is obtained, double-clad fibers, where the thickness of the second cladding is initially the optimal, could overcome the need of an etching process. On the other hand, although a higher fading was observed when the highest sensitivities were obtained, parameters such as the length of the device or the modulation index could be optimised to reduce this effect. Finally, the concept of optical fibers with a thin second cladding could be expanded to other structures, such as TFGBs, which suggests that this work could open a new and extensive line of research in the field of optical fiber sensors.

Regarding the second part of the chapter, results were presented to demonstrate experimentally that lossy mode resonances (LMR) are associated with mode transitions in TFBGs coated with materials having a refractive index higher than that of the silica cladding (ITO and TiO_2 were used in this case), similarly with LPGs [8,34,35]. This result was confirmed by simulations of TFBG spectra that showed how the mode transition is associated with mode power localization peaks in the coating for specific thicknesses. In TFBGs, the mode transition phenomenon applies to resonances that have much higher Q-factors than in LPGs, but lower inherent sensitivities, a common trade-off between these technologies. Nevertheless, it can be noted that TFBGs have several "insensitive" resonances in their spectrum that can be used to improve accuracy by removing cross sensitivities, such as in plasmonic amplification when an additional metal coating is used [36].

Another important property observed in TFBGs is that the resonances can be tracked without a significant depth reduction (a partial depth reduction was observed in ITO, but none in the case of TiO_2), as opposed to LPGs and SMS fibers, during the entire mode transition. Moreover, it was demonstrated here that the spectra of both P and S polarizations can be obtained separately by adequately controlling the polarization state of the incidence light, and that the mode transition has widely different properties for the two orthogonal input polarization states. This result can lead to sensing modalities by means of differential measurements based on alternating or separating input polarizations, and potentially on measurements on birefringent coatings.

On the other hand, the obtained results confirm that the simulation tools developed to model TFBGs and coated TFBGs work well as they reproduce experimental spectral features and wavelength shifts accurately over many changes in parameters. In particular, it is clear that the observed mode transition is showing up in exactly the same way in the experimental wavelength shift data and in the simulated effective index data, providing a key to finding the deposition rate of the system and to confirming the origin of the mode transition phenomenon. The accuracy of the model in the canonical case of the bare fiber in air (which is at the limit of the measurement capabilities of most spectrum measurement instrumentation) ensures that the underlying algorithms are correct and that extrapolation to more complex situations (i.e. the presence of an additional coating of varying thickness) is reliable.

Finally, the measured mode transition data was combined with the value of the coating refractive index to determine the thicknesses of the deposited TiO_2 thin films.

This method could be used to extract film thicknesses in real time during deposition by ALD, enabling researchers and users of this thin film technology to monitor the stability of the processes routinely and to produce thin films with very precise thicknesses by stopping the process at the desired value (at the peak of the mode transition for instance). Obviously, a new TFBG probe would be required for each new deposition, but there are process runs in the semiconductor and optical industries that are so valuable that the cost of a single-use disposable probe would be insignificant (TFBGs can be mass-produced the same way as FBGs, with the same tools, at very low cost).

Table 4.5 Main aspects of the mode transition studied for double-clad LPGs and TFBGs in Chapter 4.

Structure	Main aspects
Double-clad LPGs	• Effect of the second cladding thickness on the mode transition (sensitivity to the thin film thickness analysis) • Enhancement of the SRI sensitivity by means of the second cladding thickness • Experimental results supported with simulations of the wavelength shift of the resonances, evolution of the effective indices of the cladding modes and optical field intensities
TFBGs	• Two different materials (ITO, TiO_2) and deposition systems (sputtering, ALD) • Fading phenomenon during the mode transition in the ITO case, but the resonances do not completely disappear • Mode transition studied with both polarizations (P and S) in the TiO_2 case. Important differences between both polarizations • Experimental results supported with simulations of the effective indices of the cladding modes and the mode power fraction in the coating • Experimental results combined with simulations to recover the thin film final thickness in the case of the TiO_2 depositions

Bibliography

1. Cusano, A.; Iadicicco, A.; Pilla, P.; Contessa, L.; Campopiano, S.; Cutolo, A.; Giordano, M.; Vengsarkar, A.M.; Lemaire, P.J.; Judkins, J.B.; et al. Mode Transition in High Refractive Index Coated Long Period Gratings. *Optics Express, Vol. 14, Issue 1, pp. 19-34* **2006**, *14*, 19–34, doi:10.1364/OPEX.14.000019.

2. Rees, N.D.; James, S.W.; Tatam, R.P.; Ashwell, G.J. Optical Fiber Long-Period Gratings with Langmuir–Blodgett Thin-Film Overlays. *Optics Letters, Vol. 27, Issue 9, pp. 686-688* **2002**, *27*, 686–688, doi:10.1364/OL.27.000686.

3. Del Villar, I.; Achaerandio, M.; Matías, I.R.; Arregui, F.J. Deposition of Overlays by Electrostatic Self-Assembly in Long-Period Fiber Gratings. *Optics Letters, Vol. 30, Issue 7, pp. 720-722* **2005**, *30*, 720–722, doi:10.1364/OL.30.000720.

4. Del Villar, I.; Matías, I.R.; Arregui, F.J.; Lalanne, P.; Vengsarkar, A.M.; Lemaire, P.J.; Judkins, J.B.; Bhatia, V.; Erdogan, T.; Sipe, J.E.; et al. Optimization of Sensitivity in Long Period Fiber Gratings with Overlay Deposition. *Optics Express, Vol. 13, Issue 1, pp. 56-69* **2005**, *13*, 56–69, doi:10.1364/OPEX.13.000056.

5. Del Villar, I.; Arregui, F.J.; Zamarreño, C.R.; Corres, J.M.; Bariain, C.; Goicoechea, J.; Elosua, C.; Hernaez, M.; Rivero, P.J.; Socorro, A.B.; et al. Optical Sensors Based on Lossy-Mode Resonances. *Sensors and Actuators B: Chemical* **2017**, *240*, 174–185, doi:10.1016/J.SNB.2016.08.126.

6. Cusano, A.; Iadicicco, A.; Pilla, P.; Contessa, L.; Campopiano, S.; Cutolo, A.; Giordano, M. Cladding Mode Reorganization in High-Refractive-Index-Coated Long-Period Gratings: Effects on the Refractive-Index Sensitivity. *Opt Lett* **2005**, *30*, 2536–2538, doi:10.1364/OL.30.002536.

7. Cusano, A.; Trono, C.; Baldini, F.; Chiavaioli, F.; Giordano, M.; Pilla, P. Giant Sensitivity of Long Period Gratings in Transition Mode near the Dispersion Turning Point: An Integrated Design Approach. *Optics Letters, Vol. 37, Issue 19, pp. 4152-4154* **2012**, *37*, 4152–4154, doi:10.1364/OL.37.004152.

8. Śmietana, M.; Koba, M.; Mikulic, P.; Bock, W.J. Towards Refractive Index Sensitivity of Long-Period Gratings at Level of Tens of Mm per Refractive Index Unit: Fiber Cladding Etching and Nano-Coating Deposition. *Optics Express* **2016**, *24*, 11897, doi:10.1364/OE.24.011897.

9. Cusano, A.; Iadicicco, A.; Pilla, P.; Contessa, L.; Campopiano, S.; Cutolo, A.; Giordano, M.; Guerra, G. Coated Long-Period Fiber Gratings as High-Sensitivity Optochemical Sensors. *Journal of Lightwave Technology* **2006**, *24*, 1776–1786, doi:10.1109/JLT.2006.871128.

10. Esposito, F.; Sansone, L.; Srivastava, A.; Baldini, F.; Campopiano, S.; Chiavaioli, F.; Giordano, M.; Giannetti, A.; Iadicicco, A. Long Period Grating in Double Cladding Fiber Coated with Graphene Oxide as High-Performance Optical Platform for Biosensing. *Biosensors and Bioelectronics* **2021**, *172*, 112747, doi:10.1016/J.BIOS.2020.112747.

11. Del Villar, I.; Matias, I.R.; Arregui, F.J. Deposition of Coatings on Long-Period Fiber Gratings: Tunnel Effect Analogy. *Optical and Quantum Electronics 2006 38:8* **2006**, *38*, 655–665, doi:10.1007/S11082-006-9002-3.

12. Esposito, F.; Srivastava, A.; Sansone, L.; Giordano, M.; Campopiano, S.; Iadicicco, A. Sensitivity Enhancement in Long Period Gratings by Mode Transition in Uncoated Double Cladding Fibers. *IEEE Sensors Journal* **2020**, *20*, 234–241, doi:10.1109/JSEN.2019.2942639.

13. Socorro, A.B.; Del Villar, I.; Corres, J.M.; Arregui, F.J.; Matias, I.R. Mode Transition in Complex Refractive Index Coated Single-Mode-Multimode- Single-Mode Structure. *Optics Express* **2013**, *21*, doi:10.1364/OE.21.012668.

14. Laffont, G.; Ferdinand, P. Tilted Short-Period Fibre-Bragg-Grating-Induced Coupling to Cladding Modes for Accurate Refractometry. *Measurement Science and Technology* **2001**, *12*, 765–770, doi:10.1088/0957-0233/12/7/302.

15. Caucheteur, C.; Paladino, D.; Pilla, P.; Cutolo, A.; Campopiano, S.; Giordano, M.; Cusano, A.; Mégret, P. External Refractive Index Sensitivity of Weakly Tilted Fiber Bragg Gratings with Different Coating Thicknesses. *IEEE Sensors Journal* **2008**, *8*, 1330–1336, doi:10.1109/JSEN.2008.926966.

16. Albert, J.; Shao, L.Y.; Caucheteur, C. Tilted Fiber Bragg Grating Sensors. *Laser and Photonics Reviews* 2013, *7*, 83–108.

17. Guo, T.; Liu, F.; Guan, B.O.; Albert, J. Tilted Fiber Grating Mechanical and Biochemical Sensors. *Optics & Laser Technology* **2016**, *78*, 19–33, doi:10.1016/J.OPTLASTEC.2015.10.007.

18. Li, Z.; Yang, X.; Zhu, H.; Chiavaioli, F. Sensing Performance of Fiber-Optic Combs Tuned by Nanometric Films: New Insights and Limits. *IEEE Sensors Journal* **2021**, *21*, 13305–13315, doi:10.1109/JSEN.2021.3068445.

19. Del Villar, I.; Fuentes, O.; Chiavaioli, F.; Corres, J.M.; Matias, I.R. Optimized Strain Long-Period Fiber Grating (LPFG) Sensors Operating at the Dispersion Turning Point. *Journal of Lightwave Technology* **2018**, *36*, 2240–2247, doi:10.1109/JLT.2018.2790434.

20. Malitson, I.H. Interspecimen Comparison of the Refractive Index of Fused Silica*,†. *J Opt Soc Am* **1965**, *55*, 1205, doi:10.1364/josa.55.001205.

21. Urrutia, A.; Del Villar, I.; Zubiate, P.; Zamarreño, C.R. A Comprehensive Review of Optical Fiber Refractometers: Toward a Standard Comparative Criterion. *Laser & Photonics Reviews* **2019**, *13*, 1900094, doi:10.1002/lpor.201900094.

22. Imas, J.J.; Albert, J.; Del Villar, I.; Ozcáriz, A.; Zamarreño, C.R.; Matías, I.R. Mode Transition During Deposition of Nanoscale ITO Coatings on Tilted Fiber Bragg Gratings. Advanced Photonics Congress, Maastricht, Netherlands (24 - 28 July 2022)

23. Imas, J.J.; Albert, J.; Del Villar, I.; Ozcáriz, A.; Zamarreño, C.R.; Matías, I.R. Mode Transitions and Thickness Measurements during Deposition of Nanoscale TiO_2 Coatings on Tilted Fiber Bragg Gratings. Journal of Lightwave Technology. In press. doi:10.1109/JLT.2022.3186596

24. Dominguez, I.; Del Villar, I.; Fuentes, O.; Corres, J.M.; Matias, I.R. Interdigital Concept in Photonic Sensors Based on an Array of Lossy Mode Resonances. *Scientific Reports 2021 11:1* **2021**, *11*, 1–11, doi:10.1038/s41598-021-92765-0.

25. Sarkar, S.; Gupta, V.; Kumar, M.; Schubert, J.; Probst, P.T.; Joseph, J.; König, T.A.F. Hybridized Guided-Mode Resonances via Colloidal Plasmonic Self-Assembled Grating. *ACS Applied Materials and Interfaces* **2019**, *11*, 13752–13760, doi:10.1021/ACSAMI.8B20535.

26. Del Villar, I.; Matias, I.R.; Arregui, F.J.; Achaerandio, M. Nanodeposition of Materials with Complex Refractive Index in Long-Period Fiber Gratings. *Journal of Lightwave Technology* **2005**, *23*, 4192–4199, doi:10.1109/JLT.2005.858246.

27. Jian, S.-S.; Huang, W.-P.; Lu, Y.-C. Full Vector Complex Coupled Mode Theory for Tilted Fiber Gratings. *Optics Express, Vol. 18, Issue 2, pp. 713-726* **2010**, *18*, 713–726, doi:10.1364/OE.18.000713.

28. Erdogan, T. Cladding-Mode Resonances in Short- and Long-Period Fiber Grating Filters. *Journal of the Optical Society of America A* **1997**, *14*, 1760, doi:10.1364/josaa.14.001760.

29. Albert, J.; Alam, M.Z. Selective Excitation of Radially and Azimuthally Polarized Optical Fiber Cladding Modes. *Journal of Lightwave Technology, Vol. 31, Issue 19, pp. 3167-3175* **2013**, *31*, 3167–3175.

30. Albert, J.; Shao, L.Y.; Caucheteur, C. Tilted Fiber Bragg Grating Sensors. *Laser and Photonics Reviews* 2013, *7*, 83–108.

31. Zhou, W.; Zhou, Y.; Albert, J. A True Fiber Optic Refractometer. *Laser & Photonics Reviews* **2017**, *11*, 1600157, doi:10.1002/LPOR.201600157.

32. George, S.M. Atomic Layer Deposition: An Overview. *Chemical Reviews* **2010**, *110*, 111–131, doi:10.1021/cr900056b.

33. Garcia-Caurel, E.; De Martino, A.; Gaston, J.P.; Yan, L. Application of Spectroscopic Ellipsometry and Mueller Ellipsometry to Optical Characterization. *Applied Spectroscopy* **2013**, *67*, 1–21, doi:10.1366/12-06883.

34. Del Villar, I. Ultrahigh-Sensitivity Sensors Based on Thin-Film Coated Long Period Gratings with Reduced Diameter, in Transition Mode and near the Dispersion Turning Point. *Optics Express* **2015**, *23*, doi:10.1364/OE.23.008389.

35. Cheung, C.S.; Topliss, S.M.; James, S.W.; Tatam, R.P. Response of Fibre Optic Long Period Gratings Operating near the Phase Matching Turning Point to the Deposition of Nanostructured Coatings. **2008**, *25*, 897–902, doi:10.1364/JOSAB.25.000897.

36. Shevchenko, Y.Y.; Albert, J. Plasmon Resonances in Gold-Coated Tilted Fiber Bragg Gratings. *Opt Lett* **2007**, *32*, 211–213, doi:10.1364/OL.32.000211.

Chapter 5

Conclusions and Future Lines

5.1 Conclusions

This thesis has contributed to the analysis and optimization, both theoretical and experimental, of different configurations and structures in optical fiber, applied to the development of sensors. Several structures have been studied in this thesis, including Lossy Mode Resonances (LMRs) and optical fiber gratings: FBGs (fiber Bragg gratings), LPGs (long period fiber gratings) and TFBGs (tilted fiber Bragg gratings). The main research lines that have been presented in this thesis are the fabrication of multisensing devices based on LMRs and the enhancement of the mode transition in optical fiber gratings for LPGs in double clad fibers and TFBGs. The common element between both research lines is the employment of thin films of high refractive index materials: tin oxide (SnO_2), indium tin oxide (ITO) and titanium dioxide (TiO_2).

First of all, the optical fiber structures that have been employed in this thesis have been introduced in Chapter 2. Here, these structures have been described in detail, discussing their principle of operation and their main characteristics, as well as enumerating their types, fabrication techniques and principal applications. Some aspects can be stressed out for each of these structures. Concerning LMRs, they stand out due to their high sensitivity. LMRs can be generated with both TE (transverse electrical) and TM (transverse magnetic) polarizations and several resonances can be obtained in the same spectrum. Regarding optical fiber gratings, FBGs possess a great potential to be combined with other structures for temperature compensation and improvement of their operation. In the case of LPGs, they have achieved a widespread employment due to the enhancement of their sensitivity obtained by means of the mode transition phenomena and the dispersion turning point (DTP). With respect to TFBGs, they have low sensitivities compensated by their narrow linewidth, obtaining values for the figure of merit (FOM) in the same order as LPGs, but with the added advantage of counting with multiple resonances, which enables the easy removal of cross-sensitivities and the development of multiparameter sensors.

In Chapter 3, different structures and configurations based on LMRs have been assessed with the purpose of developing multisensing platforms. In the first place, it was explored the design of a structure that would produce an LMR in the transmission spectrum and bands in the reflection spectrum. With this purpose, a thin film with a grating pattern was simulated on two different substrates, a coverslip (planar waveguide) and a D-shaped optical fiber. It was checked that the Bragg-Snell equation for normal incidence could be used for correctly estimating the position of the reflected bands in the spectrum.

Two designs were used for the thin film. The initial design was a thin film with a grating pattern along all its length. It was expected that the thin film, in spite of the

grating, would be able to generate an LMR while the grating would produce the reflection bands. However, when simulating this design on a coverslip, it was concluded that it could not be found a value for the grating pitch where both phenomena would be present. A small grating pitch (in the order of the µm) would produce the bands in the reflection spectrum but in this case the thin film would not be able to generate the LMR. On the other hand, if the grating pitch was increased until several hundreds of µm (500 - 800 µm), the LMR would begin to be clearly visible, but the reflection bands would be too close to be able to distinguish them. In order to solve this problem, and generate simultaneously the LMR and the reflection bands, a second thin film pattern was proposed. Instead of employing a grating pattern along all the thin film length, the grating would only be used in part of it, leaving the other part of the thin film with constant thickness. This new design was able to produce both types of phenomena. A coverslip with a grating pitch with value of 3 µm - 5 µm was used as substrate. However, for the simulated parameters values, the power of the reflection bands seems too low for a practical implementation. It is believed that the most promising alternative for this problem would be increasing the length of the grating, which is expected to produce more powerful reflection bands (this result has been observed in the case of the D-shaped optical fiber).

Then, a thorough theoretical study was carried out for the grating pattern design on a D-shaped fiber, in which only the reflection bands are obtained. This study began because initially the power of the reflection bands was too low and it was easier to study the variation of the different parameters for improvements for the pure grating pattern than for the more complex design (grating and section of constant thickness). This analysis became complete enough to justify its publication on its own in "*Optimization of Fiber Bragg Gratings Inscribed in Thin Films Deposited on D-Shaped Optical Fibers*" in Sensors 2021, Vol. 21, 4056 (2021).

The main part of the analysis was focused on the reflection band located at 1650 nm, for a grating pitch of 4 µm, a D-shaped section (equal to the grating length) of 20 mm, a SRI value of 1.33 (water) and using SnO_2 as the thin film material. The reflected power and the FWHM were studied for variations in the thin film thickness, the neck and the length. The highest power was achieved for low necks (-2 µm - 0 µm), thick thin films (50 nm - 125 nm) and lengths as long as possible (limited in practice to around 20 mm), although a trade-off between the reflected power and the FWHM is required. The sensitivity to the SRI, the FWHM and the FOM were also studied for variations in the SRI in the 1.33 - 1.4 range. Again, the best results were obtained for low necks and thick thin films and it is necessary to achieve a compromise between the sensitivity to the SRI and the FOM. The main obstacle to the practical implementation of this structure is the need for low necks, which would require further etching or polishing of the D-shaped fiber, making it more fragile. On the other hand, the second thin film pattern (grating section and section of constant thickness) was also studied on a D-shaped fiber, obtaining in this case both an LMR and the bands in the reflection spectrum.

The second configuration that was studied in chapter 3 was the combination of an LMR and an FBG on a D-shaped optical fiber. The LMR was obtained through the deposition of a 60 nm TiO_2 thin film with an atomic layer deposition (ALD) system

while the FBG, whose peak was located at 1553 nm, was inscribed on the core of the fiber with the phase mask method. Two essays were carried out, in the first one the SRI was varied while the temperature was kept constant, while in the second the temperature was modified from 25ºC to 45ºC in 5ºC steps in ultrapure water. These essays enabled to obtain the sensitivities of both the LMR and the FBG to the SRI and the temperature, respectively. In particular, the LMR had a sensitivity of 3725.2 nm/RIU in the SRI range from 1.3324 to 1.3479 while the FBG had a linear temperature sensitivity of 32.6 pm/ºC in the 25ºC - 45ºC range. It has also to be considered that the FBG sensitivity to the SRI is negligible. This way, the sensor is fully characterized and it can measure both the SRI (the temperature drift of the LMR is eliminated) and the temperature. These results were published in the article "*Optical Fiber Thermo-Refractometer*" in Optics Express, Vol. 30, Issue 7, pp. 11036-11045 2022. The proposed device would be interesting for biosensing applications, in which it is important to count with sensors with a high sensitivity as well as temperature compensation capabilities.

The final device that was introduced in chapter 3 was a dual LMR, that is, two independent LMRs, on a single D-shaped optical fiber. LMRs were generated by a thin film with two sections of different thickness. The first section had a thickness of 120 nm (TiO_2) and was responsible for producing the LMR located at shorter wavelengths (known as blue LMR) while the second section had a thickness of 140 nm (120 nm of TiO_2 and 20 nm of SnO_2) and generated the LMR located at longer wavelengths (named red LMR). The TiO_2 layer was deposited with an ALD system while an electron beam was employed for the SnO_2 layer. It was experimentally demonstrated that each resonance only shifts when the SRI in which the corresponding section of the D-shaped fiber is immersed in varies. It was also theoretically studied and experimentally shown, through the fabrication of several devices, that the depth of each resonance can be tuned with the length of the corresponding section. The length of the section corresponding to the blue LMR has to be longer than that corresponding to the red LMR in order to have two resonances with a similar depth, which is a desired condition for making their monitoring easier. In particular, for the values and materials used in this work the optimum length would be 7.5 mm and 2.5 mm for the first and the second sections, respectively. Finally, the sensitivities of the resonances of the manufactured devices were also assessed, achieving values ~4000 nm/RIU (not very relevant differences were found between the sensitivities of the blue and the red LMRs) with a maximum of 4506 nm/RIU for values of the SRI between 1.3327 and 1.3485.

In Chapter 4, the mode transition phenomenon has been studied, both numerically and experimentally, in two types of optical fiber structures: double-clad LPGs in which the refractive index of the second cladding is lower than that of the first cladding, and TFBGs.

In the first place, an enhancement of the mode transition in LPGs was proposed through the use of double-clad fibers. Fibers with different second cladding thicknesses were initially obtained by controlling the wavelength shift during the etching process. It was experimentally demonstrated through the deposition of a TiO_2 coating on the previously manufactured fibers that, with a thicker second-cladding,

the sensitivity to the thin film thickness during the mode transition increases, being the wavelength shift more abrupt. These results were supported by simulations of both the effective indices of the cladding modes of the LPGs (linked to the resonances through the phase matching condition) and the wavelength shifts of the resonances, which precisely reproduced the experimental results. Therefore, the sensitivity during the mode transition can be tuned with the thickness of the second cladding. Nevertheless, it was also shown that the increase in sensitivity that is obtained with the utilization of a second cladding is not unlimited. For a certain thickness of the second cladding, the resonance fades in the mode transition region. Therefore, a trade-off between the sensitivity and the ability to track the resonance band must be established. Finally, the SRI sensitivity in liquids (1.33 - 1.47 SRI range) was studied for two fibers with different thicknesses of the second cladding, and a higher sensitivity was achieved for the fiber with the thicker second cladding (approximately double in the 1.435 - 1.45 RI range, obtaining a sensitivity of 5000 nm/RIU in the 1.43 - 1.44 range). These results have been submitted for publication and are under review at the moment these conclusions are being written.

In the second part of the chapter, the mode transition was experimentally demonstrated in TFBGs through the deposition of a thin film of materials with a higher refractive index than that of the silica cladding, similarly to LPGs. The mode transition was first shown for an ITO deposition with a sputtering deposition system employing an S-polarized TFBG. The mode transition was not clearly visible in the initial data, but after taken into account that the temperature was not constant during the deposition, the data were corrected by subtracting the wavelength shift of the Bragg wavelength, making the mode transition clearly visible. These initial results were published in the conference paper "*Mode Transition During Deposition of Nanoscale ITO Coatings on Tilted Fiber Bragg Gratings*" in the Advanced Photonics Congress, Maastricht, Netherlands (24 - 28 July 2022)

Then, two TiO_2 thin-film depositions were carried out with an ALD system, each one with a separate TFBG and a different polarization state (P-polarization, corresponding to EH modes; and S-polarization, corresponding to HE modes; respectively). It was also demonstrated that the mode transition has different properties for the two polarization states, being sharper and taking place at much smaller thicknesses for the HE modes than for the EH modes. These results were supported with simulations of the evolution of the effective indices of the cladding modes and the power distribution of the mode fields as a function of the coating thickness. As it was expected from perturbation analysis, the maximum rate of change of the mode effective index closely matched the maximum in the mode power fraction in the coating. It is also relevant to mention that the shift of the resonances could be tracked without a significant depth reduction (a partial fading was observed in the ITO case, but none in the case of TiO_2).

Finally, the experimental TiO_2 mode transitions were compared with simulated ones (assuming $n = 2.14$, value given by the ellipsometer) in order to obtain a value for the final thin film thickness for each of the two depositions. The results obtained differed in 5%, which is an acceptable result, and they were closer to the values given by the SEM (-9% for the P-polarized deposition, -1% for the S-polarized one) than to those

provided by the ellipsometer (-16% and -18%, respectively), although it has to be considered that the deposited coatings were not very homogeneous, which could be the reason behind the discrepancy with the ellipsometer results. These results corresponding to the TiO_2 depositions have been published in the article "*Mode Transitions and Thickness Measurements during Deposition of Nanoscale TiO_2 Coatings on Tilted Fiber Bragg Gratings*" in the Journal of Lightwave Technology (in press).

5.2. Future lines

The results presented in this thesis suggest the continuation of the research in various fields. In the first place, regarding the analysis for obtaining an LMR and bands in the reflection spectrum with a grating pattern on the thin film, the second studied design (grating section and section of constant thickness) on a coverslip seems the most promising structure for a practical implementation if it is finally possible to obtain more powerful reflection bands with a proper selection of the parameters of the device. In this case, this structure should be tested as a multisensing platform, for instance, trying to measure the SRI and temperature simultaneously, as it was done with our combination of LMR and FBG in a D-shaped optical fiber.

Concerning the utilization of an LMR and an FBG on a single D-shaped optical fiber, the FBG inscribed on the core of the optical fiber could also be used, for example, in combination with the dual LMR structure that has been developed. This way, a multiparameter sensor based on the LMRs could be manufactured, counting as well with the temperature compensation offered by the FBG. One of the most promising applications for the dual LMR structure would be its employment in the biosensing field, as the possibility of detecting several biomarkers linked to the same disease with a single device would be really useful. The previous optical biosensors based on LMRs using D-shaped optical fibers are a good starting point, although the greatest challenge will be the separate biofunctionalization of each of the sections of the thin film associated to the generation of each LMR.

With respect to the mode transition, the results obtained for the mode transition in LPGs with double clad fibers open the path to further enhance the SRI sensitivity of these devices. Although it was demonstrated that LPGs with a low refractive index second cladding possess better SRI sensitivity in liquids than standard LPGs, the employed LPGs had not been optimized for this purpose, so there is still room for improvement. In addition to this, this phenomenon can also be combined with DTP, even increasing more the sensitivity. If high sensitivities are finally achieved, these devices would be an interesting platform for developing biosensors, as it is the case of standard LPGs working at the mode transition or the DTP. On the other hand, the concept of optical fibers with a thin second cladding could also be extrapolated to other structures, such as TFBGs, contributing to the enhancement of their mode transition as well.

Finally, regarding the mode transition in TFBGs, after demonstrating the possibility of recovering the thickness of the deposited thin film if the refractive index is known, the next step would be obtaining both the refractive index and the thickness of the

thin film without any additional information, in a similar fashion to the operation of an ellipsometer. This method would be based in simulating the mode transition for a range of refractive index values and comparing them with the experimental mode transition. For each refractive index value, the thin film thickness that best fits the experimental results would be calculated. Then, the pair (refractive index, thickness) that gives the lowest difference between the experimental mode transition and the simulated one would be determined, providing the final solution. This way, an alternative method to the ellipsometer for obtaining both the thickness and the refractive index of a thin film, based on the mode transition on TFBGs, could be employed. A similar approach, but using an LPG mode transition instead, could also be tried.

Appendix I

Scientific Contributions

I.1. Publications on scientific journals directly related to this thesis

2.4.3.1. Imas, J.J.; Zamarreño, C.R.; Del Villar, I.; Matías, I.R. Optimization of Fiber Bragg Gratings Inscribed in Thin Films Deposited on D-Shaped Optical Fibers. *Sensors 2021, Vol. 21, Page 4056* **2021**, *21*, 4056, doi:10.3390/S21124056.

2.4.3.2. Imas, J.J.; Zamarreño, C.R.; Del Villar, I.; Da Silva, J.C.C.; Oliveira, V.; Matías, I.R. Optical Fiber Thermo-Refractometer. *Optics Express, Vol. 30, Issue 7, pp. 11036-11045* **2022**, *30*, 11036–11045, doi:10.1364/OE.450316.

2.4.3.3. Imas, J.J.; Zamarreño, C.R.; Zubiate, P.; Del Villar, I.; Pérez-Escudero, J.M.; Matías, I.R. Twin Lossy Mode Resonance on a Single D-Shaped Optical Fiber. *Optics Letters, Vol. 46, Issue 13, pp. 3284-3287* **2021**, *46*, 3284–3287, doi:10.1364/OL.425928.

2.4.3.4. Imas, J.J.; Albert, J.; Del Villar, I.; Ozcáriz, A.; Zamarreño, C.R.; Matías, I.R. Mode Transitions and Thickness Measurements during Deposition of Nanoscale TiO_2 Coatings on Tilted Fiber Bragg Gratings. *Journal of Lightwave Technology*. In press. doi:10.1109/JLT.2022.3186596

2.4.3.5. Del Villar, I.; Montoya-Cardona, J.; Imas, J.J.; Reyes-Vera, E.; Zamarreño, C.R.; Matías, I.R.; Cruz, J.L. Mode tunneling in double-clad fibres: a novel paradigm in optical fibre sensing. Submitted, in reviewing process.

I.2. Other publications on scientific journals

1. Imas, J.J.; Zamarreño, C.R.; Zubiate, P.; Sanchez-Martín, L.; Campión, J.; Matías, I.R. Optical Biosensors for the Detection of Rheumatoid Arthritis (RA) Biomarkers: A Comprehensive Review. *Sensors 2020, Vol. 20, Page 6289* **2020**, *20*, 6289, doi:10.3390/S20216289.

2.4.3.6. Vitoria, I.; Zamarreño, C.R.; Ozcáriz, A.; Imas, J.J.; Matías, I.R. Beyond Near-Infrared Lossy Mode Resonances with Fluoride Glass Optical Fiber. *Optics Letters* **2021**, *46*, 2892, doi:10.1364/OL.428533.

2.4.3.7. Vitoria, I.; Zamarreño, C.R.; Ozcáriz, A.; Imas, J.J.; Del Villar, I.; Matías, I.R. Surface Exciton Plasmon Resonances (SEPR) Based Sensors. Submitted, in reviewing process.

I.3. Participation in International Conferences

1. Imas, J.J.; Albert, J.; Del Villar, I.; Ozcáriz, A.; Zamarreño, C.R.; Matías, I.R. Mode Transition During Deposition of Nanoscale ITO Coatings on Tilted Fiber Bragg Gratings. Advanced Photonics Congress, Maastricht, Netherlands (24 - 28 July 2022)

2.4.3.8. Imas, J.J.; Zamarreño, C.R.; Zubiate, P.; Campión, J.; Sánchez-Martín, L.; Matías, I.R. Rheumatoid Arthritis MiRNA Biomarker Detection by Means of LMR Based Fiber-Optic Biosensor. IEEE Sensors 2020; Rotterdam, Netherlands (25 - 28 October 2020).

I.4. Participation in National Conferences

1. Imas, J.J.; Gracia, A.; Vitoria, I.; Zamarreño, C.R. Low cost mid-infrared detection system. XIII Spanish National Meeting on Optics (22 - 24 November 2021)

2.4.3.9. Vitoria, I.; Gracia, A.; Garnica, I.; Imas, J.J.; Zamarreño, C.R. Low-cost multispectral imaging system based on multi-led light source. XIII Spanish National Meeting on Optics (22 - 24 November 2021)